Australian Government
Geoscience Australia

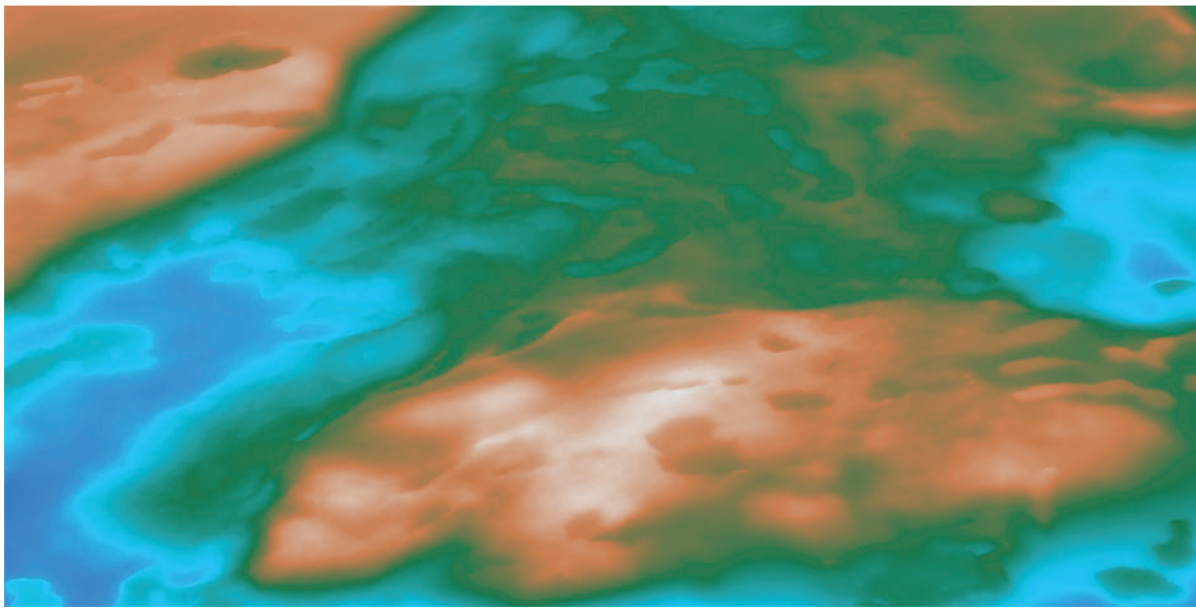

Record 2012/60 | **GeoCat** 74291

The Cooper Basin 3D Map Version 2:

Thermal Modelling and Temperature Uncertainty

A.J. Meixner, A.L. Kirkby, D.T. Lescinsky and N. Horspool

The Cooper Basin 3D Map Version 2: Thermal Modelling and Temperature Uncertainty

GEOSCIENCE AUSTRALIA
RECORD 2012/60

by

A.J. Meixner, A.L. Kirkby, D.T. Lescinsky and N. Horspool

Australian Government
Geoscience Australia

Department of Resources, Energy and Tourism
Minister for Resources and Energy: The Hon. Martin Ferguson, AM MP
Secretary: Mr Drew Clarke

Geoscience Australia
Chief Executive Officer: Dr Chris Pigram

This paper is published with the permission of the CEO, Geoscience Australia

ISSN 1448-2177
ISBN 978-1-922103-83-3 (PDF)

GeoCat # 74291

Bibliographic reference: Meixner, A.J., Kirkby, A.L., Lescinsky, D.T., and Horspool, N., 2012. *The Cooper Basin 3D map version 2: Thermal modelling and temperature uncertainty*. Record 2012/60. Geoscience Australia: Canberra

Contents

Executive summary

A three-dimensional (3D) geological map of the Cooper Basin region has been produced from 3D inversions of Bouguer gravity data using geological data to constrain the inversions. The 3D map has been used to predict temperatures and their uncertainty throughout the volume of the map. This will allow regions of elevated predicted temperature at 4 – 5 km to be identified, which may provide targets for future geothermal exploration in the Cooper Basin region. The 3D map delineates regions of low density within the basement of the Cooper and Eromanga basins. These are inferred to be granitic bodies, which may act as heat sources. It also delineates the stratigraphy of the sedimentary basins which provide thermal insulation. The 3D map, which contains the geology as well as predicted temperature values and uncertainty throughout the study volume, has been included as a digital appendix (Appendix A) which accompanies this report. This release is the second version of the 3D map of the Cooper Basin region. It builds on Version 1 of the Cooper Basin Region Geological map, released in 2009.

The Cooper Basin region is coincident with a prominent geothermal anomaly and forms part of a broad area of anomalously high heat flow. High-heat-producing granites, including granodiorite of the Big Lake Suite (BLS) at the base of the Cooper and Eromanga basin sequences, combined with thick Cooper and Eromanga sedimentary sequences of low thermal conductivity, result in temperatures as high as 270 °C at depths of 4.5 – 5 km. The location and characteristics of other granitic bodies are poorly understood and accurately identifying them is an important first step towards future geothermal exploration in this region.

3D Bouguer gravity field inversion modelling was carried out using the University of British Columbia – Geophysical Inversion Facility (UBC-GIF) (Li and Oldenburg, 1998a) inversion software. An initial gravity inversion was performed using seismic horizons to constrain the 3D distribution of the Cooper and Eromanga basin sediments. Densities, derived from down hole logging of wells in the region, were assigned to the Cooper and Eromanga basin sediments to constrain their contribution to the gravity signal. A series of iso-surfaces were generated, enclosing lobes of low predicted density within the basement. Gravity 'worming' or multi-scale edge mapping was performed in order to approximate the lateral sub-sediment extent of modelled granites within the basement. A series of subsequent granite-constrained inversions was generated by assigning different maximum cut-off depths to the lobes. The inversion model that produced the most uniform density distribution within the non-granitic basement had a maximum cut-off depth of 10 km.

Forward predictions of temperatures were carried out using the Simulator for HEat and MAss Transport (SHEMAT) software package (Clauser, 2003). The initial thermal model produced temperature predictions that were too low compared with the available down-hole temperature measurements. A sensitivity analysis was performed to select the thermal properties which, when varied, had the greatest effect on the predicted temperatures. These properties are: thermal conductivity of the basin sediments, heat production of the basement and granite units, and basal heat flux. It was necessary to substantially increase the heat production of the basement and granite units, and the basal heat flux in order to match the temperature and heat flow data. Final values for basement heat production range from 3.8 – 5.3 $\mu W/m^3$; final values for granite range from 3.8 – 8.7 $\mu W/m^3$. It was also necessary to reduce the thermal conductivity of the basin sediments by applying a multiplier of 0.85 in order to match the temperature data. The final, optimised thermal model shows strongly elevated temperatures at 4 km depth in the vicinity of the BLS (up to 235 °C), as well as broader regions of elevated temperature (190 – 200 °C) in the northwest of the study area

toward Mt Isa, beneath the Warrabin Trough in the northeast of the study area, and southeast of the BLS. Cooler temperatures (~160 °C) were predicted at 4 km depth in the southwestern corner of the study area.

Stochastic modelling was carried out on the final thermal model in order to characterise the uncertainty of the predicted temperatures and heat flow values due to the uncertainty in the input thermal properties. A standard deviation of the temperature at each point in the model was calculated from the resulting stochastic models. The stochastic modelling technique was implemented using SHEMAT, combined with the Python scripting library PySHEMAT (Wellmann et al., 2012), and other scripting libraries developed internally. The results show that areas of highest predicted temperature are also areas of highest absolute error. However, the highest percentage errors occur where the Cooper Basin sediments are thickest. Lower percentage errors occur over the BLS and in the southeast of the model area.

Introduction

The Cooper Basin region straddles the Queensland/South Australia border (Figure 1) and is coincident with a prominent geothermal anomaly (Cull and Denham, 1979; Cull and Conley, 1983; Somerville et al., 1994) (Figure 2). The region forms part of a broad area of anomalously high heat flow, which is attributed to Proterozoic basement enriched in radiogenic elements (Sass and Lachenbruch, 1979; McLaren et al., 2003). High-heat-producing granites, including granodiorite of the Big Lake Suite (BLS) at the base of the Cooper and Eromanga sequences, are the target of Australia's first Hot Rock geothermal development at Habanero (near Innamincka in South Australia, Figure 1). This development aims to produce electricity from heat energy contained in regions of elevated temperature (250 °C) at depths of 4-5 km in the crust[1]. The association between high heat flow, high temperature gradient and elevated heat production in the BLS is well accepted (Middleton, 1979; Gallagher, 1988; Beardsmore, 2004). The thick sedimentary sequences of the overlying Cooper and Eromanga basins provide a thermal insulation effect which, combined with the high heat flow, result in temperatures as high as 270 °C at depths of 4 – 5 km (Holgate, 2005). There is a high probability that analogous geothermal targets exist in association with other granitic bodies lying beneath the Cooper and Eromanga basins. For the most part, the location and characteristics of these bodies are poorly understood. Accurately identifying them and modelling their thermal character is an important first step towards future geothermal exploration in this region.

The aim of this study is to characterise the temperature distribution and its uncertainty at depths of 4 – 5 km across the broader Cooper Basin region in order to identify similar targets to that associated with the BLS at Habanero.

[1] http://www.geodynamics.com.au/IRM/content/home.html

Geology of the Cooper Basin region

PRECAMBRIAN BASEMENT

The basement to the Cooper Basin region is completely covered by successive sedimentary sequences of the Warburton, Cooper and Eromanga basins, as well as sediments of the Warrabin Trough. Proterozoic basement well intersections have been recorded in a number of wells in the study area. In the south, Fortville 3 (Figure 3) intersected highly sheared and folded quartz-sericite schist which was considered by Gatehouse (1986) to be part of the Willyama Supergroup. Also in the south, Daralingie 1 intersected steeply dipping orthoquartzite of possible Proterozoic age (Gravestock et al., 1995). In the west, Haddon Downs 1 intersected protomylonitic pegmatitic gneiss that was considered to part of the Arunta Block by Rankin and Gatehouse (1990). This interpretation is at odds with the interpreted basement in this region from the Australian Crustal Elements Map of Shaw et al. (1996) which assigns the entire northwestern basement of the study area to the Palaeozoic Thomson Fold Belt. The Crustal Elements map, which delineates upper crustal elements based primarily on composite geophysical data (magnetic and gravity), shows all but a small region in the south of the study area to be underlain by the Thomson Fold Belt (Figure 3). In this southern region the basement has been assigned to the North Flinders arm of the Adelaide Geosyncline and the Wonominta Block and in the southeast, the Bourke Geophysical Region.

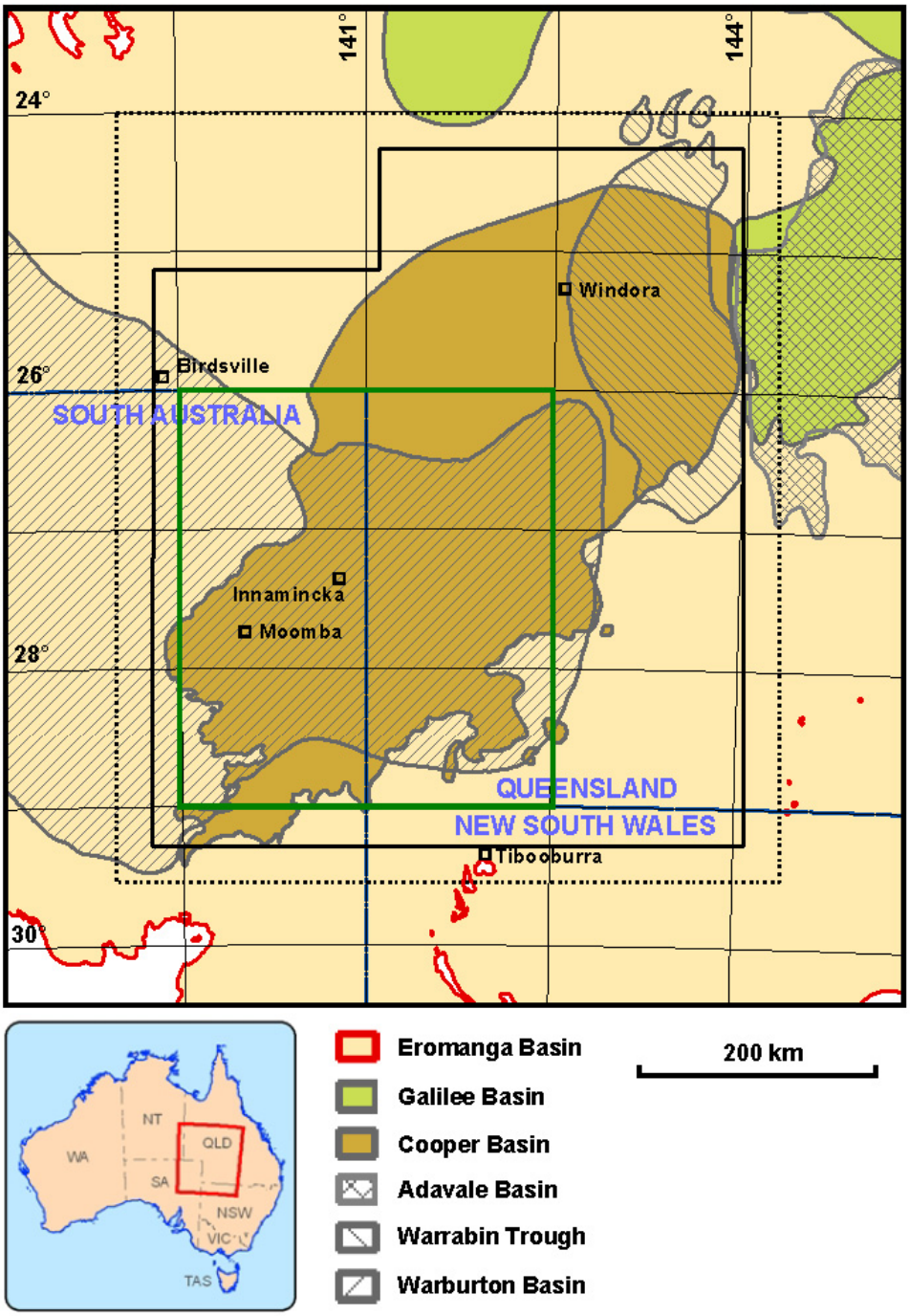

Figure 1: *Location of the Cooper Basin region, showing the spatial extents of the stacked Warburton, Cooper and Eromanga basins. The outer black solid line indicates the extents of the Version 2 Cooper Basin 3D Map, while the dashed black line shows the buffered map extents (see text). The solid green box shows the extents of the Version 1 Cooper Basin 3D map (Meixner and Holgate, 2009).*

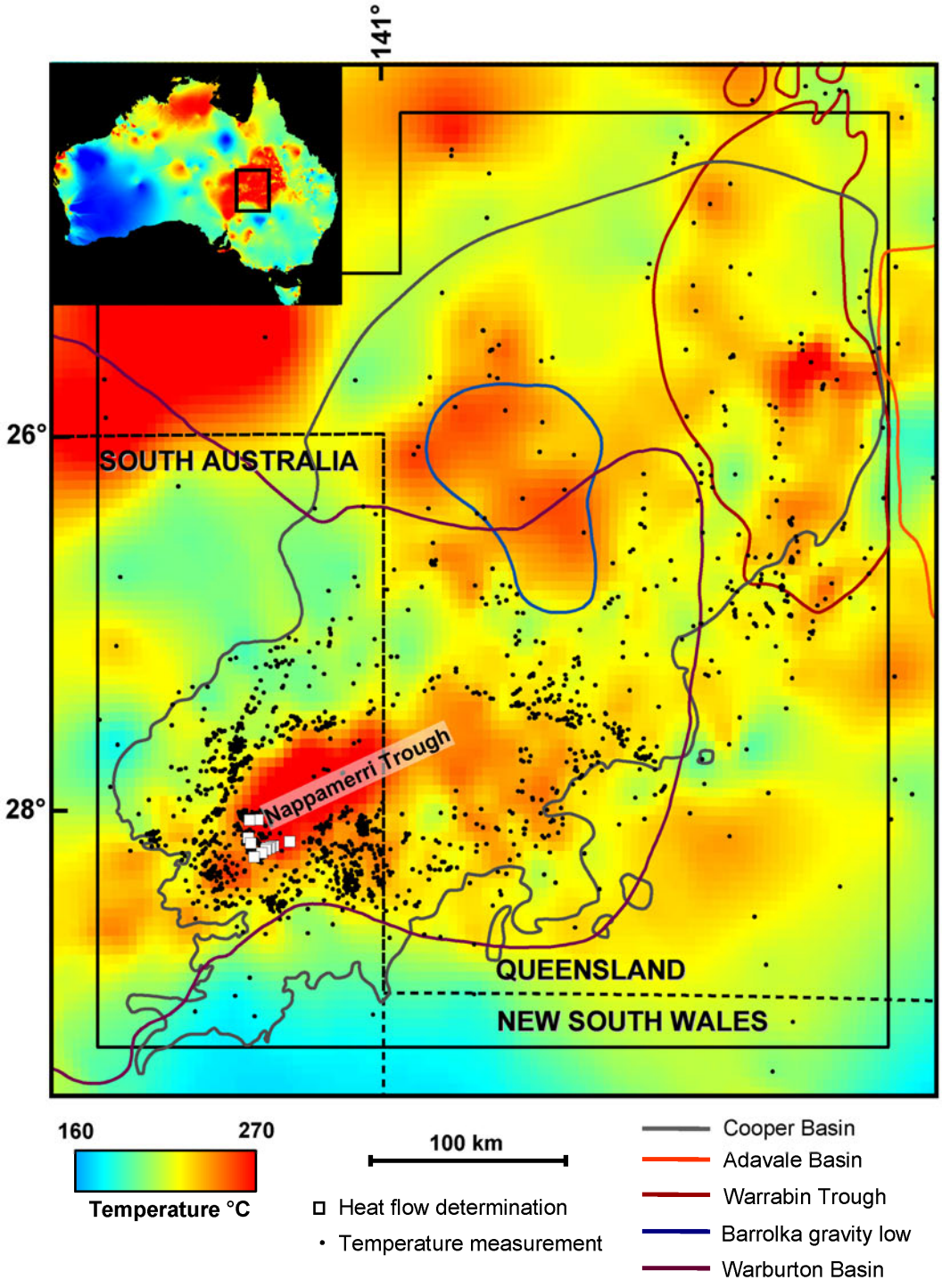

Figure 2: *Map of predicted temperatures at 5 km depth in the Cooper Basin region (main figure), and across Australia (inset) (Gerner and Holgate, 2010). Scale bar applies to the main image. Well locations from which the temperature measurements were taken are shown (black dots), as is the outline of the Cooper Basin (dark gray line). Also shown are the heat flow measurements in the region (white squares; Beardsmore, 2004). The black outline shows the extent of the study area.*

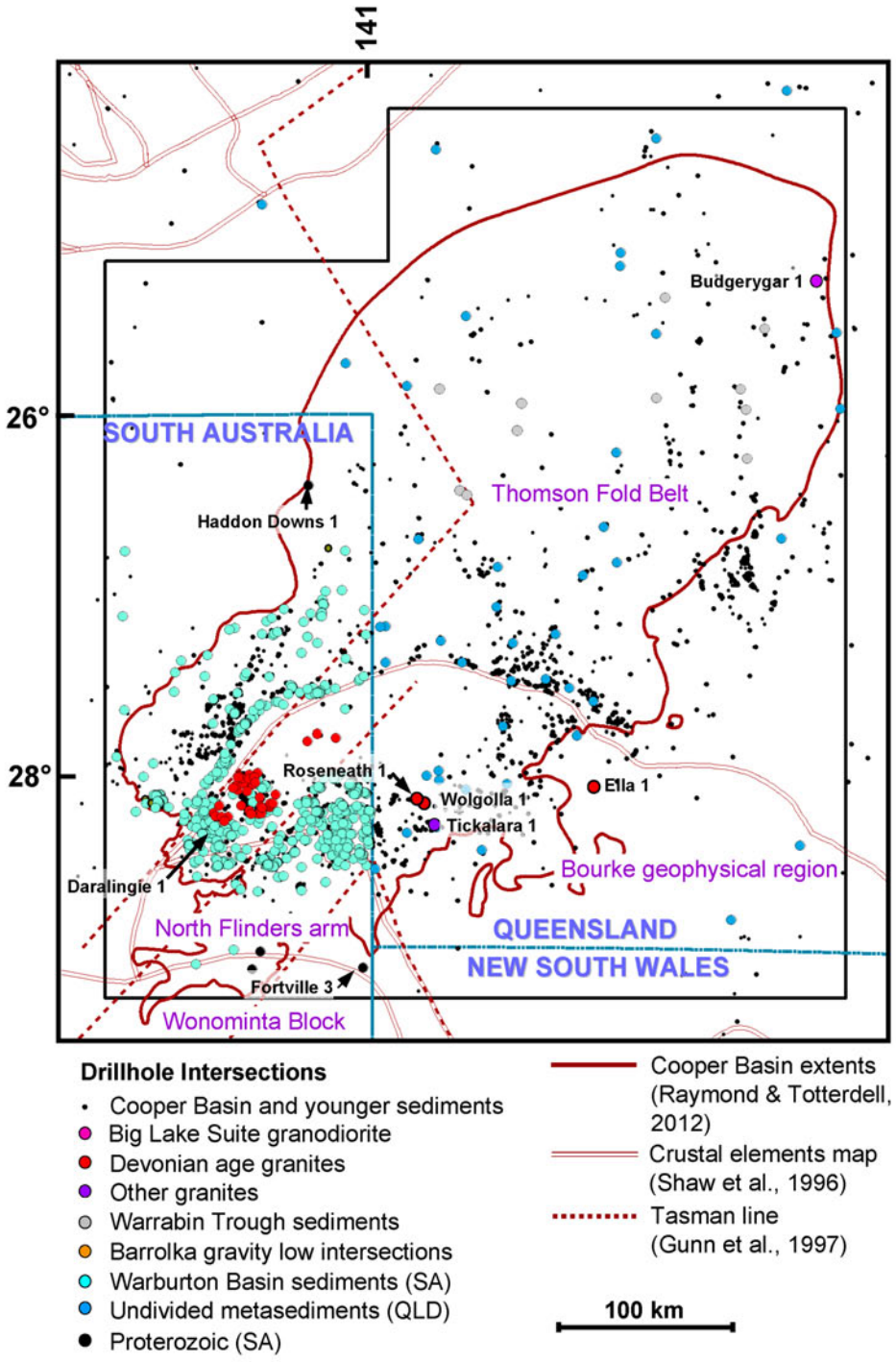

Figure 3: *Locations of well intersections and two different interpretations of basement geology. The black outline shows the extents of the study area.*

More recent interpretations of the Tasman Line (summarised by Direen and Crawford, 2003), which defines the eastern extent of the Proterozoic continental boundary (Gunn et al., 1997) are consistent with the available drill-hole data. The Tasman Line has been located by a number of authors (e.g., Scheibner and Veevers, 2000; Gunn et al., 1997) by near-coincident gravity and magnetic lineaments from the Australian national gravity and magnetic datasets (Bacchin et al., 2008; Milligan et al., 2010). The boundary truncates the Proterozoic Mt Isa Inlier to the north of the study area and is expressed on the southern edge of the study area by apparent continuous sigmoidal anomalies in the Koonenberry belt of western New South Wales (Direen and Crawford, 2003). Between the Mt Isa truncation and the Koonanberry anomalies, the location of the Tasman Line is less well defined as the anomalies are of broader wavelength due to the covering Cooper and Eromanga basin sediments. Figure 3 shows the location of the Tasman line as defined by Gunn et al. (1997). The multiple northeast trending lines are interpreted to be transfer/transform faults. The Gunn et al. (1997) interpretation shows the Proterozoic basement extending into the western portion of the study area.

WARBURTON BASIN

The Cambro-Ordovician Warburton Basin lies above the pre-Cambrian basement in the south and west of the study area and is buried by a minimum 1000 m of overlying sediments. The geology of the Warburton Basin is summarised by Radke (2009) and Meixner et al. (1999) and is based on studies including Gatehouse (1983a; 1983b; 1986), Gravestock and Gatehouse (1995), and Sun (1996; 1997; 1998).

The Warburton Basin consists of the following stratigraphic units: Mooracoochie Volcanics (felsic volcanics); Kalledeina Formation (primarily carbonates) which includes the Jena Basalt; Dullingari Group (dominantly shales), and, Innamincka Formation (red beds). Sedimentation ceased in the late Ordovician and was followed by orogenesis during which burial depths are estimated to have reached 7 – 8 km (Sun, 1996, 1997; Boucher, 1996). Burial metamorphism resulted in prehnite formation in the Mooracoochie Volcanics. In the study area, the basin has been subjected to compressional tectonism, producing tightly folded to overturned beds and thrust faulting (Meixner et al., 1999).

ADAVALE BASIN SYSTEM

The Adavale Basin System defined by Draper et al. (2004) collectively refers to the Adavale Basin, the Warrabin Trough and the Barrolka Trough. The Devonian Adavale Basin is situated outside and immediately to the east of the study area, while the Warrabin and Barrolka troughs are located in the northeast of the study area (Figure 4). These basins, including the Belyando and Burdekin basin situated to the northeast of the study area, were once remnants of more extensive basins (Draper et al., 2004). The Adavale Basin initially developed in the mid-late Early Devonian as an intracontinental volcanic rift or extensional basin (Finlayson et al., 1988, Hoffmann 1988, Evans et al., 1990, Murray 1990, 1994).

The Warrabin Trough stratigraphy is poorly known due to sparse data, however, the sediments appear to share a common history with the Adavale Basin (Draper et al., 2004). The stratigraphy consists of Early Devonian basal volcanics, followed by deltaic to marine siliclastics and shallow marine dolomites, ending with Late Devonian red bed siliclastics (Paten, 1977). Seismic traverses acquired in 1980 by the Bureau of Mineral Resources in cooperation with the Geological Survey of Queensland show a maximum thickness of 3 km (Passmore and Sexton, 1984).

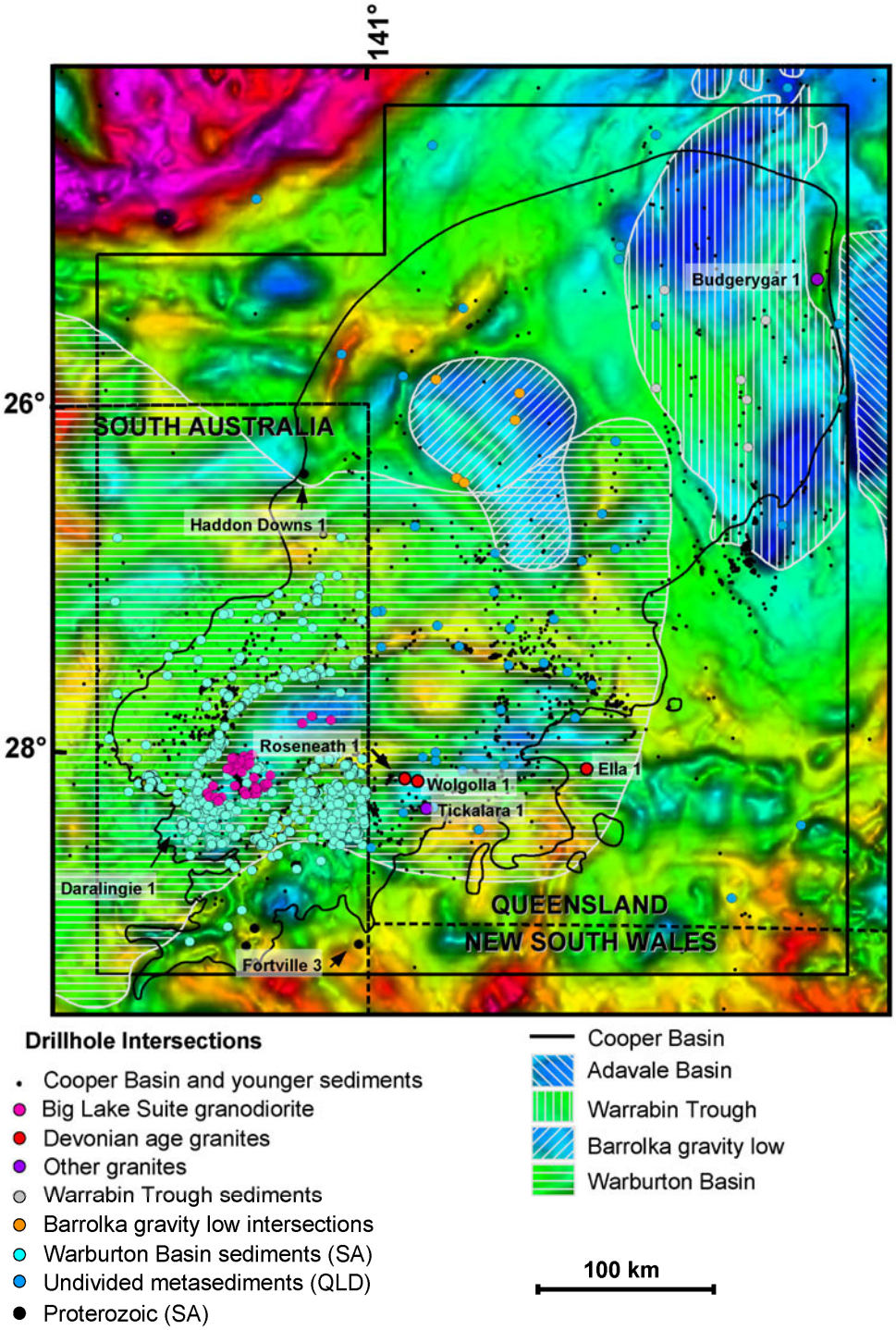

Figure 4: *Bouguer gravity image showing the locations of well intersections and basin extents. The image was created from data subsectioned from the Gravity Anomaly Map of Australia (Bacchin et al., 2008). The Cooper Basin outline is from Raymond and Totterdell (2012). The Warrabin Trough, Adavale Basin and Barrolka Gravity Low outlines are from the Geological Survey of Queensland (2004).*

Murray (1994) interpreted sediments intersected at depth in five wells located on a prominent gravity low (Figure 4) to be Devonian in age due to their similarity with cores from the Warrabin Trough. Murray (1994) concluded that a subsurface basin, which he named the Barrolka Trough after the coincident gravity low (Lake Barrolka Gravity Low – Lonsdale, 1965; Barrolka Gravity Depression – Fraser et al., 1977), was responsible for the gravity low. McKillop et al. (2005) did not consider the Barrolka Trough to be part of the Adavale Basin System and suggested that the well intersections originally attributed to Devonian age sediments were likely to be Ordovician rocks of the Warburton Basin. This interpretation is at odds with Stewart (pers. comm.,) who, based on the low metamorphic grade (lower greenschist facies or less) of the core descriptions of Murray (1994), suggests that the intersected sediments are Barrolka Trough Devonian sediments, as Murray (1994) stated, and are not Cambro-Ordovician metasediments of the Warburton Basin, which are typically metamorphosed from lower to upper greenschist facies.

COOPER BASIN

The Late Carboniferous to Triassic Cooper Basin sequence is host to significant petroleum resources (Radke, 2009) and reaches thicknesses of up to 2.5 km. The basin unconformably overlies the Warburton Basin, Warrabin Trough, BLS, Devonian age granite and granites of unknown age and Palaeozoic and older basement units. This unconformity makes up part of the seismic Z-horizon, which has been mapped across the Cooper Basin region by the National Geoscience Mapping Accord (NGMA) and is colloquially referred to as the 'top basement' (Figure 5; NGMA, 2001). The basin is entirely obscured by the overlying Eromanga Basin.

In this study, we have adopted the Cooper Basin stratigraphy (Figure 6) from Gatehouse (1972) and Kapel (1972). The Merrimelia Formation and Tirrawarra Sandstone comprise a glacio-lacustrine and glacio-fluvial system overlain by fluvial and peat swamp Patchawarra Formation facies which is coal bearing. Overlying the Patchawarra Formation is the fluvio-deltaic Murteree Shale and Epsilon Formation, followed by the lacustrine Roseneath Shale and the fluvio-deltaic Daralingie Formation, which is also coal bearing. Unconformably overlying the Daralingie Formation is the coal-bearing fluvial Toolachee Formation which grades into the lacustrine siltstones of the Nappamerri Group. A prominent seismic horizon which has been mapped as the P-horizon (NGMA, 2001) is situated near the top of the Toolachee Formation (Radke, 2009) and corresponds to the near-top of the Permian sequence. The Cooper Basin is overlain in the north by the Late Triassic Cuddapan Formation.

The structure of the Cooper Basin is dominated in the south and west of the basin by the northeast-trending Patchawarra, Nappamerri and Tenappera troughs (Figure 5). These troughs are separated by the Gidgealpa–Merrimelia–Innamincka (GMI) Ridge and the Nappacoongee–Murteree (NM) structural ridges. Sediment thickness is up to 2.5 km in the south, but decreases towards the north.

EROMANGA BASIN

Unconformably overlying the Warburton and Cooper basins is the Jurassic to Cretaceous Eromanga Basin. The Eromanga Basin covers an area of 1,000,000 km^2 over central-eastern Australia. It consists of fluvial and lacustrine Jurassic sediments and overlying marine and terrestrial Cretaceous sediments (Bradshaw, 1993). Sediment thickness reaches approximately 3 km in the study area (Finlayson et al., 1988) consistent with the relatively uniform infill of a vast, slowly subsiding basin.

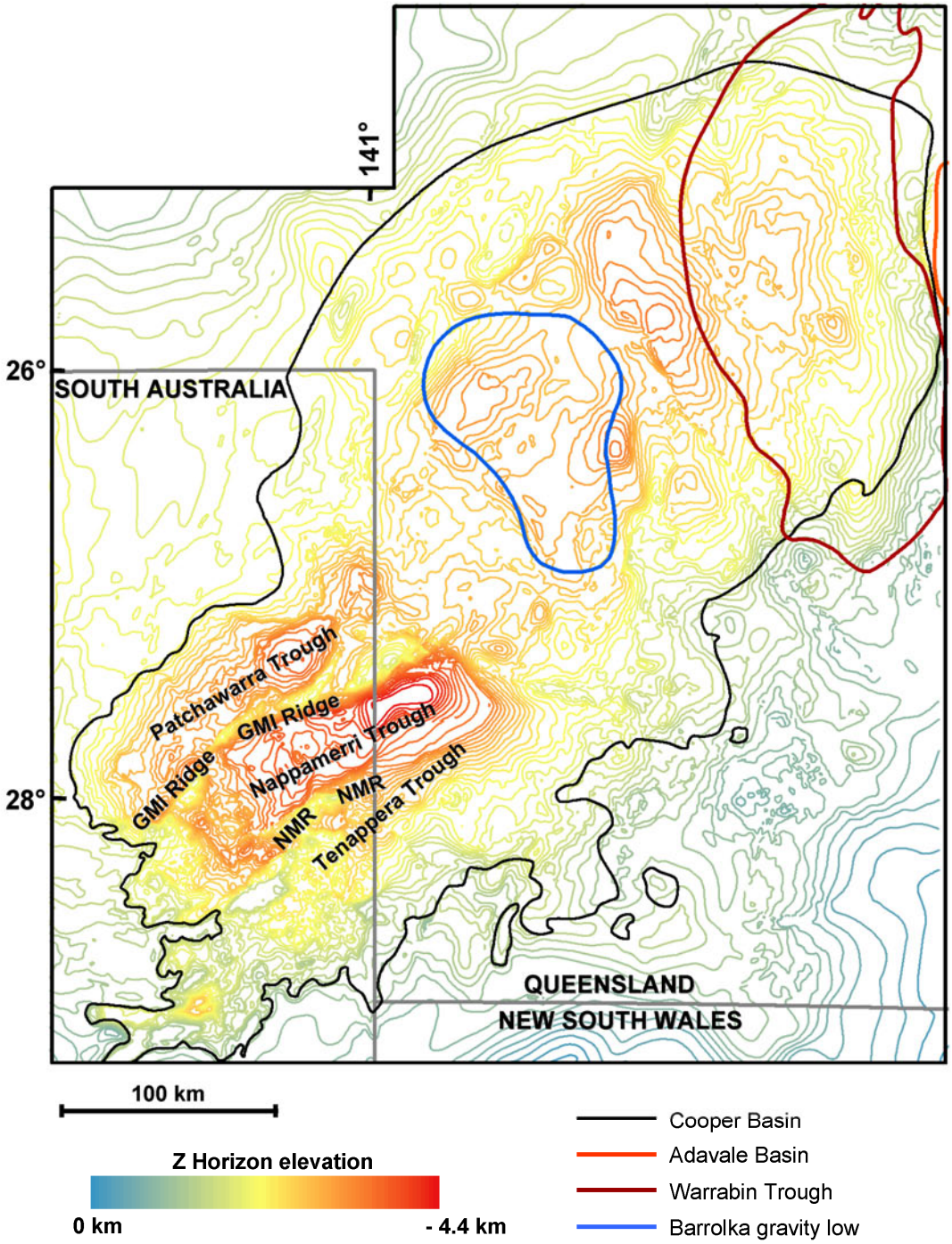

Figure 5: *Contour map of the seismic Z-horizon. The Z-horizon map was compiled from existing open file seismic sections, industry interpretations and 1300 well intersections (NGMA, 2001). Within the extents of the Cooper Basin this surface represents the base of the Cooper sequences, Outside this area it represents the base of the Eromanga sequence. The major structural elements of the Cooper Basin are labelled. GMI – Gidgealpa-Merrimelia-Innamincka; NMR – Nappacoongee-Murteree Ridge.*

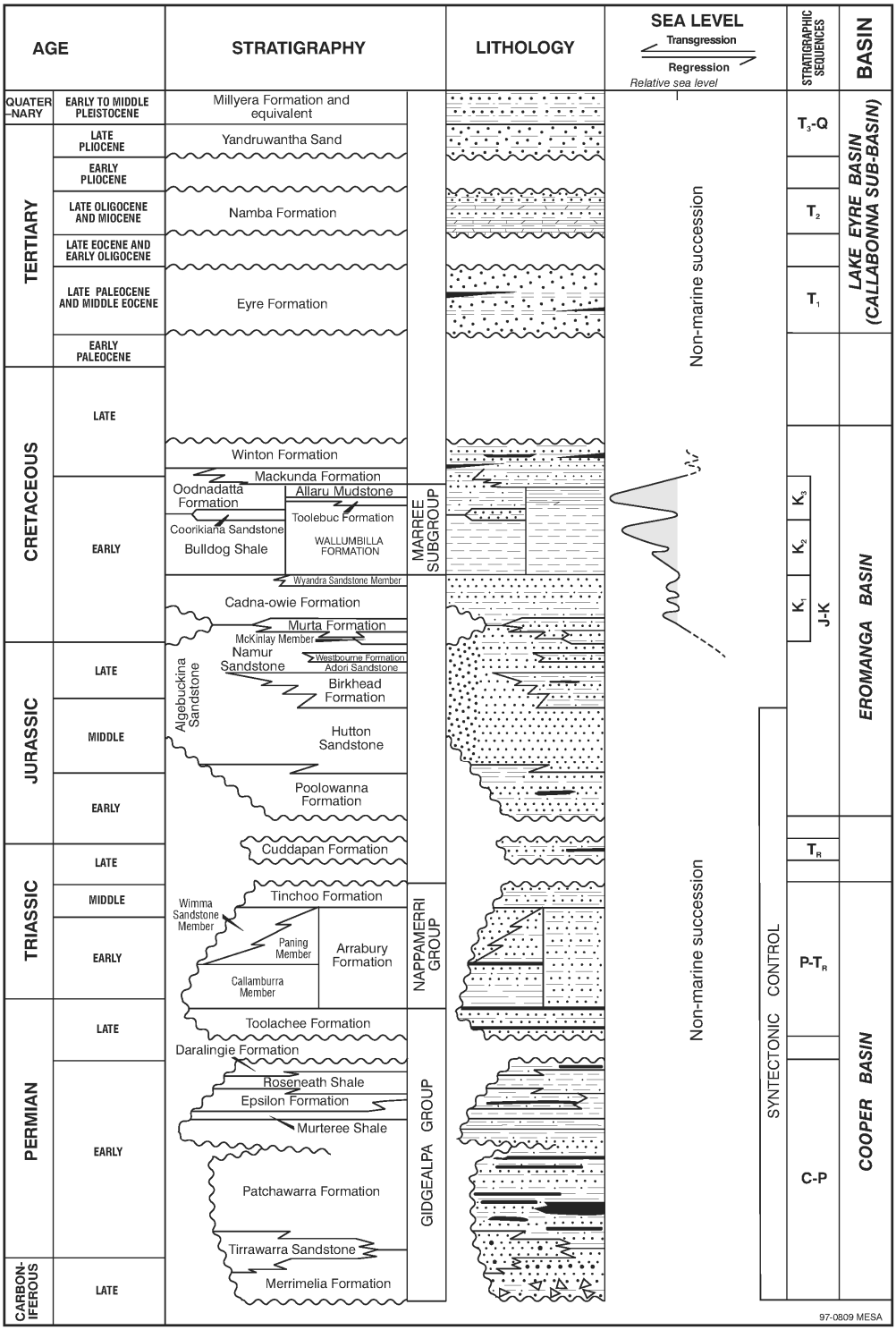

***Figure 6**: Stratigraphic summary of the Cooper, Eromanga and Lake Eyre basins. After Meixner et al. (1999).*

The Eromanga Basin stratigraphy differs slightly in different parts of the basin; however, stratigraphic units have been correlated laterally in terms of depositional environment and age (see Figure 6). In this study, we have adopted the following stratigraphy of the Eromanga Basin in the Cooper Basin region from PIRSA (2010). At the base of the sequence is the Early Jurassic

Poolowanna Formation, an aquitard unit deposited in meandering fluvial conditions. Overlying the Poolowanna Formation is the fluvial Hutton Sandstone, an aquifer consisting mostly of sandstone (Radke et al., 2000). The Hutton Sandstone is overlain by the fluvio-lacustrine Birkhead Formation, the Adori Sandstone, deposited in a braided fluvial environment, and the Late Jurassic Westbourne Formation, which was deposited in a meandering fluvial and overbank floodplain environment. Overlying these units is the Namur Sandstone, an aquifer deposited in a braided fluvial environment and the Murta Formation, a lacustrine and deltaic unit. Together these two units are laterally equivalent to the Hooray Sandstone and the Algebuckina Sandstone (Figure 6 and Radke et al., 2000).

The Namur Sandstone and Murta Formation are overlain by the Cadna-owie Formation, a sandstone aquifer near the base of the Cretaceous. The top of this formation is a prominent feature mapped as the seismic C-horizon (NGMA, 2001). Overlying the Cadna-owie Formation are the Wallumbilla and Toolebuc formations, and the Allaru Mudstone. All of these units are fine-grained, marine units. These units are laterally equivalent to the Bulldog Shale, Coorikiana Sandstone and Oodnadatta Formation. Toward the top of the sequence are the Mackunda and Winton Formations, both aquifers deposited in a marginal marine to non-marine environment.

LAKE EYRE BASIN

The Lake Eyre Basin consists of up to 400 m thick non-marine sediments that unconformably overlie deeply weathered Eromanga Basin strata. Details of Lake Eyre Basin stratigraphy are given in Callen et al. (1995) and Gravestock (1995) and shown in Figure 6.

GRANITES

A number of granites have been intersected in wells in the study area. All but one are biotite-muscovite bearing, the exception being a granite intersected in Bugerygar 1, which is of hornblende-biotite composition (Murray, 1994). A number of the granites have been isotopically dated. Table 1 summarises intrusive composition and ages of granites in the study area, excluding BLS granodiorites.

Table 1: Compositions and ages of intrusives from the study area not including the BLS granodiorite. Composition and ages based on Murray (1994).

WELL	COMPOSITION	AGE
Budgerygar 1	Hornblende-biotite granite	Unknown age
Ella 1	Biotite-muscovite granite	408 ± 2 Ma
Roseneath 1	Biotite-muscovite granite	405 ± 2 Ma
Tickalara 1	Biotite-muscovite granite	Unknown age
Wolgolla 1	Biotite-muscovite granite	Unknown age

Devonian granites

Two wells in the south of the study area intersected granites of Early Devonian age (Table 1: Roseneath 1 at 405 ± 2 Ma; Ella 1 408 ± 2 Ma; Figure 3). The two wells are located within 120 km of each other and therefore the granites may be related. These granite intersections are of similar age to the Tibooburra Granodiorite (410 Ma; Thalhammer et al., 1998) and to many other Early

Devonian granites surrounding the Darling Basin farther to the southeast (Wilcox et al., 2003). The thermal event associated with the early Devonian granite intrusion was interpreted by Draper et al. (2004) to have triggered the formation of the Adavale Basin system.

Big Lake Suite granodiorite (BLS)

Granites of the BLS have intruded into the Warburton Basin sequences and are intersected in numerous wells (Figure 3). SHRIMP U-Pb zircon isotopic analyses from samples of BLS granodiorite indicate Early Carboniferous crystallisation ages of 298 ± 4 Ma and 323 ± 5 Ma (Gatehouse et al., 1995). Erosion of the Warburton Basin sediments has unroofed the granite prior to deposition of Cooper Basin sediments (Meixner et al., 1999).

Gravity data and correlations with basin structure and basement lithology

The Gravity Anomaly Map of Australia (Bacchin et al., 2008) was inspected in order to assess the potential for using gravity data to delineate granites within basement. The gravity field is influenced by both the thickness of basin sediment and by density variation within the sediments and basement. An image of the Bouguer gravity field overlain by the major structural elements of the Cooper Basin is shown in Figure 7, while a contour map of the Z-horizon, or top of pre Cooper Basin basement, is shown in Figure 5. In the southwest of the study area two northeast to east-trending gravity lows broadly coincide with the Nappamerri and Tenappera troughs. These are bounded by northeast to east-trending gravity highs that are associated with the Gidgealpa-Merrimelia-Innamincka (GMI) Ridge and the Nappacoongee-Murteree Ridge (NMR). In the centre of the study area a structural low (Figure 5) coincides with the Barrolka Gravity Low, while a north-south trending structural low situated between the Barrolka Gravity Low and the Warrabin Trough coincides with a gravity low. The Warrabin Trough is also coincident with a broad gravity low. There is, therefore, a broad regional correlation between known basin structure as derived from drillhole intersections and reflection seismic, and the gravity field, suggesting that the distribution of low-density basin-fill is influencing the gravity field.

There is a large amount of evidence that density variations in the basement are also contributing to the gravity field. This evidence includes:

- Gravity lows that are coincident with the Nappamerri and Tenappera troughs, which extend beyond the trough boundaries (figures 5 and 7);
- The fact that the gravity low coinciding with the Patchawarra Trough is of much lower amplitude than that of the Nappamerri Trough, even though the sediment thicknesses are similar;
- A number of intense, discrete gravity lows, which lie within broader structural depressions, and in some cases coincide with granite intersections of the low density BLS (2.6 g/cm^3; Boucher, 1996);
- On the southern edge of the Tenappera Trough, a series of circular to elongate east-west gravity lows. Well intersections coincident with one of the prominent circular gravity lows correspond to two Devonian age dates (Wolgolla 1 and Roseneath 1; Figure 3 and Table 1) and a granite of unknown age (Tickalara 1).
- A number of more intense gravity lows, which are situated within the broader Barrolka Gravity Low (discussed below) and the broader gravity low associated with the Warrabin Trough;
- In the northwest and southeast of the study area where the Eromanga Basin lies directly on basement, a number of prominent gravity lows are present that are not associated with known basin structure. A granite was intersected (Ella 1; Figure 3) on one of these gravity lows.

The gravity field is therefore influenced by both the thickness of the lower density basin sediments and by density variations in the basement. It is important to constrain the influence of the basin sediments on the gravity signal so that the density variation within the basement may be analysed. All but one granite intersection occurs on localised gravity lows, the exception is a single granite intersection of unknown age (Budgerygar 1; Figure 3) in the northeast of the study area that coincides with a gravity high. The coincidence of granite intersections with localised gravity lows suggests that a large number of the localised gravity lows in the study area are due to granite intrusions within the basement.

There is no discernable gravity low associated with the Warburton Basin suggesting that the density of the basin fill is comparable to underlying basement density and cannot be delineated using gravity modelling. This higher density is consistent with the age of the basin, history of deformation and great depths of burial. The Warburton Basin is, therefore, considered basement for the purposes of the density inversion modelling.

The gravity signature of the previously identified Barrolka Gravity Low (Lake Barrolka Gravity Low – Lonsdale, 1965; Barrolka Gravity Depression – Fraser et al., 1977) is characterised by a broad anomaly within which a number of localised negative anomalies occur. The presence of thicker sequences of Cooper and Eromanga sediments due to the coincident structural low (Figure 5) will contribute to the Barrolka Gravity Low. The basin association of the well intersections (Figure 4) is disputed and are attributed to either the Barrolka Trough of the Adavale Basin System (Murray, 1994; Stewart, pers. comm.) or the Warburton Basin (McKillop et al., 2005). If the well intersections are of Warburton Basin origin, then their densities are not expected to be significantly lower than underlying basement and for the purpose of the density modelling can be considered basement. If they are of Adavale Basin System origin then their densities may be significantly lower than the basement and will contribute to the observed gravity low. As there is no depth information (seismic or drill hole) constraining the thickness of the disputed sediments, no attempt has been made to differentiate these sediments in the 3D map.

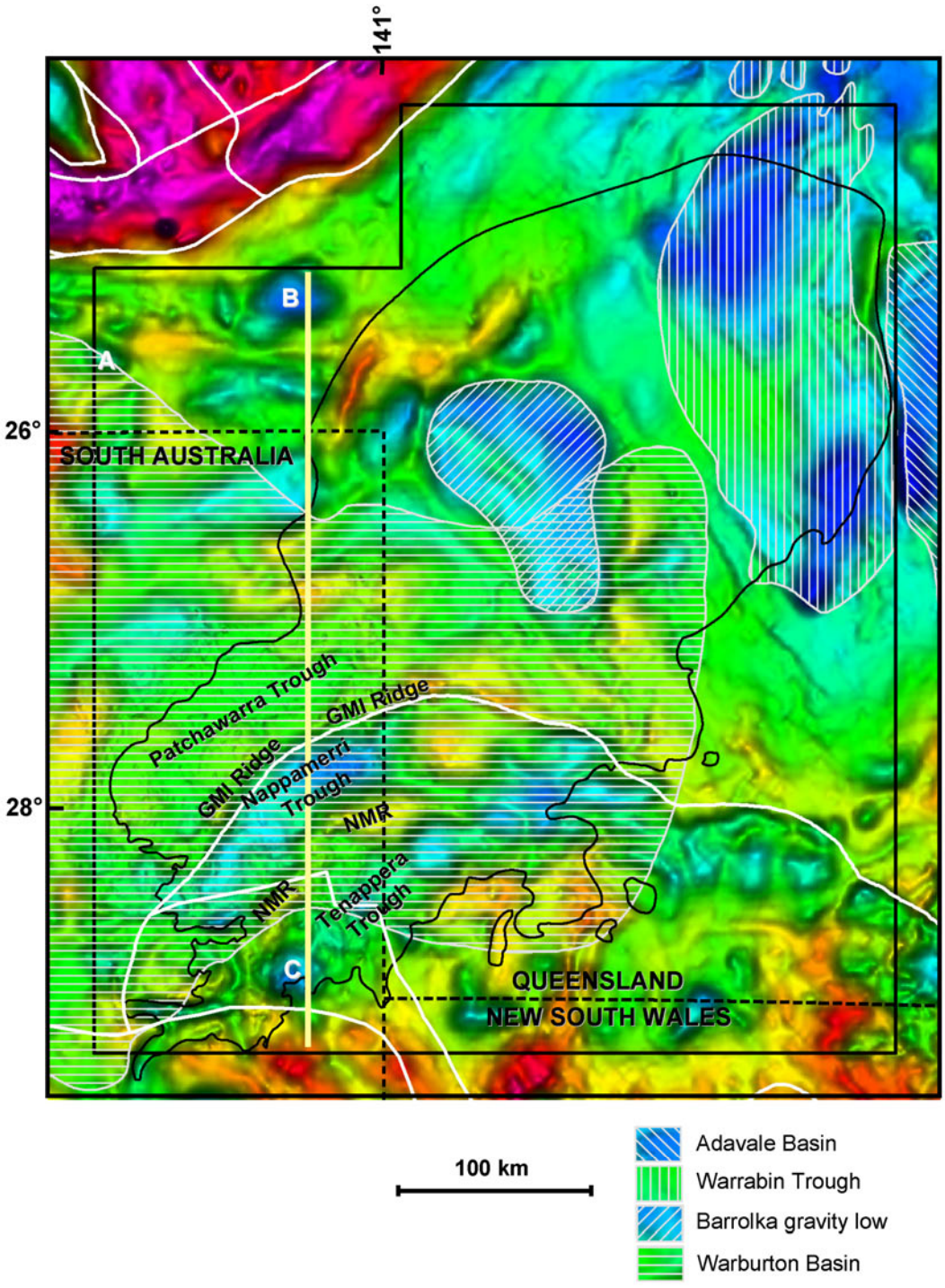

Figure 7: *Bouguer gravity anomaly image showing basin extents and the major structural elements of the Cooper Basin region (white lines, after Shaw et al., 1996). The image was created from data subsectioned from the Gravity Anomaly Map of Australia (Bacchin et al., 2008). GMI - Gidgealpa–Merrimelia–Innamincka; NMR - Nappacoongee–Murteree Ridge. Also shown are three prominent gravity lows (labelled A, B and C) that coincide with magnetic anomalies shown in Figure 8. The location of the cross-section shown in Figure 11 is indicated in yellow.*

Magnetic data and correlations with basin structure and basement lithology

The magnetic image shown in Figure 8 was produced from magnetic data sub-sectioned from the Magnetic Anomaly map of Australia (Milligan et al., 2010). The image shows a subdued signal due to the thick sequences of non-magnetic Cooper and Eromanga basin sediments attenuating the magnetic signal sourced within the basement. The exceptions are in the northwest (due to the strongly magnetic and outcropping Mt Isa Inlier), and the strongly magnetic outcropping or shallowly buried stratigraphy of the North Flinders Arm and the Wonominta Block (Figure 3) as identified in the crustal elements map (Shaw et al., 1996). All of the intense, localised gravity lows described above, with the exception of the three lows labelled in figures 7 – 8 correspond to low amplitude magnetic signatures. The labelled exceptions are: firstly, a gravity low in the northeast which coincides with a localised magnetic high (label A; figures 7 – 8), and an intense gravity low east of gravity anomaly A which coincides with a subtle positive magnetic anomaly (label B; figures 7 – 8). It is interpreted that these two magnetic features are sourced by magnetised granites. Secondly, a localised gravity low in the southwestern corner of the study area (label C; figures 7 – 8) coincides with several localised magnetic highs, which have been interpreted by Meixner et al. (1999) to be caused by magnetic basement stratigraphy overlying an intruded granite body at depth.

The observed magnetic signal is therefore interpreted to be sourced from the basement. The coincidence of granite intersections (Figure 8) with regions of subdued magnetic signal suggests that the known granites are non-magnetic. The prevalence of subdued magnetic signal in regions of positive gravity anomalies suggests that dense, non-granitic basement is also non-magnetic. The magnetic data are therefore of little use in this area discriminating granites from metamorphic basement.

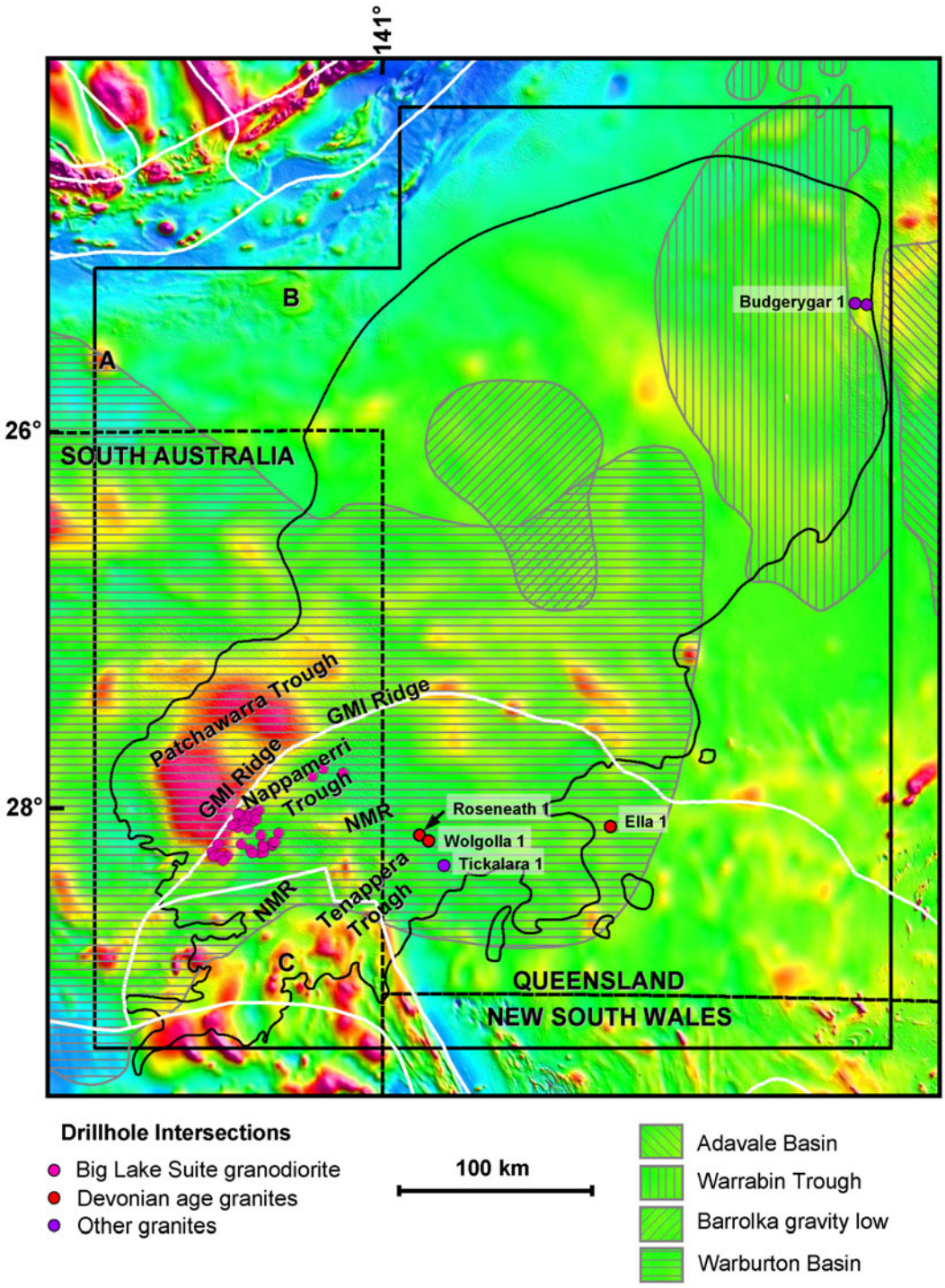

Figure 8: *Total magnetic intensity (reduced to pole) image showing drillhole intersection of granite, basin outlines and the major structural elements of the Cooper Basin (white lines, after Shaw et al.,1996). GMI – Gidgealpa-Merrimelia-Innamincka; NMR – Nappacoongee-Murteree Ridge. Also shown are three magnetic highs (labelled A, B and C) which coincide with gravity lows shown in Figure 7.*

3D map production

A 3D geological map was constructed that includes Eromanga Basin, Cooper Basin and Warrabin Trough stratigraphy, as well as sub-cropping and interpreted granites within basement. The 3D map, together with the thermal modelling results described in the following sections, are included as a digital accompaniment to this report (Appendix A) in Gocad® [2] format. The voxelised 3D map was constructed in two steps. The sedimentary section of the map, including the interface between the sediments and the basement, was defined as 3D surfaces. Depending on data availability, these were either taken from the NGMA C, P and Z seismic horizons (NGMA, 2001) or constructed in 3D-GeoModeller using drillhole intersections as constraints. The basement section of the map was then constructed from constrained gravity inversions that delineate interpreted granitic bodies within the basement. The complete set of 3D surfaces were then imported into Gocad and used to delineate regions within a voxelised volume.

The final voxelised 3D map consists of the study volume that has been padded laterally by 30 km to avoid edge effects during the gravity inversion and thermal modelling. Table 2 lists the lateral and vertical extents, as well as the cell size, of the five model volumes that were constructed. The study volume includes a region in the northwest that includes null information only. This null region corresponds to the Mt Isa Inlier, which has been excluded from this study (Figure 3).

Table 2: Lateral and vertical extents, as well as cell size, for the five models constructed as part of this study. The coordinate projection is Universal Transverse Mercator, Zone 54, Geocentric Datum of Australia 1994. The null region corresponds to the Mt Isa Inlier that has been excluded from this study.

NAME	EASTING (m)		NORTHING (m)		HEIGHT (m)*		CELL SIZE (m)	
	min	max	min	max	min	max	X and Y	Z
Study Volume	330000	800000	6760000	7316000	-13000	500	2000	100
Null Region	330000	510000	6760000	7220000	-13000	500		
3D Map	300000	830000	6730000	7346000	-20000	500	2000	100
Gravity inversion	300000	830000	6730000	7346000	-20000	500	2000	250
Regional inversion	95000	1035000	6465000	7645000	-60000	1000	5000	5000
Thermal model	310000	820000	6740000	7226000	-13000	500	2000	100
Stochastic model	310000	820000	6740000	7226000	-13000	500	2000	100

*With respect to sea level, positive upwards.

THE SEDIMENT SECTION

Eromanga Basin

The number of stratigraphic units was condensed prior to construction of the 3D map in order to reduce its complexity. The Eromanga Basin was divided into four 3D map units based on the

[2] http://www.gocad.org/

hydrostratigraphic groupings defined by Radke et al. (2000). Hydrostratigraphic groupings will allow future studies to incorporate the impact of fluid flow in transporting heat. These hydrostratigraphic groupings are also expected to represent realistic groupings based on thermal conductivities: aquitards, in general, are fine-grained units (e.g. mudstones, shales) that tend to have lower thermal conductivities than aquifer units such as coarse grained sandstones. As described in the geology section (see above), some of the Eromanga Basin units have lateral equivalents that are named differently across the basin. These were grouped together in the model. The Cuddapan Formation, located between the Eromanga and Cooper Basin sequences, reaches a maximum thickness of only 50 m (Gray et al., 2002) and was therefore not included as a separate unit. Instead it was incorporated into the basal unit of the Eromanga Basin (Westbourne 3D map unit, see below and Figure 9).

The 3D map units corresponding to the Eromanga Basin are shown in Figure 9 and have been named according to the top formation in the unit and are as follows: Surficial, which contains all units above the Allaru Mudstone; Allaru, which contains the aquitard units Allaru Mudstone, Toolebuc Formation and Wallumbilla Formation, and their lateral equivalents the Oodnadatta Formation, Coorikiana Sandstone and Bulldog Shale; Cadna-owie which contains the Cadna-owie Formation, as well as the Murta Formation and Namur Sandstone (mostly aquifers), and lateral equivalent Hooray Sandstone; and Westbourne, which contains the Westbourne Formation, Adori Sandstone, Birkhead Formation, Hutton Sandstone, Poolowanna Formation, and Cuddapan Formation (aquitards and confined aquifers).

The prominent seismic C-horizon (NGMA, 2001) was used to represent the top of the Cadna-owie Formation, and the topographic surface was taken to represent the top of the Surficial unit. 3D surfaces representing top surfaces for the Allaru and Westbourne 3D map units were constructed in 3D-GeoModeller[3] based primarily on the South Australian minerals drillhole dataset and the Queensland Petroleum drillhole dataset (Table 3). Other datasets used to constrain the surfaces include the South Australian petroleum dataset (Table 3), and the South Australian and Queensland Stratigraphic drilling datasets. However, there was considerable duplication between these datasets and the South Australian minerals and Queensland petroleum datasets, so these datasets were only incorporated when necessary.

In the Eromanga Basin (and also in the Cooper Basin), additional constraints were added to the model within 3D-GeoModeller. These additional constraints, which define the top of formations between true drillhole intersections, were added to ensure that the resulting surfaces were geologically realistic and did not intersect each other.

[3] http://www.geomodeller.com/geo/index.php?lang=EN&menu=homepage

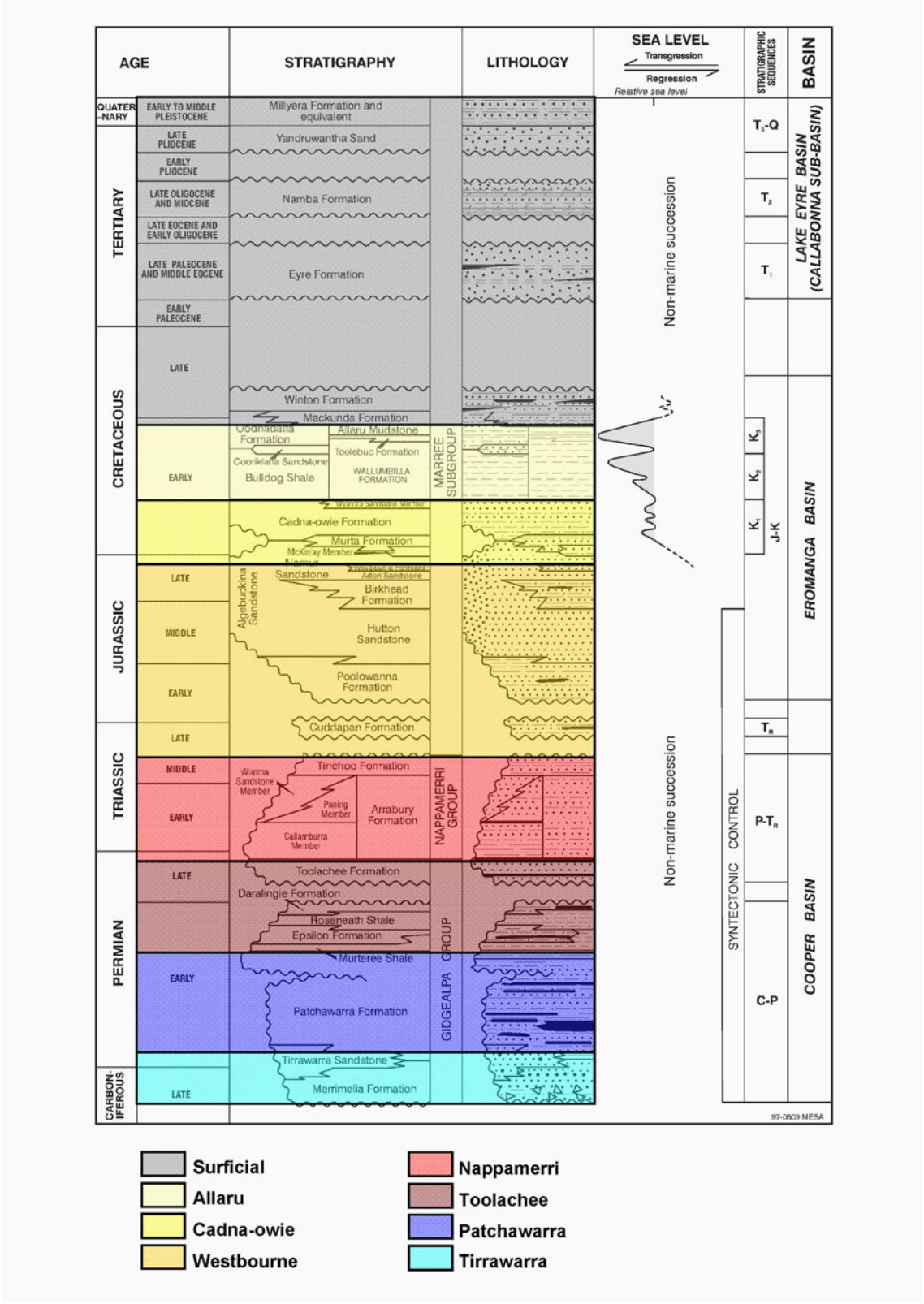

Figure 9: *Stratigraphic summary of the Cooper, Eromanga and Lake Eyre basins showing formational groupings used in the 3D geological map for the Cooper Basin region.*

Table 3: Drillhole datasets used in construction of the Cooper and Eromanga basin 3D map.

DATASET	REFERENCE
Queensland petroleum wells	Queensland Petroleum Exploration Database (QPED) http://www.dme.qld.gov.au/mines/petroleum_geoscince_data.cfm
Queensland stratigraphic wells	QPED Database
South Australia mineral drill holes	SARIG database (https://sarig.pir.sa.gov.au/Map/)
South Australian petroleum wells	PEPSA database (ftp://central.pir.sa.gov.au/petroleum/)
South Australian stratigraphic wells	SARIG database

Cooper Basin

The Cooper Basin was divided into four units based primarily on thermal conductivity data, however hydrostratigraphy was also considered. It is unlikely that the permeability and thickness of any of the Cooper Basin units would be sufficient to sustain enough fluid flow to noticeably impact the temperature profile, however, the 3D map groupings allow for this to be considered in future studies. The 3D map units in the Cooper Basin (shown in Figure 9) are: Nappamerri, containing the moderately thermally conductive Nappamerri Group; Toolachee, containing the low thermal conductivity Toolachee and Daralingie formations, Roseneath Shale, Epsilon Formation and Murteree Shale; Patchawarra containing the higher thermal conductivity Patchawarra Formation; and Tirrawarra containing the higher thermal conductivity and higher permeability Tirrawarra Sandstone and Merrimelia Formation.

As with the Eromanga Basin units, formation top surfaces were constructed in 3D-GeoModeller for most of the stratigraphic groupings using mainly the South Australian minerals drillhole dataset (Table 3) and the Queensland Petroleum drillhole dataset (Table 3), with data from the South Australian petroleum dataset, and the South Australian and Queensland Stratigraphic drilling datasets incorporated as necessary. The seismic P-horizon (NGMA, 2001) was used to represent the top of the Toolachee Formation (Figure 10A), and the seismic Z-horizon (NGMA, 2001) was used for the top of basement (equivalent to the base of the Cooper and Eromanga basin sequence; Figure 10B).

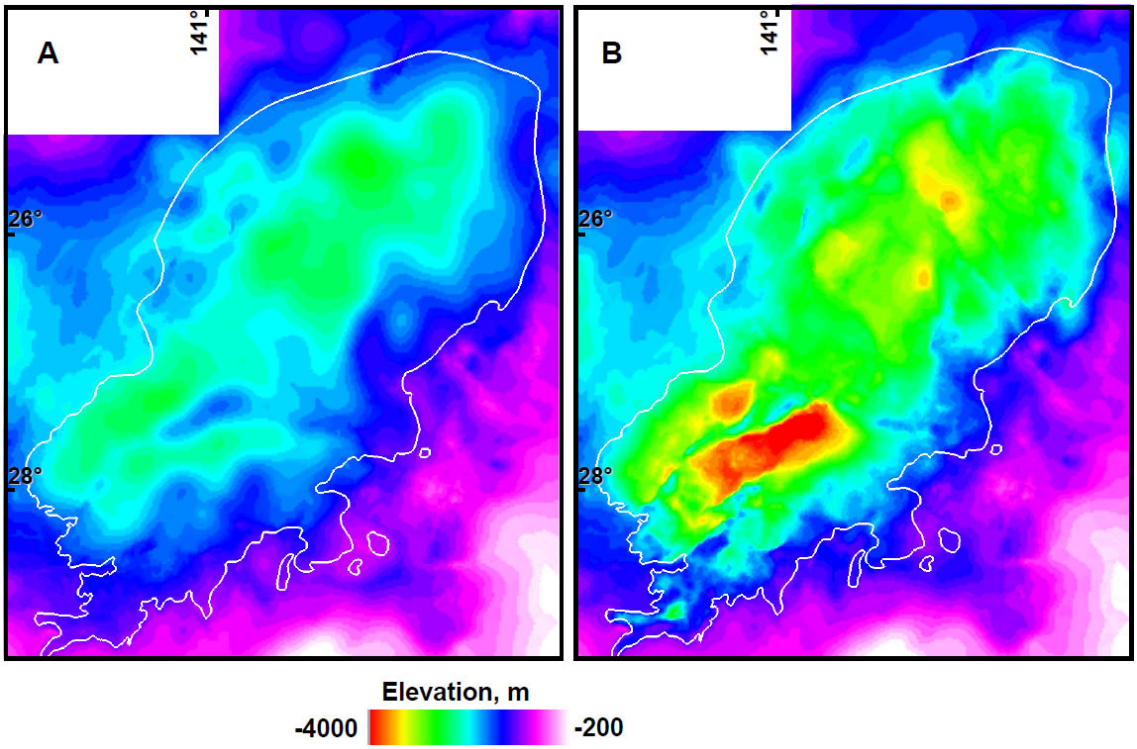

Figure 10: *A. Depth to the base of the Eromanga Basin from 3D map. B. Base of Cooper-Eromanga Basin sequence from the 3D map. Cooper Basin outline shown in white.*

Warrabin Trough

The Warrabin Trough was included in the 3D map as a single unit. Its distribution was constrained by three east-west interpreted seismic sections, which transect the north, central and southern portions of the Devonian age sediments of the Warrabin Trough. The seismic traverses were acquired in 1980 by the Bureau of Mineral Resources in cooperation with the Geological Survey of Queensland (Passmore and Sexton, 1984). These sections, which provide estimates of the sediment thickness, have been combined with an outline of the basin (Raymond and Totterdell, 2012) to constrain the location and geometry of the base of the Warrabin Trough.

THE BASEMENT SECTION

3D gravity inversions

Interpreted granitic bodies were delineated from low density regions within the basement through two stages of 3D gravity inversion modelling. The first stage involved performing inversions to constrain the contribution of the basin sediments to the gravity signal. The second stage involved the use of gravity 'worm' data (Archibald et al., 1999) to constrain the basement density distribution. During this second stage, surfaces were generated enclosing low density regions in the basement which are interpreted as granitic bodies.

The inversion programs utilised were developed by the University of British Columbia – Geophysical Inversion Facility (UBC-GIF) (Li and Oldenburg, 1998a). Iterative gravity inverse modelling is a process whereby adjustments are made to a density model, in the form of a mesh of

rectangular prisms, until there is an acceptable fit between the predicted response of the model and the observed gravity data (Meixner and Lane, 2005). When geological and physical property observations are available, it is possible to make a reference model that will include geologically-sensible variations in the physical properties. The inversion can be forced to honour the supplied property values to within a specified upper and lower bound, at specific points within the model. The inversions were run on the National Computational Infrastructure facility at the ANU (NCI high performance computing centre).

The gravity inversions were conducted on the study volume consisting of a mesh with a 2 km lateral and 100 m vertical cell size (Table 2). The resolution that can be achieved through inversion is ultimately dependent on the spacing and accuracy of the input gravity data. Given an average spacing between gravity observations of 4 to 7 km (Bacchin et al., 2008), it is unlikely that using cells smaller than 2 km in the lateral dimension would produce any additional information. The 100 m vertical cell size was to accommodate the high resolution of the Eromanga and Cooper basin stratigraphic horizons that were used to constrain the inversion model. The response of material beyond the limits of the inversion mesh was removed using the method described by Li and Oldenburg (1998b).

Stage 1: Constraining the contribution of basin sediments

An initial constrained gravity inversion was performed on the sedimentary section (Eromanga, Cooper and Warrabin Trough) of the 3D map in order to constrain the contribution of the sediments to the gravity anomaly signal. Density data to constrain this inversion were obtained from down-hole density logs from wells in the study area (Table 4). The values for individual stratigraphic units were combined into averaged values based on the groupings shown in Table 5. Eromanga Basin units were combined into two groupings due to the limited number of density values available in the Eromanga Basin. No density information was available for the Warrabin Trough and so an average value of all Cooper Basin densities (2.59 g/cm^3) was used as a proxy value. A 'typical' value for granites of 2.64 g/cm^3 (Telford et al., 1990) was used in the stage 2 inversions.

As gravity anomaly data are used in the inversion, and the regional gravity field has been removed (Table 2), the densities used in the reference model must be converted to relative densities by adjusting them so that the average density of all cells in the model equals zero. To do this requires estimating the average density of the final model. To do this, an average basement density is assumed excluding potential granites which are to be extracted from the final inversions, of 2.75 g/cm^3. This is considered to be a reasonable value for upper crustal lithologies that exclude granite and sediment lithologies (Korsch et al., 2012). A basement to granite volume ratio of 0.25, and a granite density of 2.64 g/cm^3, is also assumed. At this stage these values are not critical and are used to define a baseline density for the entire model. Combining the 2.75 g/cm^3 basement density with the 2.64 g/cm^3 for granite at the 0.25 ratio results in a value of 2.72 g/cm^3, which was used as the combined granite and basement density. After assigning the densities listed in Table 5 for the basin units, as well as the 2.72 g/cm^3 for the combined granite and basement, an average value of 2.69 g/cm^3 was calculated for the entire model voxet. This value is then subtracted from all of the previously assigned densities. For example, the absolute density of the Patchawarra Formation is 2.53 g/cm^3. Subtracting 2.69 g/cm^3 gives a relative density for the Patchawarra Formation of -0.16 g/cm^3. The inversion was forced to honour the sediment densities to within ± 0.15 g/cm^3. Although a density was assigned to the combined granite and basement volume (a relative value of 0.03 g/cm^3), the corresponding upper and lower bounds (absolute values of 2.4 to 3.5 g/cm^3) were set such that they encompass all likely rock densities (Emerson, 1990). Figure 11 shows a

cross-section through the inversion model showing densities tightly constrained in the sedimentary section, but loosely constrained in the basement section of the model.

Table 4: Average densities from downhole density logs.

FORMATION	AVERAGE DENSITY (g/cm^3)	BIG LAKE 001	BIG LAKE 002	BIG LAKE 003	MOOMBA 009	MOOMBA 010	MERRIMELIA 005	DULLINGARI 005	MOORARI 002	MURTEREE 001	NAMUR 001	TOOLACHEE 006
Mackunda Formation	2.20							2.20				
Oodnadatta Formation	2.16							2.16				
Coorikiana Sandstone	2.14							2.14				
Bulldog Shale	2.39							2.39				
Cadna-owie Formation	2.41							2.41				
Hutton Sandstone	2.48		2.50				2.42		2.52	2.48		
Poolowanna Formation	2.49	2.53	2.42	2.48	2.42				2.49	2.61		
Nappamerri Group	2.70	2.74	2.68	2.78	2.70	2.66	2.65		2.6	2.74	2.71	2.62
Toolachee Formation	2.49	2.52	2.44	2.58	2.47	2.60	2.37		2.45	2.50	2.52	2.44
Daralingie Formation	2.54	2.61	2.33	2.68	2.52							2.54
Roseneath Shale	2.70	2.72	2.66	2.80						2.62		2.64
Epsilon Formation	2.59	2.54	2.55	2.68					2.55	2.64		2.56
Murteree Shale	2.73	2.74	2.68	2.84					2.69	2.72	2.69	2.68
Patchawarra Formation	2.54	2.49		2.60			2.52		2.51	2.57	2.53	2.48
Tirrawarra Sandstone	2.40	2.41		2.32			2.47					
Merrimelia Formation	2.63			2.63			2.58		2.65	2.67	2.66	
Big Lake Suite	2.59	2.59										
Innamincka Formation	2.49						2.49					
Lycosa Formation	2.73									2.73		2.66

In order to assess the effectiveness of the inversion in separating the gravity signal due to the sediments from that due to basement, we have forward modelled the above density constrained inversion model, with the basement density set to a constant value (Figure 12A). The modelled gravity response should therefore reflect density and thickness variations in the sediments only. Figure 12B is a residual gravity image where the signal in Figure 12A has been subtracted from the observed gravity field. This, if the density contribution of the sediments has been successfully accounted for, is then the gravity signal contribution from the basement. Given that there is poor correlation between the two figures, and that in Figure 12B there are no remaining gravity lows associated with areas of greatest sediment thickness (see Figure 5), it appears that the gravity signal due to the sediments has been accounted for successfully in the density constrained inversion model. It is noted that the range in Figure 12B (~700 g.u.) is considerably higher than that in Figure 12A (~400 g.u.) suggesting that in the Cooper Basin region, density variations within basement have a stronger impact on the gravity signal than variations in the thickness of the sediments.

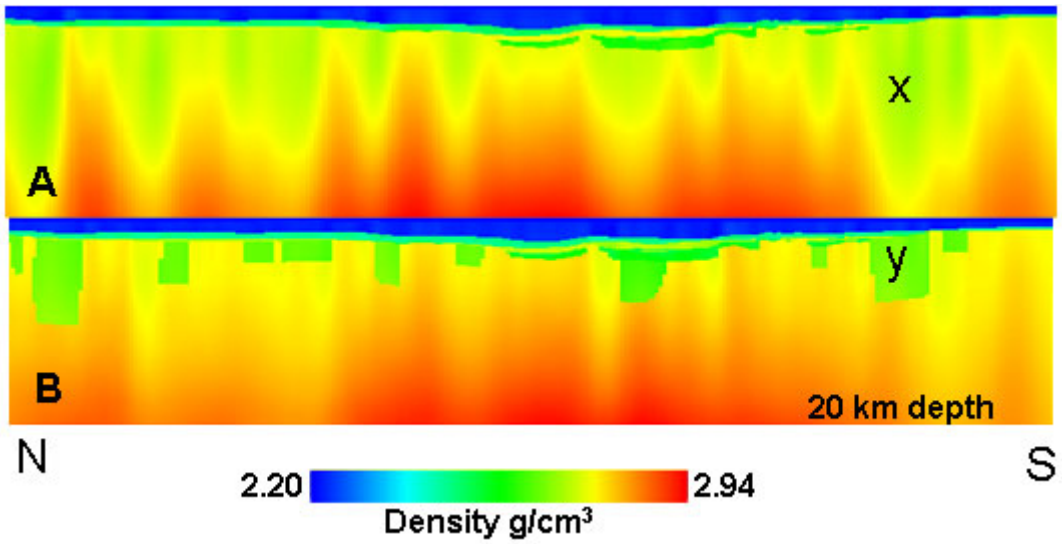

Figure 11: *North-south cross-sections through the gravity inversion density model. A. The sediment-constrained model where the densities of the sedimentary section of the model are tightly constrained, while the densities of the basement section of the model are unconstrained. The low density lobes beneath the sediments are clearly visible (x). B. The final depth optimised density model showing the variability of the depth extent of the interpreted granite bodies (y). See Figure 7 for section location.*

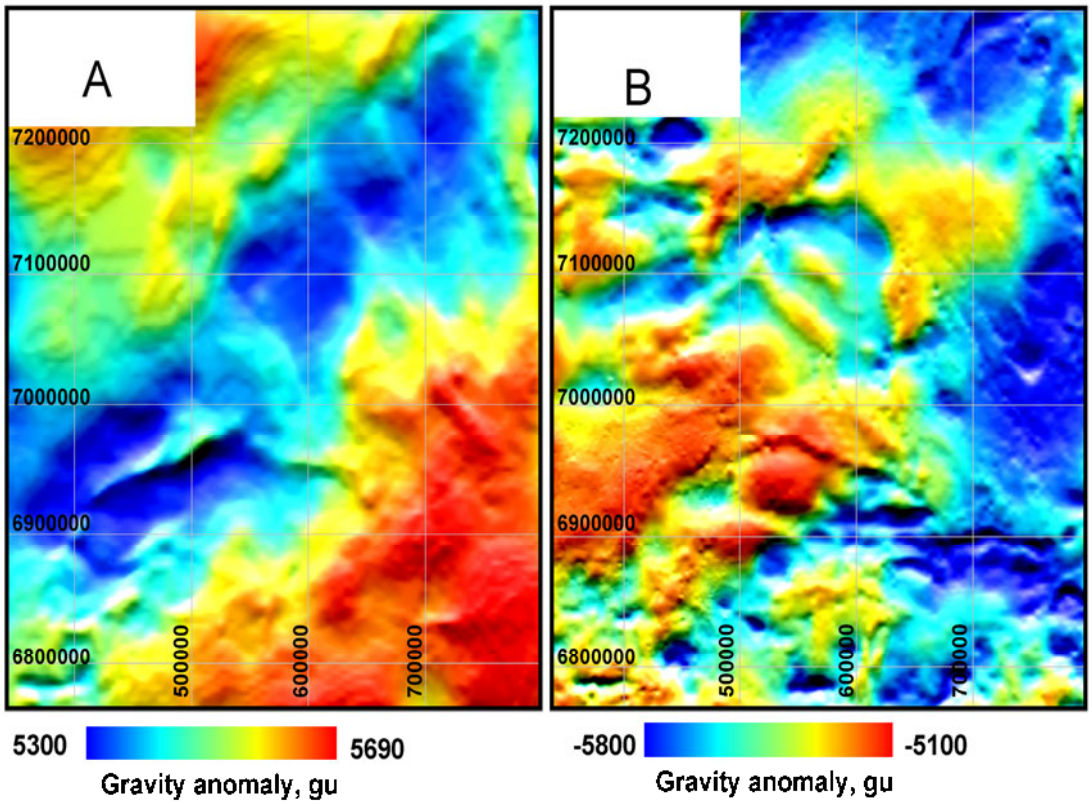

Figure 12: *A. Forward modelled gravity response due to the sediments alone. The basement has been assigned a constant density of 2.72 g/cm^3 (a relative density of 0.00 g/cm^3). B. Residual gravity image where the gravity response of the sediments has been subtracted from the observed gravity field. The residual range reflects the influence of variable basement density on the overall gravity field.*

Table 5: Average densities for the 3D map units compiled from the data in Table 4. The upper Eromanga Basin map units (Surficial and Allaru) were assigned an average density from the Mackunda Formation, Oodnadatta Formation, Coorikiana Sandstone, and Bulldog Shale. The lower Eromanga Basin map units (Cadna-owie and Westbourne) were assigned an average density from the Hutton and Poolowanna formations. All other map units were assigned average values based on the stratigraphic formations they encompass.

3D MAP UNIT	DENSITY (g/cm^3)	STANDARD DEVIATION (g/cm^3)
Surficial	2.22	0.12
Allaru	2.22	0.12
Cadna-owie	2.46	0.06
Westbourne	2.46	0.06
Nappamerri	2.69	0.06
Toolachee	2.59	0.08
Patchawarra	2.53	0.04
Tirrawarra	2.55	0.13

Stage 2: Building the 3D granite-constrained map

The sediment constrained stage 1 inversion model shows the relative basement densities smoothly varying from high to low values. Discrete boundaries, however, can be constructed by producing 3D contour surfaces, termed iso-surfaces. A series of iso-surfaces was generated, based on a range of density values, enclosing successively larger volumes of low densities. The geometry of these iso-surfaces is lobe-like with the maximum lateral extent at or near the top of the basement and gradually reducing in lateral extent at depth.

Gravity 'worming' or multi-scale edge mapping was performed on the residual gravity data (Figure 13). The worming process described by Archibald et al. (1999) maps the edges of source bodies from gravity or magnetic data at a variety of scales. The worms are generated from the maxima in the horizontal gradient and approximate the position of the density contrast at the edge of a vertically dipping body. Worms are generated for several levels of upward continuation. Upward continuation is a process that can be applied to potential field data whereby the signal is recalculated to the signal that would be observed at higher levels above the ground surface. Higher upward continuation levels enhance long wavelength features that are often a result of deeper source features, whereas low levels retain short wavelength features. The higher upward continuation level worms will, therefore, approximate the lateral sub-sediment extent of discrete low density bodies within the basement. Only those iso-surfaces with sub-sediment lateral extent that matched the higher (i.e., deeper) levels of the worm data were selected and used to differentiate these discrete low density bodies from the surrounding high density basement.

The selected lobe-like iso-surfaces extend to differing depths, with the more intense gravity lows producing lobes with total depth extents of up to 15 km. These low density lobes are ultimately to be interpreted as granites. As such, granites with these larger depth extents are considered geologically unrealistic and were restricted by specifying a maximum cut-off depth. The value of this maximum cut-off depth was determined by running six further inversions. Each inversion used a different maximum cut-off depth with values of 2, 4, 6, 8, 10, 12 and 14 km.

For this new series of inversions, the relative density values assigned to the reference model were recalculated. This was done as the lower density interpreted granite bodies had now been separated from the basement. In successive inversions, granite densities were tightly constrained to 2.64 g/cm^3. It is important to get the relative density values as accurate as possible, because the difference in density between the 'averaged' basement and the assigned granites controls the final depth extent of the granite bodies; the larger the density difference, the smaller the final depth extent. A value of 2.75 g/cm^3, the assumed average basement density, was subtracted from the absolute density values to convert the density model from absolute to relative densities. For example, the absolute density of the Patchawarra Formation was 2.53 g/cm^3, subtracting the 2.75 g/cm^3 value results in a relative Patchawarra Formation density of -0.23 g/cm^3. The inversion was forced to honour the densities of the sediments and the interpreted low density granite bodies to within ± 0.15 g/cm^3 by specifying upper and lower bounds in the reference model. Although a density was assigned to the basement (a relative value of 0.0 g/cm^3), the corresponding upper and lower bounds (absolute values of 2.4 to 3.5 g/cm^3) were again set such that they encompassed all likely rock densities (Emerson, 1990).

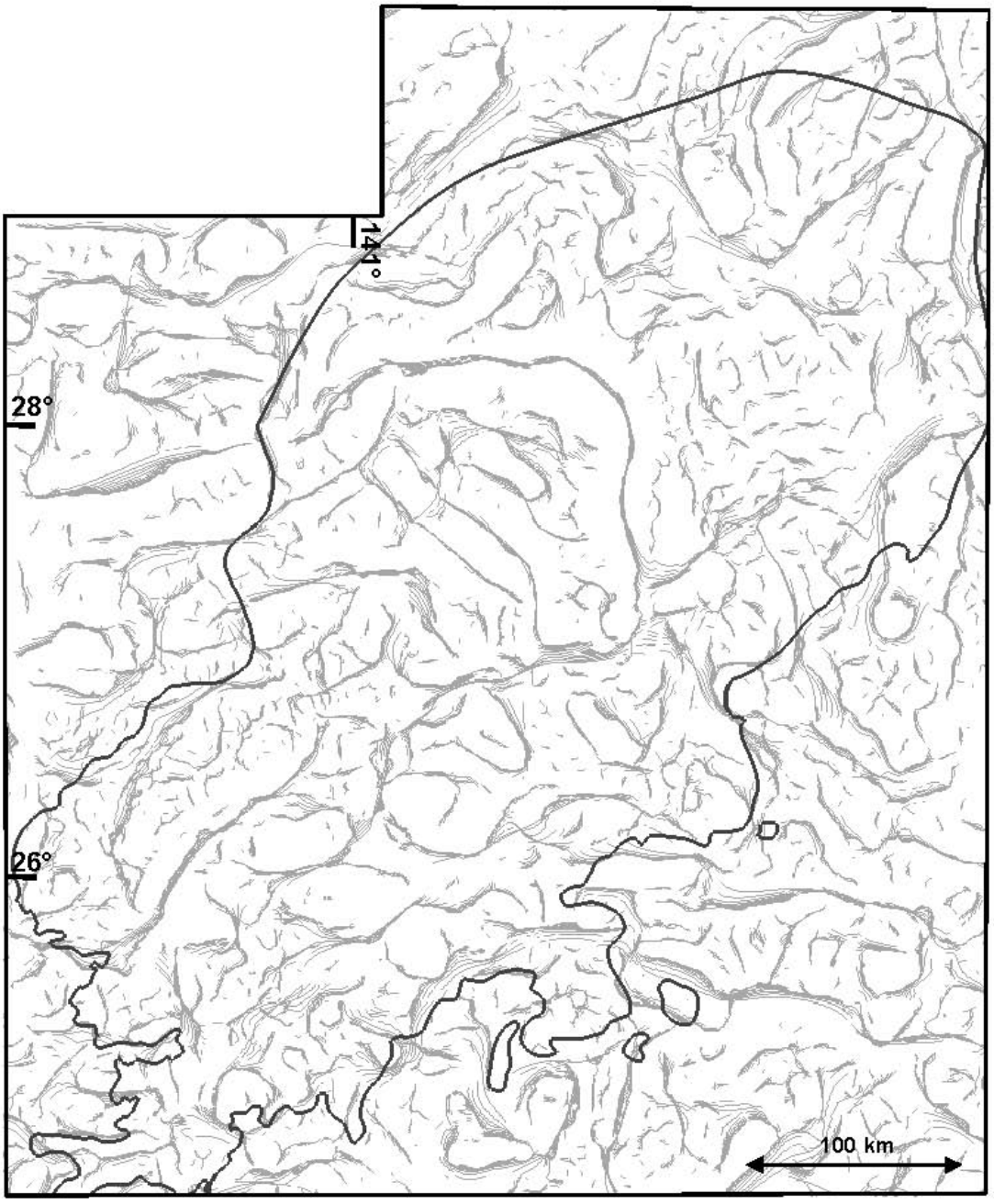

Figure 13: *Gravity worms (light grey; see text for details) generated over the study area, which are used to help constrain the lateral sub-sediment extent of the low density bodies. Dark grey line shows extent of the Cooper Basin.*

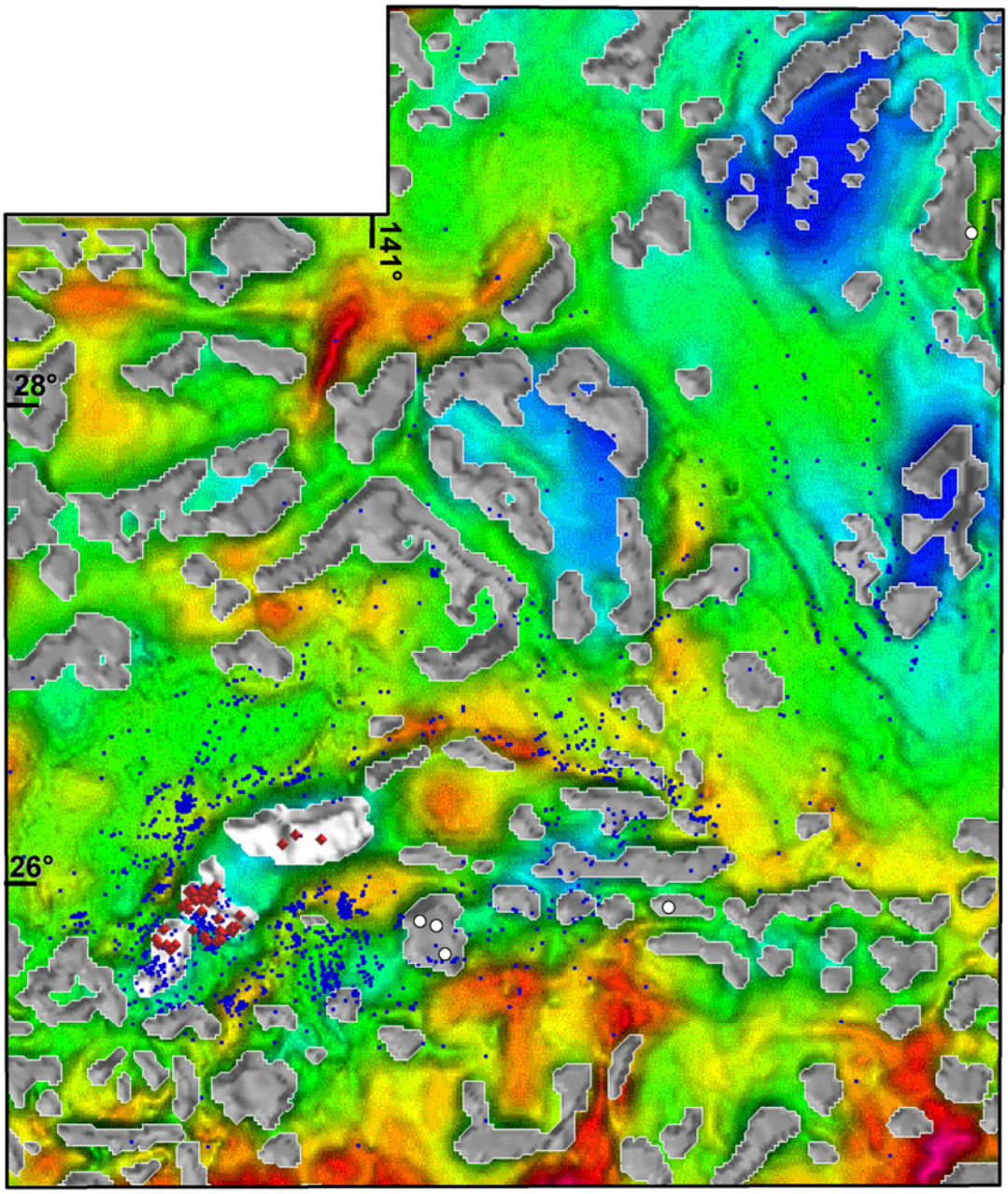

Figure 14: *Set of iso-surfaces created from the final gravity inversion density model draped over a gravity image (grey – undivided granites; white – BLS granodiorite). The red diamonds show BLS granodiorite intersection; the white circles show other intersected granites; the blue dots show locations of temperature measurements.*

Results of the six inversions were analysed by inspecting the regions of the basement immediately below the base of the modelled low density interpreted granitic bodies. If the density of the granite in the reference model was too high and/or its depth extent was too small, then the inversion result incorporated an anomalous region of low density in the basement directly beneath the modelled granite in order to satisfy the observed data. Conversely, if the density of the modelled granite in the reference model was too low and/or the depth extent too large, then an anomalous region of high density was generated at the base of the granite. A new density model was produced that

amalgamated the optimum cut-off depths for each of the six inversion models into a single granite depth optimised density model. A final inversion was run on this optimised model and the results are shown in Figure 11B. A new set of iso-surfaces was generated from this optimised model. These iso-surfaces (Figure 14) show the base of the interpreted granitic bodies situated beneath the Cooper and Eromanga basins. There is a good correspondence of the interpreted granite bodies with the granite intersections from drill-hole data.

Temperature and heat flow data

The OZTemp (2010) database is an updated and improved version of the AUSTHERM05 borehole temperature database previously described by Chopra and Holgate (2005). OZTemp contains temperature and geothermal gradients collected from drillholes around Australia. Using measured and estimated thermal gradients, surface temperature estimates and depth to basement information, these temperatures have been vertically extrapolated to 5 km depth. The interpreted temperatures at 5 km were gridded to produce a map of crustal temperature at 5 km across the Australian continent. An image of the temperature at 5 km in the study area is shown in Figure 2 and highlights the large number of downhole temperature measurements in the region, a legacy of the numerous hydrocarbon exploration and production wells in the Cooper Basin. Beyond the extents of the Cooper Basin, the data distribution is heterogeneous, with the highest data density in the known petroleum provinces. Conversely there are some areas of very sparse data spacing which require large interpolations to produce a continuous grid. The resulting temperature predictions in these areas are often unreliable and unconstrained. Furthermore, while the data has had a quality assessment performed on it, many of the temperature measurements are still of unknown quality. Many of the measurements were performed soon after (or during) drilling, and will therefore be unequilibrated and do not reflect the true formation temperature. In some cases, corrections have been applied to account for this, but for many of the measurements this was either not possible or the equilibration status of the hole was simply not known.

The predicted temperature at 5 km image of the entire Australian continent (Figure 2 inset) shows a larger region, extending beyond the study area that has elevated temperatures. Within the study area a broad region of elevated temperatures corresponds to the Cooper Basin. More localised elevated temperatures (e.g., Bulyeroo 1, 222 °C at 3.55 km) occur in the southwest of the Cooper Basin, coinciding with the Nappamerri Trough and well intersections of the BLS. Another broad region of elevated temperatures coincides with the Barrolka Gravity Low and the Warrabin Trough (Figure 2). The remaining larger amplitude temperature anomalies are not as well constrained. They include areas: to the north of the Barrolka Gravity Low; within the Warrabin Trough; directly to the north of the Warrabin Trough; in the northwestern corner of the study area; and on the western edge of the study area. There are no identified temperature anomalies coinciding with the Devonian age granite intersections.

The only heat flow determinations in the study area occur in a localised area in the Nappamerri Trough region (Figure 2). The heat flow determinations were published by Beardsmore (2004), who used temperature logs from 12 wells in a Geothermal Exploration Lease (Geodynamics Limited, GEL99) to generate one dimensional heat flow models. The resulting heat flow values in the lease area are fairly high with an average of 100 mW/m^2 and a standard deviation of 6 mW/m^2.

Thermal conductivity data

A total of 98 thermal conductivity measurements have been compiled from the study area (Gallagher, 1987a; Weber and Kirkby, 2011). Of these, 88 are from Cooper and Eromanga basin units, and ten are from granite or basement units. With the exception of the top two 3D map units (Surficial and Allaru – see the section 3D Map Production) there are at least nine measurements from each 3D map unit, and therefore it is theoretically possible to simply take an average for each unit. However the available measurements do not sample the correct proportions of all lithologies present. For example, the Patchawarra Formation is approximately 6% coal, but no thermal conductivity measurements are available for coal in the Patchawarra Formation. Given that coal has a considerably lower thermal conductivity (~0.3 W/mK) than most rocks (2 – 5 W/mK), adding 6 % coal to a unit will have a substantial impact on the overall thermal conductivity. Therefore, to produce a more representative estimate of the mean value and standard deviation of thermal conductivity for each unit in the 3D map, we followed the process described below.

PROCESS OVERVIEW

The aim of the process was to provide as accurate a description as possible of the thermal conductivity distribution in the Cooper Basin region. Firstly, the thermal conductivity of each major rock type (e.g., sandstone, shale, coal etc) was characterised for each unit in the 3D map. Secondly, the composition of each map unit was characterised in terms of the percentage of each major rock type. Finally, the thermal conductivity and compositional data were combined to determine the thermal conductivity of the 3D map unit.

To calculate and combine the thermal conductivity and compositional data, a Monte-Carlo approach was taken, similar to that followed by Haynes (in prep). Instead of relying on single values (for example, the mean of a population), the Monte-Carlo approach takes a population of values as an input, and returns a population of possible values as an output. The primary reason for using this approach is that it provides a way of accurately representing the rock types present in each unit and their errors. For example, bimodal, normal, log-normal, and other probability distributions can be represented, without the necessity to force these distributions into a single probability distribution model (e.g. normal distribution). Given the large number of drillholes present in the Cooper region, all of which provide stratigraphic information (which then provide information on the distribution of rock types), a Monte-Carlo approach is justified.

The Monte-Carlo approach takes a population of possible values for each parameter that is to be combined. In the situation addressed here where thermal conductivity and rock type percentages are combined, populations were generated for each unit in the 3D model (see section 3D Map Production) using (a) possible thermal conductivity values for each rock type, and (b) possible percentages of rock types. The process for generating these populations is described in the following section. These populations were then combined by first, randomly picking one set of thermal conductivity values (one value for each rock type) from population (a) and then randomly picking a set of proportions from population (b), and second, calculating an overall thermal conductivity value based on those two sets using a weighted harmonic mean. This process was then repeated until a population of 5000 thermal conductivity values had been produced for each unit in the 3D map.

CHARACTERISATION OF THERMAL CONDUCTIVITY OF DIFFERENT ROCK TYPES

In order to characterise the thermal conductivity of each major rock type, the thermal conductivity measurements were first categorised according to lithology, and then by which unit in the 3D map they fell within. For example, thermal conductivity measurements on shale in the Westbourne Formation would be grouped with thermal conductivity measurements on shale in the Birkhead Formation, as these two formations are in the same unit in the 3D map (Westbourne). Thermal conductivity measurements on shale in the Toolebuc Formation (in the 3D map unit Allaru), however, would be grouped separately.

The next step was to take an average of the thermal conductivity values based on a log-normal distribution. A log-normal distribution is believed to produce the most accurate model of thermal conductivity distribution. This assumption is supported by the histogram of thermal conductivity measurements from the Geoscience Australia (GA) database (Weber and Kirkby, 2011) shown in Figure 15 where the log-normal distribution fits the data more accurately than a normal distribution.

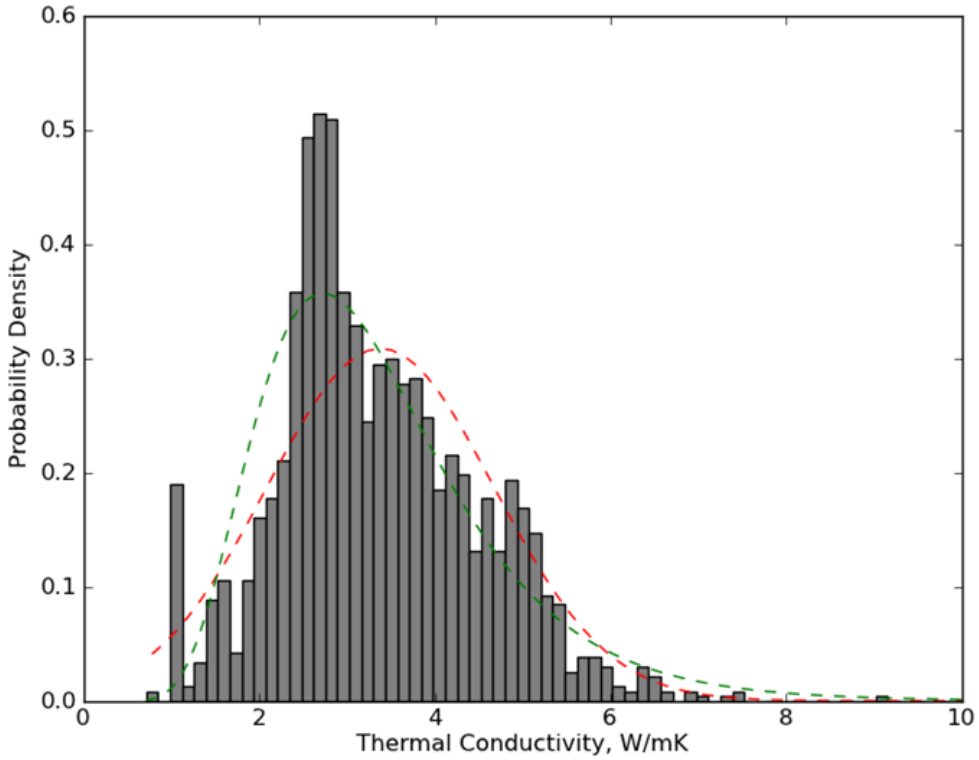

Figure 15: *Normalised probability distribution for all saturated thermal conductivity measurements contained in the GA database (n=1742). Red dashed line shows a normal distribution, the green dashed line shows a lognormal distribution.*

Thermal conductivity values were then averaged using the following criteria. If there were three or more thermal conductivity measurements for a given rock type in a given map unit, a harmonic mean and standard deviation was calculated from these values. Where there were fewer than three values for a rock type in a given map unit, the thermal conductivity measurements for that rock type were grouped with all other thermal conductivity values from that rock type in the basin which they

fell within, and averaged. If there were fewer than three values for the rock type in the entire basin sequence, then a published value was taken for that rock type. For coal, published values were taken from Herrin and Deming (1996) which contains measurements on coal samples from the United States of America. For all other rock types, published values were taken from Weber and Kirkby (2010), which contains measurements on various rock types from across Australia. Finally, a population of 5000 thermal conductivity values were generated for each rock type in each 3D map unit, by random sampling from a normal distribution defined by the mean and standard deviation values obtained above.

CHARACTERISATION OF LITHOLOGY PROPORTIONS

The proportion for each major lithology in each stratigraphic unit was estimated using one of the following two methods, depending on data availability:

For 3D map basin units containing only one stratigraphic unit (Nappamerri and Patchawarra), the proportion of major lithologies were either estimated based on lithological descriptions of the formation or obtained from the Department of Primary Industry and Resources of South Australia (now the Department for Manufacturing, Innovation, Trade, Resources and Energy (DMITRE)) electrofacies maps (PIRSA, 2004). See Table 6 for details of data sources. For the remaining 3D map units, which contain multiple stratigraphic units, a different process was applied:

- Firstly, for each stratigraphic unit, a mean and the standard deviation value for the percentage of each major lithology was either estimated based on lithological descriptions (see Table 6 for references) or obtained from the PIRSA electrofacies maps (PIRSA, 2004);
- Secondly, possible proportions for each rock type in the stratigraphic unit were obtained by taking random values from a normal distribution described by the mean and standard deviation values estimated above (excluding negative values and values greater than 100 %). For example the Allaru Mudstone was estimated to contain 10 ± 10 % sandstone, 70 ± 20 % mudstone and 20 ± 15 % siltstone, so a possible composition could be 12 % sandstone, 65 % mudstone and 23 % siltstone. Where the percentages did not add up to 100 % they were renormalised to 100 %.
- Thirdly, a drillhole was selected randomly from the Queensland/South Australia database (see Table 3), and used to assess the thickness of each stratigraphic unit as a proportion of the total thickness of the 3D map unit. For example, at Queensland drillhole ALLANDALE_1, the map unit Allaru contains approximately 42 % Allaru Mudstone, 3 % Toolebuc Formation and 55 % Wallumbilla Formation.
- Finally, for each rock type, the percentage values described in the above two steps were multiplied together to give an overall percentage of each lithology in the 3D map unit. Figure 16 shows histograms for the percentage of different rock types in each of the 3D map units analysed in this way.

The above steps were repeated 5000 times for each 3D map unit to give a representative population of possible compositions.

INTEGRATION OF THERMAL CONDUCTIVITY VALUES AND LITHOLOGY PROPORTIONS

The thermal conductivity values for each rock type and the compositional data for each 3D map unit were then combined using the following process. Firstly, a compositional dataset was randomly selected for the map unit, which contained one possible set of rock type proportions for that unit. Secondly, a set of thermal conductivity values were selected that contained possible thermal

conductivity values for each rock type represented in the map unit. Finally, these two datasets were combined by using them to calculate a weighted harmonic mean thermal conductivity. This process was repeated for all thermal conductivity values and percentage values in the population. The result is a population of 5000 possible thermal conductivity values for the 3D map unit, from which a mean and standard deviation value can be derived (Figure 17).

Table 6: Data sources for stratigraphic information for stratigraphic units in the Cooper and Eromanga basins.

FORMATION	3D MAP UNIT	STRATIGRAPHY DATA SOURCE
Winton Formation	Surficial	Draper (2002)
Mackunda Formation	Surficial	Draper (2002)
Allaru Mudstone	Allaru	Draper (2002)
Toolebuc Formation	Allaru	Draper (2002)
Wallumbilla Formation	Allaru	Draper (2002)
Cadna-owie Formation	Cadna-owie	Draper (2002)
Murta Formation	Cadna-owie	Draper (2002)
Namur Sandstone	Cadna-owie	Draper (2002)
Westbourne Formation	Westbourne	Draper (2002)
Adori Sandstone	Westbourne	Draper (2002)
Birkhead Formation	Westbourne	Draper (2002)
Hutton Sandstone	Westbourne	Draper (2002)
Poolowanna Formation	Westbourne	Moore (1986)
Cuddapan Formation	Westbourne	Draper (2002)
Nappamerri Group	Nappamerri	PIRSA (2008)
Toolachee Formation	Toolachee	PIRSA (2008)
Daralingie Formation	Toolachee	PIRSA (2008)
Roseneath Shale	Toolachee	Draper (2002)
Epsilon Formation	Toolachee	PIRSA (2008)
Murteree Shale	Toolachee	Draper (2002)
Patchawarra Formation	Patchawarra	PIRSA (2008)
Tirrawarra Sandstone	Tirrawarra	Draper (2002)
Merrimelia Formation	Tirrawarra	Draper (2002)
Warrabin Trough units	Warrabin	McKillop et al (2005)

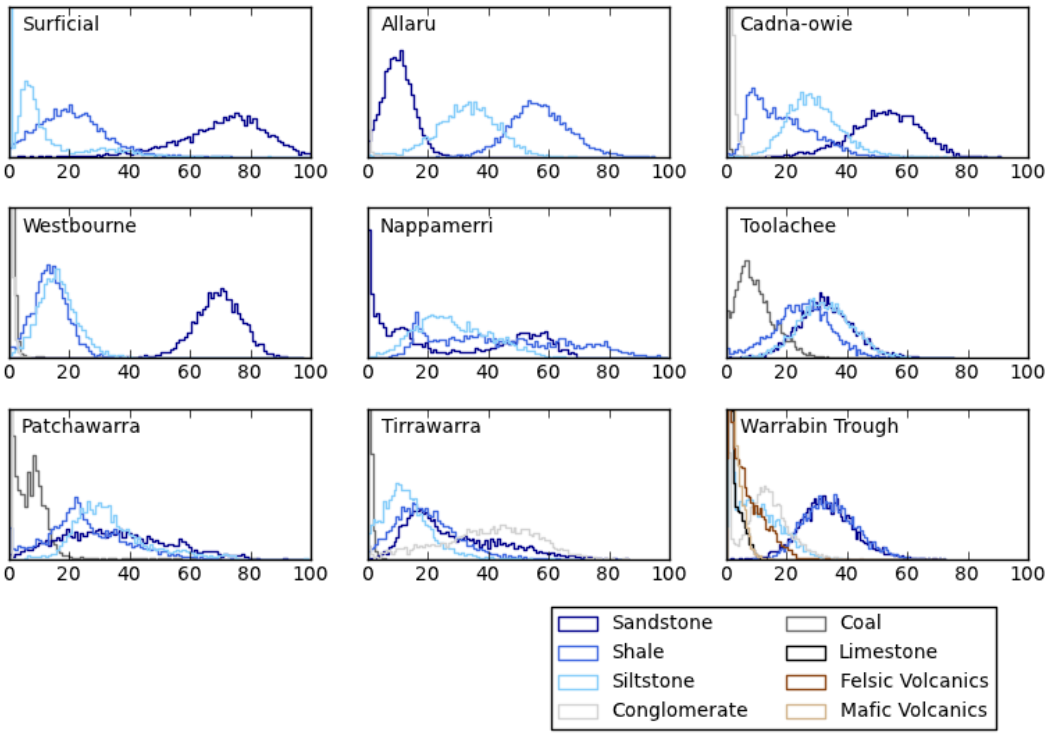

Figure 16: *Normalised probability distributions showing proportions of the main rock types present in basin units in the Cooper Basin region. X axis is in percent. Y scale is the same for all graphs (range = 0 to 0.12) and shows the probability density for each rock type percentage bin.*

THERMAL CONDUCTIVITY CALCULATION FOR GRANITE AND BASEMENT

The thermal conductivities of basement and granite units were calculated using a different process. This difference is because granite is a single rock type and, therefore, it was not necessary to calculate a weighted mean based on different lithological compositions. A mean value and standard deviation was taken from the GA database (Weber and Kirkby, 2011) which contains 104 measurements on Australian granite. The composition of basement is variable and poorly constrained, comprising highly metamorphosed Proterozoic metasediments, Thompson fold belt units and low grade metamorphosed Warburton Basin units. We suggest that a metasedimentary lithology best describes the basement composition, and as such, a mean and standard deviation value was taken from all metasedimentary rocks in the GA database. See Table 7 for the thermal conductivity values and the standard deviations used for each unit.

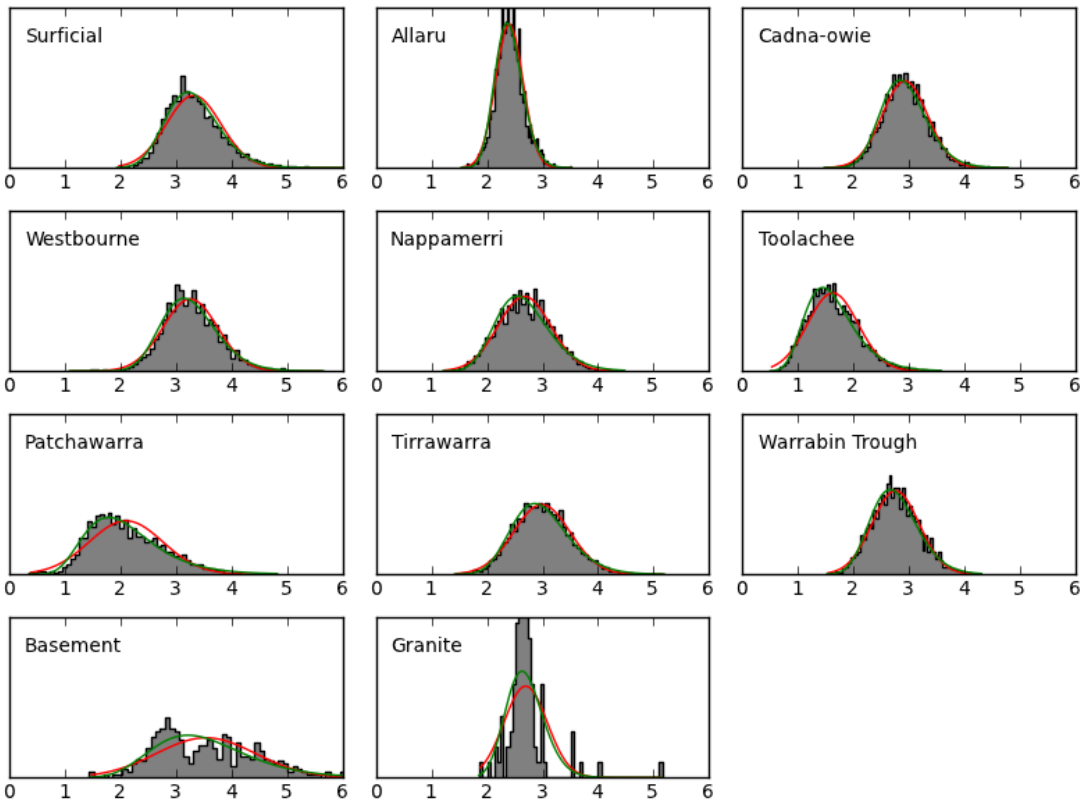

Figure 17: *Thermal conductivity probability distributions for all 3D map units. Y scale is the same for all graphs (range = 0 to 1.8) and shows the probability density for each thermal conductivity bin. Horizontal axis is thermal conductivity in W/mK. Red line shows a normal distribution based on the mean and standard deviation of the population; green line shows a lognormal distribution. The distributions for units Surficial – Warrabin (n = 5000) were obtained using the method described in the text. The distributions for basement and granite (n = 383 and 104 respectively) were taken directly from the Geoscience Australia database.*

Table 7: Thermal conductivity averages and standard deviations used in modelling.

3D MAP UNIT	MEAN THERMAL CONDUCTIVITY (W/mK)	STANDARD DEVIATION (W/mK)
Surficial	3.31	0.51
Allaru	2.40	0.25
Cadna-owie	2.94	0.42
Westbourne	2.92	0.45
Hutton	4.10	0.65
Nappamerri	2.67	0.48
Toolachee	1.63	0.46
Patchawarra	2.10	0.66
Tirrawarra	2.99	0.51
Warrabin Trough	2.73	0.41
Basement	3.54	0.89
Granite	2.79	0.38

Heat production data

BASIN HEAT PRODUCTION

For the Eromanga and Cooper basins, heat production values of 1.2 and 1.4 μW/m^3 respectively were used. Both values were calculated by Meixner et al. (2011) using corrected and weighted potassium, thorium and uranium concentrations from the Australia-wide, levelled and back-calibrated gamma-ray dataset (Minty et al., 2010). For the Eromanga Basin, the value of 1.2 μW/m^3 was calculated based on the intersection of the gamma-ray dataset and outcropping Eromanga Basin units. For the Cooper Basin, there were no outcropping units and therefore an average was taken from all basins assessed in Meixner et al. (2011). These values fall within a 0.9 – 1.5 μW/m^3 range for heat production given by Gallagher (1987b) for the Cooper and Eromanga basins.

BASEMENT AND GRANITE HEAT PRODUCTION

Basement and granite heat production values were calculated using measured uranium, potassium and thorium concentrations from rocks within and beyond the study area, depending on the available data. The following equation was used to calculate heat production:

$$HP = 2670 \times ((K_2O \times 2.91 \times 10^{-5}) + (U \times 9.67 \times 10^{-5}) + (Th \times 2.63 \times 10^{-5})) \quad (1)$$

where HP is heat production in μW/m^3, K_2O is potassium oxide concentration in weight percent and U and Th are uranium and thorium concentrations in ppm (Beardsmore and Cull, 2011; Jessop, 1990; Emsley, 1989).

An estimate of the basement heat production of 1.7 μW/m^3 was used and is based on using global average uranium, thorium and potassium concentrations for upper crustal rocks (Rudnick and Gao, 2003). For the BLS granodiorite an average value of 8.7 μW/m^3 was calculated from values of 7.2 and 10.1 μW/m^3 given by Middleton (1979); these values were calculated from measured U, Th and K abundances. For Devonian age granites, GA's OZCHEM database was queried for all Devonian granites in Australia, giving a median calculated heat production value of 1.9 μW/m^3. For all other granites (undivided), a value of 2.5 μW/m^3 was calculated based on a median value for all Australian granites in the OZCHEM database.

Thermal modelling

PREDICTING TEMPERATURE AT DEPTH

To predict temperature at depth the transfer of heat in the crust must be considered. Heat flows in the earth by conduction or advection of fluids (Stüwe, 2007). Heat can be produced in the crust by radiogenic, chemical and mechanical heat sources. Gibson et al. (2008) propose that as the Australian continent is not subject to active tectonism, there is minimal chemical or mechanical heat production and, at depths of interest for geothermal electricity generation, the dominant mode of heat transfer is conduction.

The heat transfer process is described in the following equation (modified after Stüwe, 2007):

$$\frac{dT}{dt} = \kappa\left(\frac{d^2T}{dz^2}\right) + u\left(\frac{dT}{dz}\right) + (A)/(\rho c_p) \quad (2)$$

Where κ = the thermal diffusivity defined as $k/(\rho c_p)$, k = thermal conductivity, ρ = density, c_p = heat capacity, A = the heat production due to radiogenic heat sources and u is the advection rate vector. This equation assumes a constant thermal conductivity.

Gibson et al. (2008) also proposed that, for the Australian crust, it is sufficient to consider only the case of the thermal steady state based on the assumption that the crust has attained thermal equilibrium since the last period of tectonic or magmatic disturbance. Thermal equilibrium, or steady state, is expressed as

$$\frac{dT}{dt} = 0$$

The steady state equation for conductive heat flow can be expressed as:

$$Q_0 = Q_d + \int A(z)\partial z \quad (3)$$

Where Q_0 = surface heat flow, Q_d = heat flow at depth d, $\int A(z)\partial z$ = the integral of volumetric heat production from the surface to d, A = heat production and z = depth.

The heat flow at depth d can be calculated using the following relationship:

$$Q_d = \lambda_d \cdot \left[\frac{\Delta T}{\Delta z}\right]_d \quad (4)$$

Where: λ_d = thermal conductivity at depth d and T = temperature in °C.

From equations (3) and (4), it can be seen that the key datasets for calculating temperature at depth are: heat flow, thermal conductivity, and heat production. The relationship between these variables is diagrammatically illustrated in Figure 18.

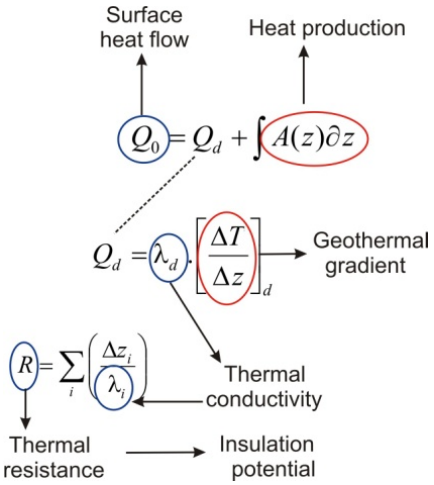

Figure 18: *Relationship between key thermal parameters useful for geothermal resource exploration.*

The transfer of heat by the advection of fluids, in particular convection of water in permeable aquifers, has not been considered. Although convection may occur within high permeability sandstones of the Eromanga Basin (part of the Great Artesian Basin; Habermehl, 2001), the effect on heat transfer and hence, computed temperatures, is likely to be localised.

3D THERMAL MODELLING USING SHEMAT

3D temperature prediction was achieved by performing thermal modelling on the 3D geological map using the SHEMAT software package (Clauser, 2003). SHEMAT uses a finite difference method to solve coupled problems involving fluid flow, heat transfer, species transport, and chemical water-rock interaction in fluid-saturated porous media. For this study, only conductive heat transport was modelled. The solver can be set to calculate using an implicit method (unconditionally stable), an explicit method (faster), or a combination of the two. For this study a fully implicit solution was used.

Thermal conductivity is not a constant for geologic materials; it varies with temperature (e.g., Birch and Clark, 1940). The temperature dependence of thermal conductivity is incorporated into SHEMAT using the following equations from Zoth and Hänel (1988):

$$\lambda_r(T > 400°C) = \frac{770}{350 + T} + 0.7$$

$$\lambda_r(T < 400°C) = \lambda_r(T > 400°C) \times \left[\frac{\lambda_r(20°C)}{\frac{770}{350 + 20°C} + 0.7} - \left(\frac{\lambda_r(20°C)}{\frac{770}{350 + 20°C} + 0.7} - 1 \right) \left(\frac{T - 20°C}{400 - 20°C} \right) \right] \quad (5)$$

During this study, boundary conditions were applied to the derived equation for 3D temperature prediction as follows:

- for the four vertical sides, "no flow" boundary conditions where all lithologies and temperatures are mirrored beyond the model boundaries, and therefore no heat flows in or out of the model;
- for the bottom boundary, a constant predefined heat flow; and
- for the top boundary, a uniform constant temperature.

For this study, the top temperature boundary condition was set in the top layer of cells of the model. To incorporate the effects of topography, a region was added at the top of the model to represent the volume above the topographic surface (atmosphere). In this region the thermal conductivity was set to a very high value (80 W/mK) and heat production set to zero so that the temperature at the topographic surface was very close to the assigned top temperature boundary condition.

Each SHEMAT input file contains a list of arrays and scalars representing the input parameters for simulation. The output files have an identical format but contain the final values of the simulated parameters. In order to convert the models from Gocad voxet format into SHEMAT input files, and then back into Gocad format after simulation, the open source Python scripting library PySHEMAT (Wellmann et al., 2012) was utilised in conjunction with separate scripting libraries developed by the authors. The properties exported for interrogation in Gocad are summarised in Table 8.

Table 8: Summary of thermal property outputs solved in 3D by SHEMAT.

3D TEMPERATURE AND OTHER OUTPUTS FROM SHEMAT	
Temperature	(°C) – Solved for every cell/voxel centre by finite difference method.
Vertical Heat Flow	(mW/m^2) – Flow of heat measured in energy per time per unit area. For each cell/voxel centre, the value returned is an arithmetic average of the heat flow calculated with respect to the centre of the cell immediately above and the cell immediately below.
Thermal Conductivity (final)	(W/mK) – Calculated for each cell. Represents the thermal conductivity at the modelled temperature for the cell.

MODEL BOUNDARY CONDITIONS

Top boundary condition

The cells in the 3D mesh that coincide with the topographic surface were assigned a constant temperature of 25 °C. This value was calculated based on the mean annual surface temperature of 22 °C from the Bureau of Meteorology[4] at the location of 142 ° east and 27 ° south. The 25 °C value assigned equates to the average soil temperature, which is generally about 3 °C higher than the average air temperature (Howard and Sass, 1964).

Basal heat flow

The calculated heat flow at the topographic surface of the thermal model corresponds to the sum of the heat-flow at the base of the model and the heat flow contribution of heat production within the model. If the surface heat flow is constrained and the geometry and heat production value of the heat

[4] http://www.bom.gov.au/

producing bodies are also constrained, then the heat flow at the base of the model may be determined. Unfortunately these constraints are not well known. The only heat flow measurements in the study area are from the Beardsmore (2004) study, which produced measured values of 100 mW/m^2. This value, although high compared to global average values of 49 – 54 mW/m^2 (Chapman and Furlong, 1977; Morgan, 1984), is not unexpected as the wells analysed are located over the high-heat-producing BLS granodiorite.

One method of estimating the basal heat flow into the model is to sum the expected heat flow from the mantle with the heat flow contribution of heat production from the base of the crust to the base of the model. Neumann et al. (2000) and McLaren et al. (2003) calculated a reduced heat flow, or the heat flow at the mantle/crust boundary from geochemical and heat flow data using the method of Lachenbruch (1968) and Birch et al. (1968). The values, 29.5 mW/m^2 and 25 mW/m^2 respectively, were both calculated for a region in South Australia which Neumann et al. (2000) called the South Australian Heat Flow Anomaly. This anomaly forms part of the Central Australian Heat Flow Province of McLaren et al. (2003) and comprises a region of the Australian continent that formed mostly during the Proterozoic. Assuming that more recent interpretations of the Tasman Line are correct (Direen and Crawford, 2003), then the Central Australian Heat Flow Province (Figure 1 of McLaren et al. 2003) extends into the western portion of the study area. No equivalent study has been conducted that could be used to determine the reduced heat flow for the eastern portion of the study area. Neumann et al. (2000), however, concluded that the elevated heat flow in the South Australian Heat Flow Anomaly was the result of enrichment of the upper crust in uranium, thorium and potassium within granitic and volcanic lithologies, and was not the result of abnormal mantle heat flow. As no estimation for the reduced heat flow exists for the eastern portion of the study area, and the available value for western portion is not abnormal, then it is likely that an average of the Neumann et al. (2000) and McLaren et al. (2003) reduced heat flow value (27 mW/m^2) is the best available estimation of the actual value.

The heat flow contribution due to heat production in the mid to lower crust is calculated by integrating the heat production of these lithologies with depth. Rudnick and Gao (2003) give heat production estimates of 1.0 $\mu W/m^3$ for mid crustal lithologies (13 to 23 km depth) and 0.19 $\mu W/m^3$ for lower crustal lithologies (from 23 km depth to the Moho). The Moho depth in the region is approximately 35 km (Kennett et al., 2011). Based on these heat production values and depth extents, the heat flow contribution from the Moho to the base of the model (10 km depth) is 12 mW/m^2.

Combining the heat flow contribution due to the heat produced between the base of the model and the base of the crust (12 mW/m^2) and the reduced heat flow at the base of the crust (27 mW/m^2), we calculated an initial basal heat flow value for our thermal models of the Cooper Basin of 39 mW/m^2.

THERMAL MODELLING WORKFLOW

The thermal modelling was performed in three stages using the SHEMAT software with the temperature-dependent thermal conductivity option. The modelling was run at the NCI high performance computing centre. Stage one, the initial thermal model, involved forward modelling using the thermal properties and the boundary conditions described in the above sections. This thermal model produced predicted temperatures and surface heat flows significantly lower than the measured values. The second stage of the thermal modelling process involved a sensitivity analysis of the predicted heat flow and temperature due to variations in the input thermal properties. This sensitivity analysis aided in the third stage of the thermal modelling, which involved running a series

of iterations where the thermal properties were optimised, and the 3D map altered in order to minimise the temperature and heat flow residuals. The temperature and heat flow residuals are the difference between the available downhole temperature measurements and calculated heat flow determinations described above and predicted temperatures and heat flows for the corresponding locations. This iterative third stage of modelling led to the optimised final thermal model.

THE INITIAL THERMAL MODEL

The initial thermal model was computed on the voxelised 3D map using the input properties listed in Table 9 and with the boundary conditions discussed above (surface temperature of 25 °C; basal heat flow of 39 mW/m^2 at 13 km, the depth extent of the model). The results of the initial thermal model are shown as a temperature slice at 4 km below ground level (Figure 19). The effect of the high heat producing BLS is evident by the coinciding higher predicted temperatures (up to 169 °C, compared to an average of 112 °C for the initial model) at 4 km depth. The effect of the higher heat production of the undivided granites with respect to the basement is also evident by the temperature anomalies coinciding with the interpreted granite bodies. The effect of the comparatively low thermal conductivity of the sediments is also evident in the subtle temperature anomaly trending from the southwest to the northeast corresponding to the general northeast-trending Cooper Basin depocentre (figures 2 and 5). Higher temperature anomalies correspond to the thick sediments of the Patchawarra Trough in the southwest and the Warrabin Trough in the northeast.

The median temperature residual for this model is 46.2 °C, which is large considering the median measured temperature is 124.8 °C. The median heat flow residual was 30.2 mW/m^2, which is also large compared to the median heat flow determination of 101.4 mW/m^2. This indicates that the model is considerably under-predicting both the temperature and the heat flow.

Table 9: Thermal properties used in initial and final thermal models, together with the mean and standard deviation values used for 3D map units in the stochastic modelling.

	HEAT PRODUCTION, μW/m^3				THERMAL CONDUCTIVITY, W/mK			
3D MAP UNIT	**INITIAL**	**FINAL**	**MEAN**	**SD**	**INITIAL**	**FINAL**	**MEAN**	**SD**
Surficial	1.4	1.4			3.31	2.81	3.31	0.51
Allaru	1.4	1.4			2.40	2.04	2.40	0.25
Cadna-owie	1.4	1.4			2.94	2.50	2.94	0.42
Westbourne	1.4	1.4			2.92	2.48	3.23	0.45
Nappamerri	1.2	1.2			2.67	3.49	2.67	0.48
Toolachee	1.2	1.2			1.63	2.27	1.63	0.46
Patchawarra	1.2	1.2			2.10	1.39	2.10	0.66
Tirrawarra	1.2	1.2			2.99	1.79	2.99	0.51
Warrabin Trough	1.2	1.2			2.73	2.54	2.73	0.41
Basement	1.7	3.8	3.5	1.8**	3.54	3.54	3.54	
Undivided granites	2.5	3.8	3.2	2.7	2.8	2.80	2.80	
Big Lake Suite granodiorite	8.7	8.7	8.7	2.0	2.8	2.80	2.80	
Devonian granites	1.9	3.8	2.2	1.5	2.8	2.80	2.80	
BasementNW*	1.7	5.3	5.0	1.8**	3.54	3.54	3.54	
BasmentSE*	1.7	4.6	4.3	1.8**	3.54	3.54	3.54	
	BASAL HEAT FLUX, mW/m^2							
N/A	39	48	55	16				

*3D map units added to match temperature measurements during iterative stage of the thermal modelling

**Estimated standard deviation as described in text

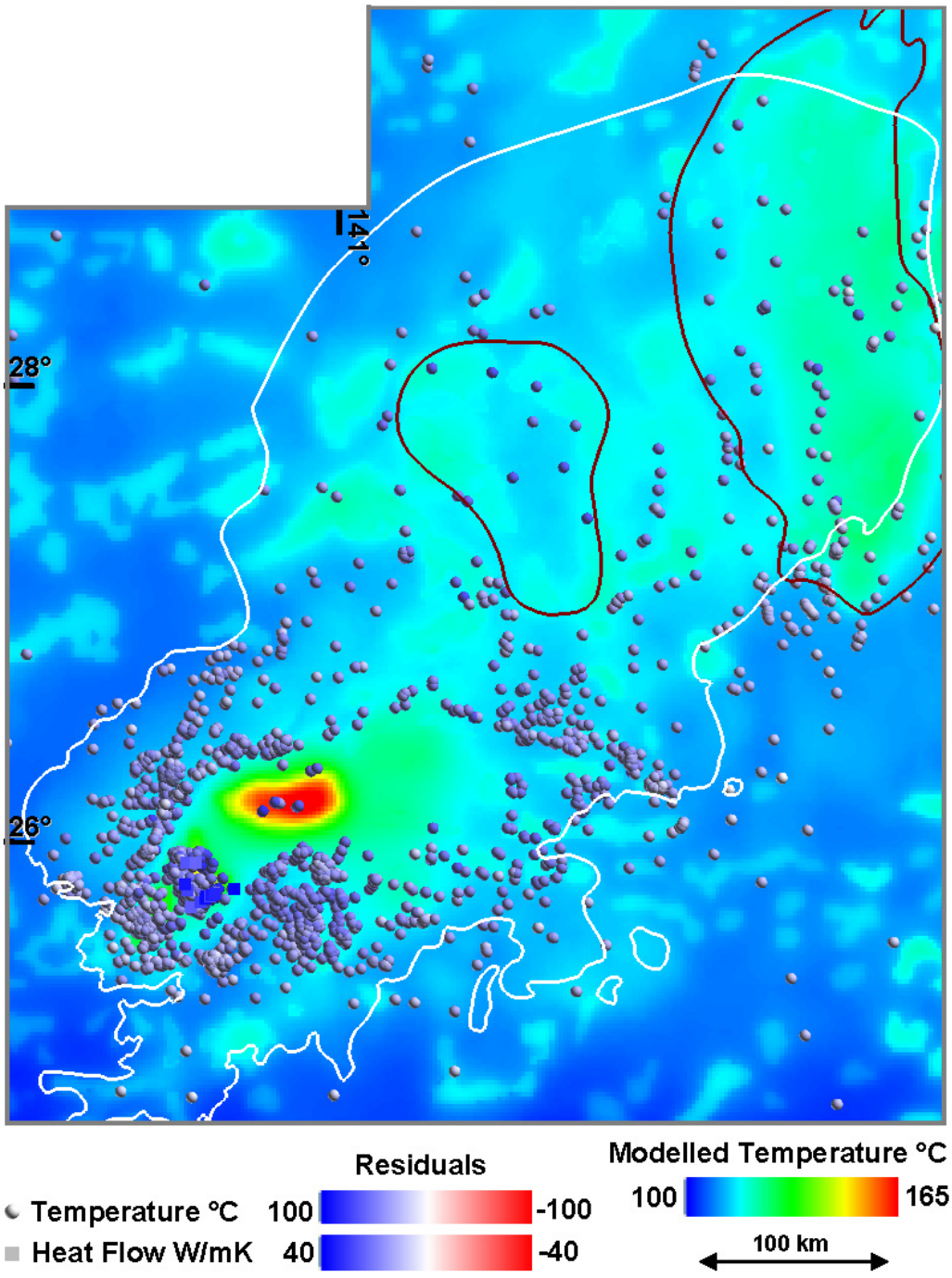

Figure 19: *A 4 km depth slice through the initial thermal model showing the modelled temperature. Coloured symbols show the calculated residuals at control points; temperature residuals are represented as circles and heat flow residuals as squares. The blue colours of the residual temperatures indicate that the thermal model is not 'hot' enough to match the measured temperatures and heat flows. Outline of the Cooper Basin shown in white; outline of the Warrabin Trough and the Barrolka Gravity Low are shown in maroon*

THERMAL PROPERTY SENSITIVITY MODELLING

The large positive values for the temperature and heat flow residuals from the initial thermal model indicate that this thermal model is not 'hot' enough. To provide an indication of which property or properties require adjustment and to what degree, a series of thermal models were run to test the sensitivity of the predicted temperature and heat flow to these property adjustments. The properties subjected to sensitivity analysis, listed below, were the properties that were considered to have the largest influence on the predicted temperatures and heat flows, and hence, the largest influence on the residual temperatures and heat flows. For each property analysed, four thermal models were run that successively increased or decreased the property value so that the sensitivity of the modified property could be compared with the results for the initial property value. The property values were only modified in the direction that would increase the 'heat' in the model. The model properties analysed were:

- Basal heat flow: Increasing this value will result in a mostly uniform increase of temperatures at depth and heat flows at the surface.
- Heat production of the basement: The larger the depth extent and volume of the basement unit for which heat production is increased, the larger the increase in temperatures at depth and heat flows at the surface.
- Heat production of the granites: as above.
- Thermal conductivity of the sediments: Adjusting this parameter will only have a minor influence on the surface heat flow which will be the result of increased refraction of heat around areas of thick sediment cover resulting from the lower thermal conductivities. The modification of this property, however, will have a major impact on the predicted temperatures in the model region directly within or beneath the modified unit.
- Heat production of the sediments: This is not expected to have as large an effect on predicted temperature and heat flow as increasing the heat production of the basement, due to the lesser volume of sediments in the model compared to the basement. However, to ascertain what the effect is, sensitivity analysis was carried out.

The thermal properties that were not subjected to this sensitivity analysis were the following:

- Top boundary condition, or temperature at the top of the model: Modifications to this temperature by a given value will result in a blanket change in the predicted temperatures throughout the model by that same value. The value (25 °C) is reasonably well constrained and is expected to be accurate to within a few degrees.
- Thermal conductivity of the basement: Varying the thermal conductivity of a specific region in a model will have little effect to predicted temperatures above that region. As most of the downhole temperature measurements were made at or near the base of the sedimentary section, increasing the thermal conductivity of the basement will have little effect to the temperature residuals.
- Thermal conductivity of the granites: as above.

The results of the sensitivity analysis are shown in Figure 20 and Table 10. The plot of temperature residuals (Figure 20B) shows strong model sensitivity to basal heat flow, basement heat production and sediment thermal conductivity. The plot also suggests that the model is relatively insensitive to changing heat production in the granites and basin sediments. Similar relationships are observed in the plot of heat flow residuals (Figure 20A), with the exception of apparent model insensitivity to the thermal conductivity of the sediments.

The observed sensitivities can largely be explained in relation to the location of downhole measurement points. The measurement points are predominantly located near the basin-bedrock

contact, with few points located directly above granites. As a consequence, regional sources of heat (i.e., basal heat flow and basement heat production) should have the greatest effect on model residuals as observed in the results. Localised (granite) and shallow (basin sediment) heat production have a much smaller apparent affect. The thermal conductivity of the overlying basin sediments has a significant role in trapping heat near the basin-bedrock contact, thereby increasing the observed temperatures, but does not affect the heat flow below the basin (Figure 20A).

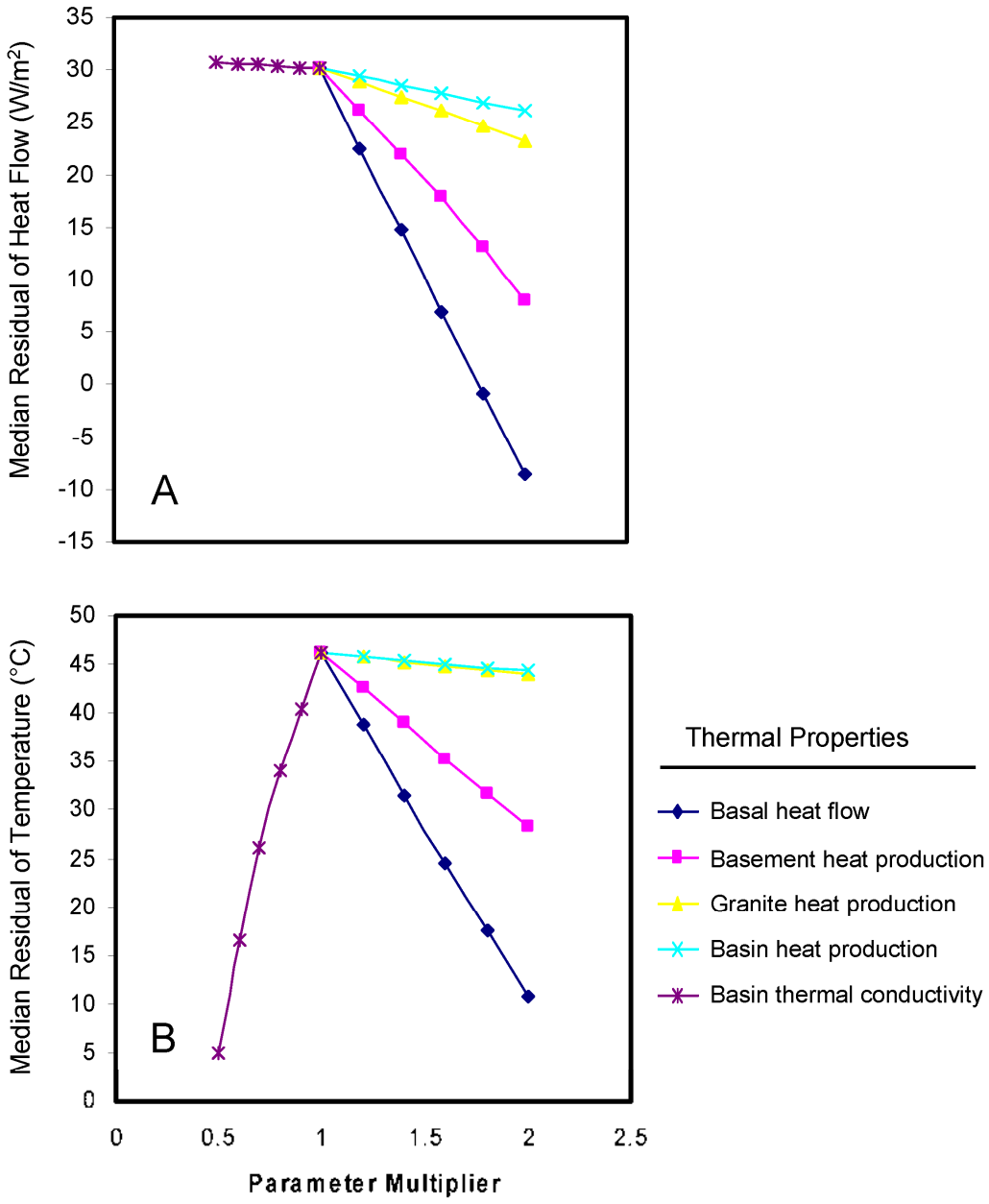

***Figure 20**: Graphs showing the sensitivity of calculated heat flow and temperature due to varying thermal property values. Properties showing significant changes in mean residual value (A. Heat flow residual; B. Temperature residual) with changing parameter multiplier are sensitive (e.g., basal heat flow), properties showing minimal change are insensitive (e.g., basin heat production).*

Table 10: Thermal properties sensitivity analysis.

MULT.[a]	MEDIAN TEMP. (°C)	MEDIAN TEMP. RESIDUAL (°C)	MEDIAN HEAT FLOW (mW/m^2)	MEDIAN HEAT FLOW RESIDUAL (mW/m^2)	MEDIAN HEAT FLOW SLICE[b] (mW/m^2)
Control Values	**med 125.0[c] stdev 24.0**		**med 101.4[d] stdev 5.8**		
Initial Model Values	**78.9**	**46.2**	**66.8**	**30.2**	**61.8**
Basal Heat Flow (mW/m^2)					
1	78.9	46.2	66.8	30.2	61.8
1.2	86.0	38.9	74.6	22.5	69.6
1.4	93.3	31.5	82.5	14.7	77.6
1.6	100.9	24.5	90.2	6.9	85.4
1.8	108.4	17.5	98.1	-0.8	93.3
2.0	116.5	10.7	105.9	-8.5	101.2
Basement Heat Production					
1	78.9	46.2	66.8	30.2	61.8
1.2	82.3	42.7	71.6	26.1	65.7
1.4	86.0	39.0	76.4	22.0	69.6
1.6	89.6	35.2	81.1	17.9	73.6
1.8	93.2	31.7	85.8	13.2	77.6
2.0	96.8	28.2	90.5	8.0	81.6
All Granite Heat Production					
1	78.9	46.2	66.8	30.2	61.8
1.2	79.1	45.8	68.3	28.9	62
1.4	79.3	45.3	69.8	27.5	62.1
1.6	79.5	44.9	71.3	26.1	62.3
1.8	79.7	44.5	72.8	24.7	62.4
2.0	79.9	44.0	74.2	23.3	62.6
All Basin Sediments Thermal Conductivity					
1	78.9	46.2	66.8	30.2	61.8
0.9	84.4	40.5	66.6	30.3	61.8
0.8	91.2	34.0	66.4	30.4	61.8
0.7	99.2	26.0	66.2	30.5	61.8
0.6	109.1	16.5	66	30.6	61.8
0.5	121.6	4.9	65.8	30.8	61.7
All Basin Sediments Heat Production					
1	78.9	46.2	66.8	30.2	61.8
1.2	79.2	45.8	67.6	29.4	62.4
1.4	79.5	45.5	68.4	28.6	62.9
1.6	79.9	45.1	69.2	27.8	63.5
1.8	80.2	44.7	70.1	27.0	67.0
2.0	80.5	44.4	70.9	26.2	64.6

[a] Multiplier (MULT.)- the value that the initial model property value was multiplied by during sensitivity analysis. During evaluation of granite and sediment properties, all lithologic units were multiplied by the same amount, regardless of position or initial value.

[b] The median heat flow slice refers to the median value for the computed heat flow at the surface of the model.

[c] The median and standard deviation for temperature control values correspond to downhole measurements collected in the Cooper Basin model area.
[d] The median and standard deviation for heat flow control values are taken from the group of 13 measurements performed by Beardsmore (2004) in the Geodynamics Limited geothermal exploration lease GEL99. These measurements were collected from wells located above the BLS granodiorite.

As discussed above, the granites are localized and poorly covered by existing borehole measurements. Therefore the sensitivity of the temperature residuals to granite heat production is under-represented and the observed effect small. Although this has the benefit of eliminating the granites as a significant cause of residuals, it also indicates that the field measurements are inadequate to constrain granite heat production rates.

Based on the thermal property sensitivity analysis it is unlikely that individual parameters can account for the observed residuals. Individually, basal heat flow and basement heat production need to be increased by more than a factor of two to achieve a satisfactory fit to the measured temperatures and heat flow. Likewise, the thermal conductivities of the sediments need to be reduced by half to match the temperature measurements, and would not account for the observed heat flow residuals. Basal heat flow is poorly constrained in the Cooper Basin, however values greater than double those used initially are considered unrealistic for the Australian craton. Basement heat production is also poorly constrained, and values of double those used initially may be reasonable for the Australian craton. Final values for this parameter were selected on the basis of measurements from nearby regions, as discussed below. Constraints on basin thermal conductivities are imperfect, but as discussed above, available borehole lithologies and core samples provide a reasonable characterisation of the sediments and proscribe a major revision of the thermal conductivities. Therefore, the sensitivity analysis indicates that it is necessary to modify a combination of the thermal properties.

ITERATIVE THERMAL MODELLING

To minimise the temperature and heat flow residuals a series of iterations was carried out where the thermal properties were modified in order to minimise the temperature and heat flow residuals. Where residuals were high, the thermal properties in that region of the model were adjusted and the thermal model was re-run. The initial iterations were aimed at minimising the heat flow residuals, by modifying the basal heat flow, the basement heat production and the heat production of the BLS. Once this was achieved, the temperature residuals were minimised by altering the thermal conductivities of the basin sediments. The final series of iterations involved the modification of the 3D map to allow incorporation of different basement heat producing regions.

The results of the sensitivity analyses were used as an aid to guide which property and the degree of modification required to minimise the residuals. The sensitivity analyses also provided realistic bounds for properties. For example, the sensitivity analysis has shown that the basal heat flow has a major impact on the temperature and heat flow residuals (Figure 20) and was therefore an obvious property to alter in order to reduce the temperature and heat flow residuals. It can be seen that by increasing the heat flow alone, it would be possible to match the median temperature residuals. The value required to achieve this (~90 mW/m^2), however, is unrealistically high and would result in a unrealistically high median heat flow at the surface (~112 mW/m^2) when compared to average global surface heat flow values of 49 – 54 mW/m^2 (Chapman and Furlong, 1977; Morgan, 1984), or even heat flow values for the Central Australian Heat Flow Province (~ 80 mW/m^2; McLaren et al.,

2003). Also, applying a basal heat flow of this magnitude would produce a large negative heat flow residual (-18 mW/m^2) indicating that the heat flow in this region of the model is too high.
As well as the basal heat flow, the heat production of the basement was also increased. In the initial thermal model, 1.7 μW/m^3 was used as a basement heat production value. This value was increased to 3.8 μW/m^3. Changing the heat production of basement is justified given that the value of 1.7 μW/m^3 is based on an average upper crustal composition, and is not based on data specific to this region. Previous studies (e.g., Meixner et al., in prep; Meixner et al., 2011) suggest the basement heat production is considerably higher than 1.7 μW/m^3, based on both thermal modelling, and heat production values calculated from the national gamma-ray dataset of Minty et al. (2010) for outcropping Proterozoic units (Meixner et al., in prep). Although increasing the basal heat flow and heat production of the basement has increased the amount of heat in the model, allowing the matching of the heat flow at the surface in the vicinity of the heat flow measurements, the temperature residuals were still high on average. In order to reduce these temperature residuals, the thermal conductivities of the sedimentary basin sediments were reduced by multiplying the thermal conductivities of all the basin units by a multiplier (0.85).

Figure 21 shows an interim thermal model where median heat flow residuals have been minimised and median temperature residuals have been considerably reduced. There are, however, two regions, in the northwest and the southeast where temperature residuals are positive and, hence, the predicted temperatures are not high enough. In the sensitivity analysis, further increasing the heat production of the basement produced the desired effect of minimising the temperature residuals in these regions. To allow for the addition of differing basement heat producing regions, the 3D map was modified and the basement divided into the three regions. The location of the boundaries between the different regions is based on the following: for the region in the northwest, the boundary follows a northeast-trending break in the gravity. To the west of this break, the anomalies generally track east to northeast, to the east of the break they generally track northwest. For this region, a heat production value of 5.3 μW/m^3 was assigned resulting in a marked reduction of the temperature residuals. This heat production value was assigned based on heat production values calculated by Neumann et al. (2000) who measured the uranium, thorium and potassium concentrations of basement rocks in the Gawler-Curnamona region and derived heat production values. From these heat production values, we have calculated a median value for non-granite units of 5.3 μW/m^3. For the region in the southeast, the division follows the outline of the Bourke geophysical region (Figure 3) from the crustal elements map (Shaw et al., 1996). In this region a heat production value of 4.6 μW/m^3 was required to minimise the temperature residuals.

Despite the fact that the basement heat production was increased considerably, it was still necessary to increase the basal heat flux above the initial value of 39 mW/m^2. A value of 48 mW/m^2 was found to minimise the temperature and heat flow residuals, therefore this value was used in the final thermal model.

THE FINAL THERMAL MODEL

The final thermal model is shown in Figure 22 and the corresponding thermal properties are listed in Table 9. The median heat flow residual is -1.2 mW/m^2 and the median temperature residual is 2.2 °C. The effect of increasing the heat production in the added basement region in the northwest is evident by the increase in predicted temperatures in this region. The effect is less prominent for the region in the southeast. An alternative means of analysing the results of a thermal model is via the visualisation of an isothermal surface. These are of value to the geothermal explorer in predicting the depth to a target temperature, (150 °C in the example given in Figure 23).

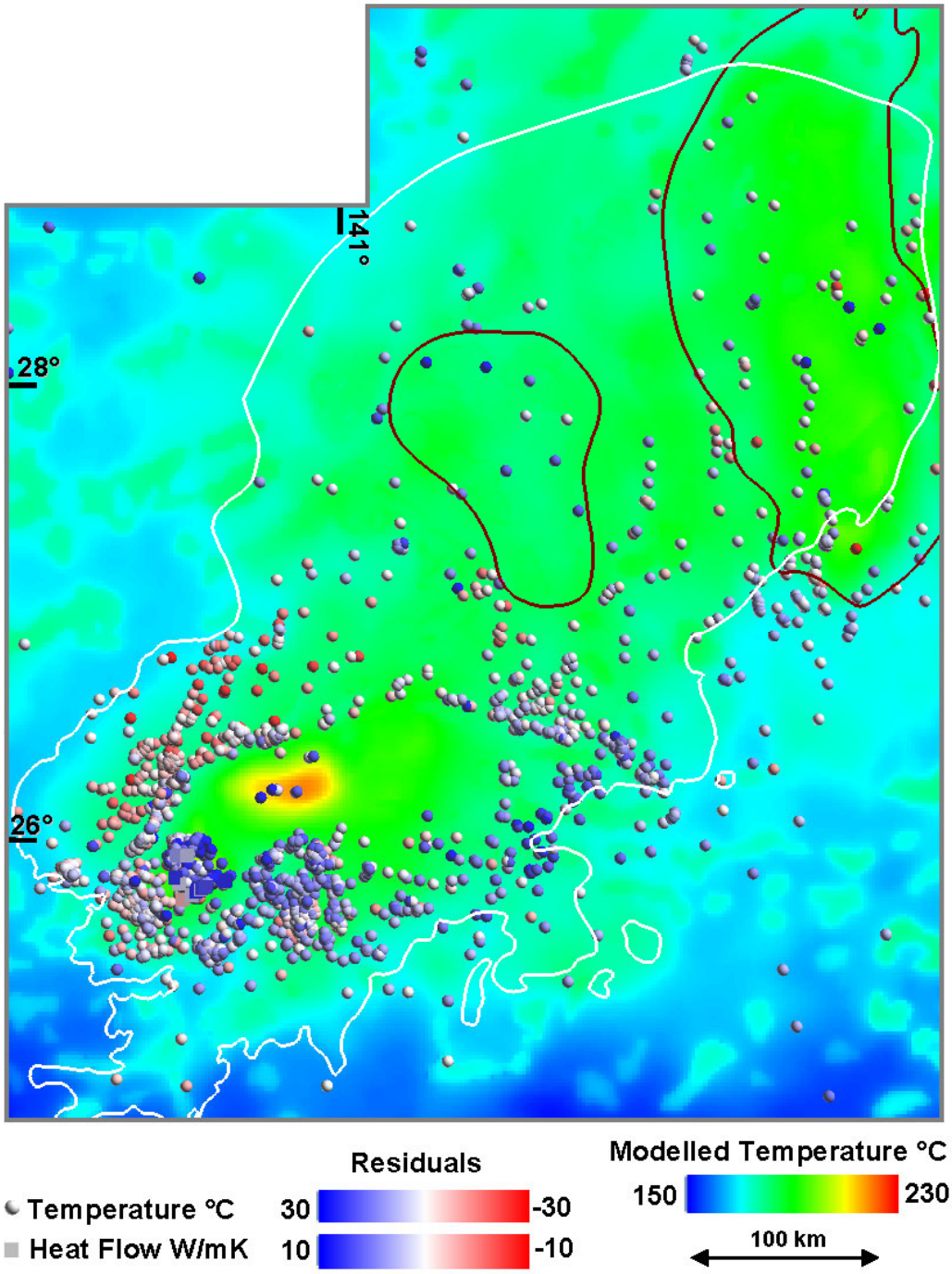

Figure 21: *A 4 km depth slice through an interim thermal model prior to the division of the basement into three regions of differing heat production. Coloured symbols show the calculated residuals at control points; temperature residuals are represented as circles and heat flow residuals as squares. Outline of the Cooper Basin shown in white; outline of the Warrabin Trough and the Barrolka Gravity Low are shown in maroon.*

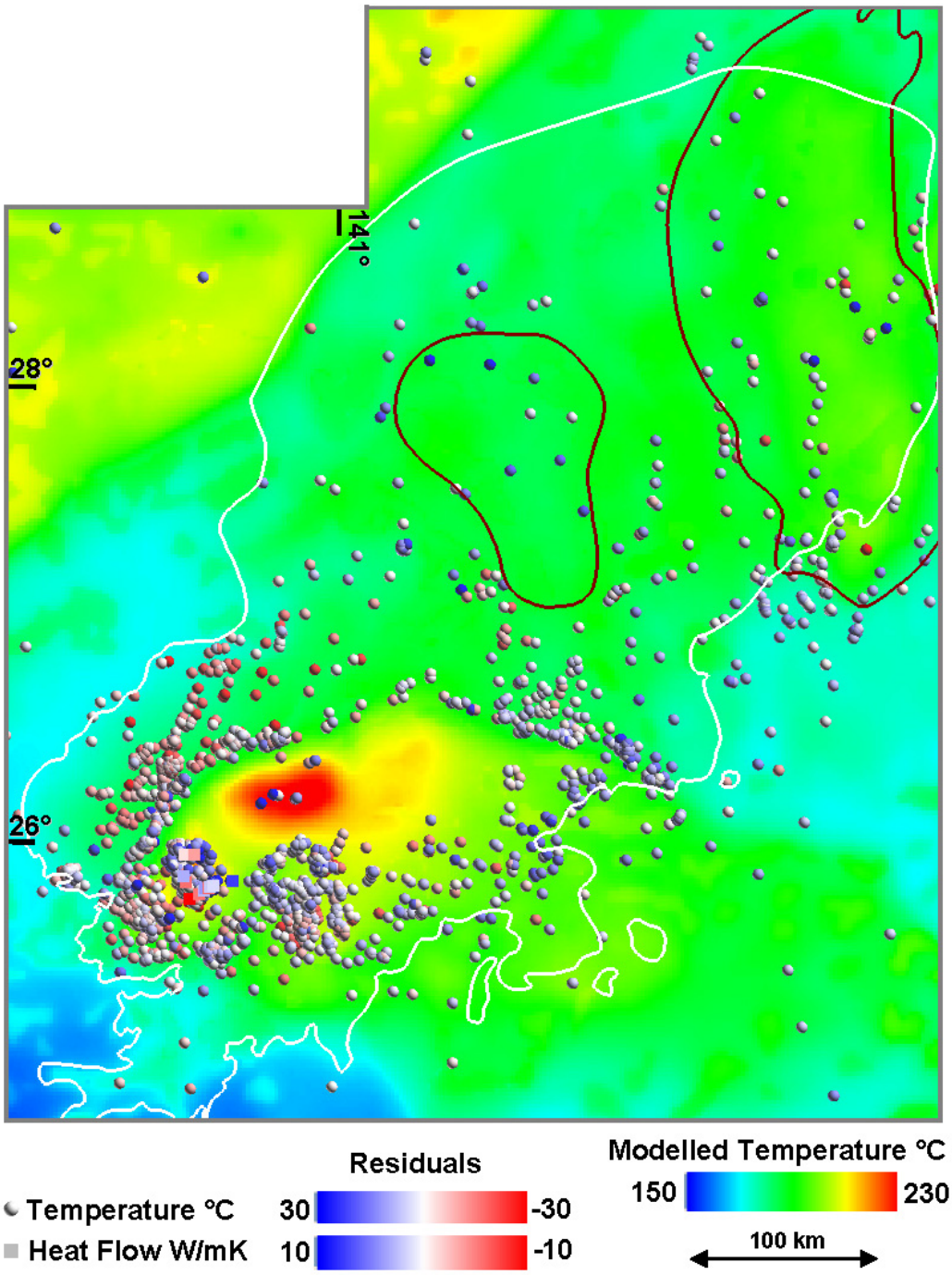

Figure 22: *A 4 km depth slice through the final thermal model. Coloured symbols show the calculated residuals at control points; temperature residuals are represented as circles and heat flow residuals as squares. Outline of the Cooper Basin shown in white; outline of the Warrabin Trough and the Barrolka Gravity Low are shown in maroon.*

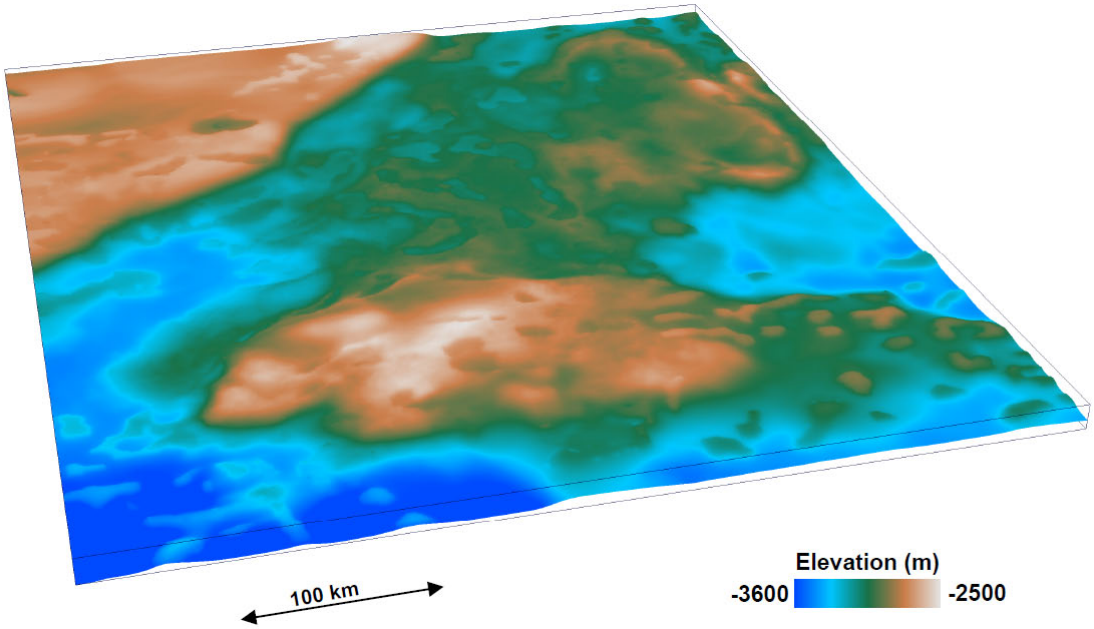

***Figure 23**: Oblique view of a 3D isothermal surface generated from the final thermal model at 150 °C.*

Stochastic thermal modelling

In order to explore the uncertainty of the predicted temperature estimates within the Cooper Basin region, we have used the SHEMAT software combined with the Python scripting library PySHEMAT (Wellmann et al., 2012) and other libraries developed by the authors, to vary the input thermal properties of each lithology (i.e., thermal conductivity, heat production rate) according to their standard deviation. Repeated parameter sweeping of these distributions occurs for each geology unit, allowing multiple models to be generated that represent the variability of the thermal properties set. Additionally, parameter sweeps can include permutations from a normalised distribution for a set boundary condition, for example, variable heat flow to the base of the model. These stochastic models represent a population of viable alternatives reflecting the uncertainty in the input model thermal properties. Multiple thermal simulations are undertaken for each of the generated models. Following forward 3D temperature calculations, the family of voxet-model outcomes (3D results for temperature, heat flow and geothermal gradient) are then interrogated by statistical methods to yield the mean values and standard deviations of the temperature, heat flow and temperature gradient.

Stochastic thermal modelling was conducted on the final thermal model (Figure 22). Normalised property distributions (mean value and first standard deviation) were specified for the thermal properties identified as most sensitive to change in the sensitivity analysis. These properties are the basal heat flow, heat production in the three basement units, the heat production of the BLS, the heat production of the undivided granites, and the thermal conductivity of the Eromanga Basin, Cooper Basin and Warrabin Trough sediments. The mean and standard deviations for the sixteen parameters that were allowed to vary are shown in Table 9. Where the property has been constrained by measurements such as the thermal conductivity of the basin sediments and heat production of the granites, the standard deviation used for the stochastic modelling is the same as the value calculated for the initial model. Where the property was not constrained by measured data (i.e. heat production in the three basement regions and basal heat flux), we have estimated likely upper and lower bounds for the property, and used these to construct a normal distribution on which to base stochastic modelling. We have assumed that the bounds represent likely scenarios, and therefore encompass the range of -1 to +1 standard deviation from the mean. It is noted that the heat production and heat flow used in the final, optimised thermal model are not necessarily the mean values in the distributions described below, but the values we consider most likely, based on the fit with the temperature data and on geological information.

The bounds on the basement heat production and basal heat flux were estimated as follows. For basement heat production, an upper bound of 6.7 $\mu W/m^3$ was estimated. This value is the maximum average value for a non-granitic basement unit (Petermorra Volcanics) as calculated by Neumann et al. (2000). The lower bound of 1.7 $\mu W/m^3$ is the value used in the initial thermal model, based on a global average upper crustal composition (Rudnick and Gao, 2003). We have calculated the upper and lower bounds for each of the basement units based on these values, and the heat production values used in the final thermal model. For example, in the basement region in the northwest, a heat production value of 5.3 $\mu W/m^3$ was used in the final thermal model. This is 1.5 $\mu W/m^3$ more than in the central basement region, which was assigned the lowest basement heat production value in the final model (3.8 $\mu W/m^3$). The upper bound in the region in the northwest was therefore taken to be 6.7 $\mu W/m^3$ (i.e., the upper bound for basement heat production in the entire model). The lower bound for the central region was taken to be 1.7 $\mu W/m^3$ (i.e., the lower bound for basement heat production for the model). To calculate the lower bound on the basement region in the northwest, 1.5 $\mu W/m^3$ was added to the overall lower bound of 1.7 $\mu W/m^3$ giving a value of 3.2 $\mu W/m^3$.

Conversely, to calculate the upper bound for the central basement region, 1.5 $\mu W/m^3$ was subtracted from 6.7 $\mu W/m^3$ to give 5.2 $\mu W/m^3$.

The bounds on the basal heat flux were calculated from the bounds on the basement heat production. In the region in the southwest, if the lower bound basement heat production value of 2.5 $\mu W/m^3$ is taken, in order to match the measured surface heat flow in this region (100 mW/m^2), a basal heat flux of 71 mW/m^2 is required. Conversely, if the upper bound of 6.0 $\mu W/m^3$ is taken, a basal heat flux of 39 mW/m^2 is needed to match the heat flow data. Therefore, lower and upper bounds on the basal heat flux were calculated to be 39 and 71 mW/m^2 respectively.

For each property to be varied, a model sweep is computed based on the mean parameter value plus one standard deviation and another forward model on the mean parameter value minus one standard deviation. If all parameters are varied independently, the total number of sweeps equals two raised to the power of the number of parameters to be varied. For sixteen parameter variations this equates to 2^{16} or 65,536. This large number of model runs is not practical in terms of either computational time or disk storage space. Therefore we have reduced the number of model sweeps by combining some units so that not all parameters are varied independently. The units we have combined are the Eromanga basin units Surficial, Allaru, Cadna-owie and Westbourne; and the Cooper Basin units Nappamerri, Toolachee, Patchawarra and Tirrawarra. A total of two parameter sweeps were performed for each of these sets of units: the first sweep took, for all units in the group, the mean thermal conductivity value plus one standard deviation, the second took, for all units in the group, the mean thermal conductivity value minus one standard deviation. This has reduced the total number of independent parameter variations for the model to ten. Ten parameter variations is equivalent to 2^{10} or 1024 model sweeps. Running this reduced number of sweeps in a realistic time frame was made possible through utilisation of the NCI high performance computing facility where each sweep is run concurrently.

The results of the stochastic simulations are shown in Figure 24. The red colours show regions of the thermal model where the uncertainty of the thermal properties are high. The highest uncertainties coincide with the BLS granodiorite, the region of higher heat producing basement in the northwest, and in the northeastern side of the model in the vicinity of the Adavale Basin. This is a reflection of the higher predicted temperatures in these areas. Figure 25 shows that the percentage uncertainty is much more consistent over the study area at approximately 15 – 20 %. However, as shown in Figure 22, the minimum and maximum predicted temperature values at 4 km depth (155 °C and 235 °C respectively) are different by a factor of about 1.5. Therefore areas of high predicted temperature show up as areas of highest uncertainty.

The stochastic simulations on their own provide an indication of the uncertainty of the predicted temperature in the final model (Figure 22) due to uncertainties in the input parameters. This approach will provide a good estimate of uncertainty where there are no temperature measurements to assess the quality of the models. However, in this study, temperature data were available, and not all of the stochastic models will match the temperature data. Therefore in this study, the stochastic modelling has most likely overestimated the true uncertainty. In order to obtain a more realistic estimate of uncertainty in the final thermal model, it would be necessary to filter the stochastic models, retaining only the models that fit the data within an acceptable threshold, and recalculate the statistics on this smaller selection of models.

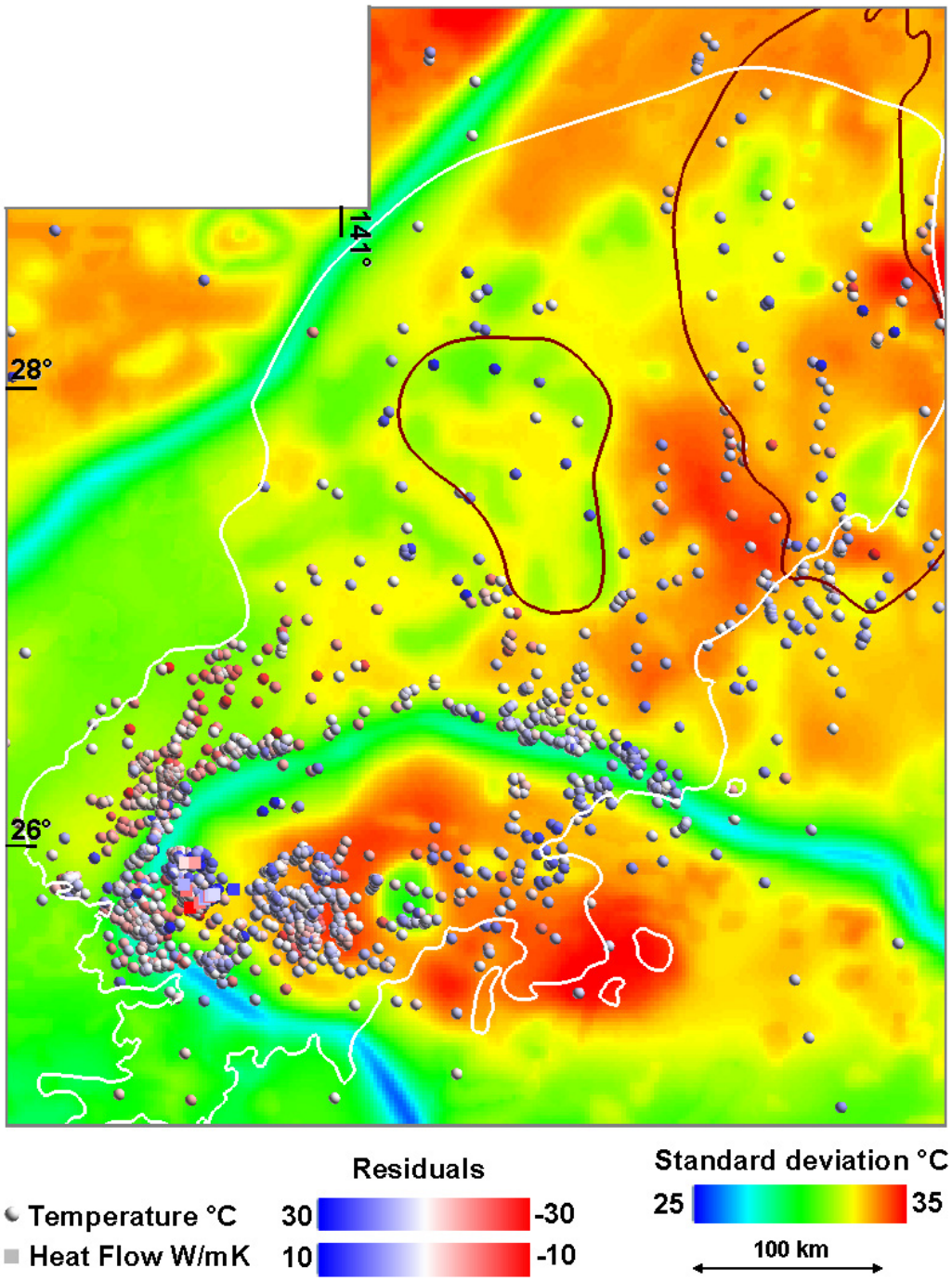

***Figure 24**: Depth slice at 4 km showing the results of the stochastic simulations as the standard deviation of the temperature from the mean value as calculated in the final thermal model (Figure 22). Coloured symbols show the calculated residuals at control points for the final thermal model; temperature residuals are represented as circles and heat flow residuals as squares. The larger standard deviation values show regions in the model where the uncertainty of the thermal properties is high. The blue linear features are artefacts and show boundaries between different crustal blocks in the thermal model.*

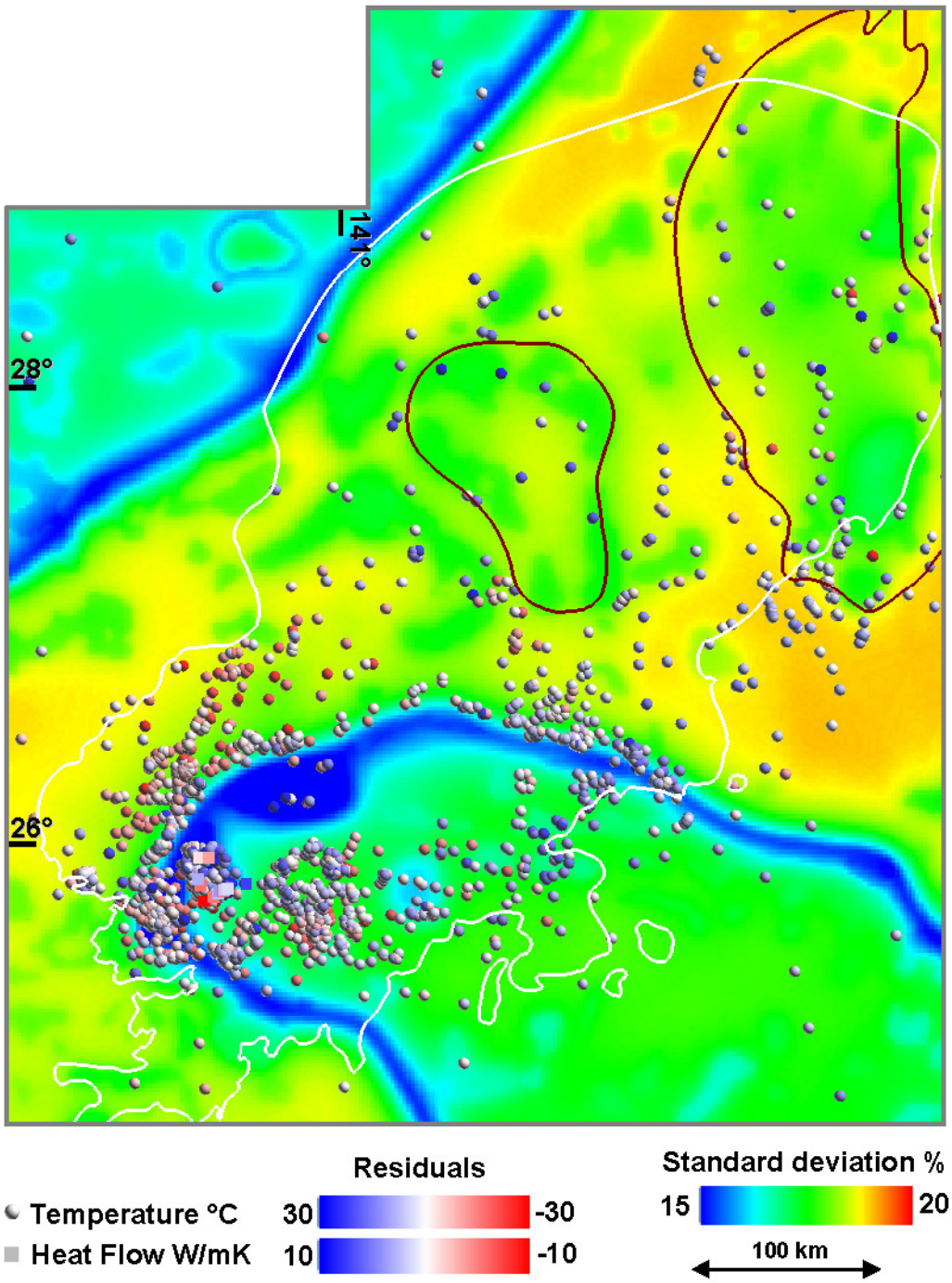

Figure 25: *Depth slice at 4 km showing the results of the stochastic simulations as the percentage uncertainty in the temperature, calculated by dividing the standard deviation by the mean. Coloured symbols show the calculated residuals at control points for the final thermal model; temperature residuals are represented as circles and heat flow residuals as squares. The blue linear features are artefacts and show boundaries between different crustal blocks in the thermal model.*

Discussion

The final thermal model shows several areas of elevated temperature at 4 km depth. Most prominent is the predicted temperature anomaly over the BLS granodiorite. This anomaly is to be expected, given the high heat production measured on the BLS granodiorite. High predicted temperatures also occur in the northwest of the study area, where the basement was assigned a high heat production value in order to match the temperature measurements.

More subtle temperature anomalies occur southeast of the BLS granodiorites, and in the northeastern corner of the study area within the Adavale Basin. The former anomaly results from increased heat production of basement in this area. The latter anomaly is a result of the low thermal conductivity assigned to the Adavale Basin compared to basement. While the Adavale Basin has a higher thermal conductivity than the Cooper Basin, it is a fairly thick sequence, and brings the total sediment thickness to over 4 km in this area. With the exception of the Nappamerri Trough (coincident with a large temperature anomaly), this is the only place in the model where this happens, and as a result the temperature is slightly elevated in this area despite a lack of significant heat sources.

The final thermal model produced as part of this study should not be considered a definitive thermal model. Although median temperature and heat flow measurements were successfully matched, further improvements could be made. For instance, improvements may be made by analysing the effect of modifying individual sedimentary units on more localised regions in the model, especially within the extent of the Cooper Basin, or modifying the heat production of individual granites or groups of granites, to analyse their effect on localised regions of the model. The Patchawarra Trough is one particular area where improvements could be made. In this region, the temperature residuals are on average positive, which means that the model has over-predicted temperature. This could result from, for example, a slightly lower basement heat production value in this region compared to the remainder of the model, or a slightly higher average thermal conductivity. Alternatively, fluid circulation may be affecting the temperature profile, resulting in a measured temperature that is slightly lower than that modelled.

Another area in which the fit to the data could potentially be improved is over the BLS granodiorites. In these areas, the temperature residuals are positive on average, indicating that the model has predicted temperatures that are too low. The heat flow residuals, however, are close to zero, indicating that the amount of heat that is being added into the model at this point is about right. The temperature residuals could be reduced by decreasing the thermal conductivity of the Cooper and Eromanga basin sediments in this region.

The influence of varying the heat production of the interpreted granite bodies on the temperature residuals was lower than expected. This was partly the result of the limited volume and depth extent of the majority of these bodies and partly due to the location of downhole temperature measurements, the majority of which are not over the interpreted granite bodies. The depth extent of the interpreted granites is controlled during the gravity inversion modelling by the density contrast between the granites and the basement. The density of the basement is poorly known and hence the density contrast is poorly constrained. Decreasing the density contrast will result in greater depth extents of the granites and a larger effect on the thermal modelling for a given heat production value.

An additional effect that may have contributed to the lower than expected influence of the heat production of granite on the predicted temperatures is the refraction of heat around the granites. This

would result from their lower assigned thermal conductivity compared to the surrounding basement. Further modelling to test the degree of refraction, and an analysis of the effect on nearby temperature residuals, may help to tie down the relative thermal conductivities of the granites and the basement in these areas, the values of which are poorly constrained.

The heat production of basement, in contrast, had a strong influence on the predicted temperature. This is not surprising given the thickness of the basement, which is 12 km or more in some places. Increasing the basement heat production even by a small amount results in a large increase in the total heat added into the model. This, combined with the fact that the basement composition (and therefore heat production) is poorly constrained in the study area, means that the heat production of basement is a large source of uncertainty in this study. The heat production of basement could be better constrained through more geochemical measurements of uranium, thorium and potassium concentrations in basement rocks and more drilling to better understand the distribution of different rock types within basement. In areas where basement outcrops, the method applied by Goodwin and van der Wielen (in prep) and Meixner et al. (2011) could be applied to provide a better estimate of basement heat production.

Another parameter that had a strong influence on the predicted temperature is the basal heat flux. In order to match the measured temperature and heat flow values, it was necessary to increase the basal heat flux above the value calculated by Neumann et al. (2000) and McLaren et al. (2003). While we agree with the conclusions of these authors that basement heat production appears to be considerably elevated in the central Australian region, we have found that the elevated heat production was not sufficient to match the temperature measurements and an elevated basal heat flux was also required.

Elevated basal heat flux is consistent with results from carbon and helium isotope measurements, soon to be published in the Cooper Basin region (Yuce and Uysal, pers. comm.). The isotopes of both elements can be used as tracers of the relative contribution of mantle versus crustal volatiles in the crust. An elevated mantle volatiles component can indicate either deep conduits in the crust allowing fluids to escape from depth, or the presence of the mantle at a shallow level. Both of these conditions are consistent with an elevated basal heat flux.

A $\delta^{13}C$ composition of approximately -5.0 to -6.5 ‰ has been identified as a common signature for CO_2 derived from the mantle (Deines, 2002; de Leeuw et al., 2010). Similarly, while ^{4}He is generated in the crust as a by-product of radiogenic decay of uranium and thorium, ^{3}He is derived mostly from the mantle with only a very small component originating from the crust (Clark et al., 1969). Therefore, elevated $^{3}He/^{4}He$ ratios in crustal fluids can indicate an increased mantle contribution of helium. In the Basin and Range province in the western United States, Kennedy and van Soest (2006) correlated $^{3}He/^{4}He$ ratios to strain rate, with increased $^{3}He/^{4}He$ associated with increased overall strain rate and increased dextral strain. Known geothermal targets were also associated with elevated $^{3}He/^{4}He$. Newell et al. (2005) compared $^{3}He/^{4}He$ ratios with P wave velocity, and found that regions of low P wave velocity are associated with elevated $^{3}He/^{4}He$ ratios. They attributed this correlation to the presence of melt material resulting in low P wave velocity and increased volatile component from the mantle.

A narrow range of $\delta^{13}C$ values between -5.89 ‰ and -6.11 ‰ has been measured in the Cooper Basin, suggesting a strong mantle component (Yuce and Uysal, pers. comm.). Measured $^{3}He/^{4}He$ ratios in the Great Artesian Basin indicate a mantle helium contribution of 0.5 – 3% (Yuce and Uysal, pers. comm.). On their own, these values are not particularly high. However they may be significant because, due to the high heat production rate associated with Cooper Basin granites

(Uysal et al., 2011), the crustal ^{4}He contribution can be expected to be higher than average crustal values.

Thermal conductivity also appears to have had quite a strong influence on the predicted temperature. In comparison, Meixner et al. (2011) noted that in their assessment of the geothermal potential of east-central South Australia, heat production was the dominant variable and thermal conductivity had a comparatively small influence. The difference is probably due to the fact that in the Cooper Basin region, low thermal conductivity basin sediments extend to depths of up to 4 km. In comparison, in the Meixner et al. (2011) study, the low thermal conductivity basins were thinner than 1.4 km for much of the study area.

In order to better constrain the thermal conductivity of the basin sediments, two things could be done. Firstly, more measurements could be performed on Cooper Basin rocks, particularly on coal, for which no measurements were available in the Cooper Basin region. Secondly, work could be done to better constrain the composition of Cooper Basin rocks so that the bulk thermal conductivity can be estimated more accurately. Given that it is very rare to find areas that are well sampled for thermal conductivity, a method similar to that described in this study could be employed in future studies to ensure that thermal conductivity is characterised accurately.

Although there were a large number of temperature measurements available for this study, there were a limited number of heat flow determinations, and the heat flow determinations that were available were restricted to one region of the model. Heat flow determinations are useful because they are not strongly influenced by thermal conductivity, and therefore can be very useful in tying down the distribution of heat sources. More heat flow determinations in this area would complement the gravity data in locating and characterising heat sources within basement.

Stochastic modelling has provided insight into the uncertainty in the final thermal model resulting from uncertainty in the input parameters. The stochastic modelling shows that the areas of high predicted temperature are also areas of high temperature standard deviation. However, the percentage uncertainty is remarkably consistent across the study area at 15 – 20 %. This consistency reflects the fact that, as discussed further below, the most dominant sources of error are the basal heat flux and the basement heat production, the uncertainties of which are (in relative terms) similar across the study area. The uncertainty in the thermal conductivity is also one of the more important sources of error, as discussed below, and as can be seen in Figure 25, the areas of thickest sediment cover show up as areas of highest percentage uncertainty in the predicted temperatures.

Future studies could include refinement of the uncertainty analysis technique. We have shown how uncertainty due to the input parameters can be assessed in a quantitative manner, providing insight into the range of possible thermal models given the uncertainty in the input parameters. The results demonstrate the importance of having temperature constraints to reduce the uncertainty; without temperature constraints, the uncertainty is very high.

Refinements to the uncertainty analysis technique could include filtering of the stochastic models retaining only those that match the temperature data. This would result in a smaller selection of models that could then be interrogated by statistical techniques. We anticipate that doing this would result in a lower overall uncertainty, as extreme scenarios with very low or very high predicted temperatures would be excluded.

Conclusions

A 3D geological map of the Cooper Basin region has been produced from 3D inversions of Bouguer gravity data using geological data to constrain the inversions. The 3D map delineates regions of low density within the basement of the Cooper and Eromanga basins that are inferred to be granitic bodies. Many of the inferred granitic bodies coincide with granite drillhole intersections and include the BLS, a known high-heat-producing unit (Middleton, 1979).

The 3D geological map has been used to predict temperatures throughout its volume using the SHEMAT software package. Thermal properties were assigned based on measurements where available or otherwise inferred from the literature, and then iteratively updated until a satisfactory match was achieved between the model and temperature measurements. The resulting temperature distribution shows strongly elevated temperatures over the BLS, as well as broader regions of elevated temperature in the northwest of the study area toward the Mt Isa Inlier, under the Adavale Basin in the northeast of the study area, and southeast of the BLS.

A higher than expected basement heat production and basal heat flux were needed to match the temperature data. Both parameters are poorly constrained, and better constraint on these parameters would substantially reduce the amount of uncertainty in this study. However, the elevated basal heat flux is consistent with recent helium and carbon isotope results which are soon to be released for the Cooper Basin region (Yuce and Uysal, Pers. comm.), which suggest that Cooper and Eromanga basin fluids have a contribution from mantle sources.

The uncertainty on many of the input parameters could be reduced by more heat flow determinations in the study area. While there is an abundance of temperature data, the few heat flow data that do exist are located in a small region in the study area. A greater spatial coverage of heat flow data will help to better constrain the relative influence of basin thermal conductivity, basement heat production and basal heat flux, and granite heat production.
Uncertainty was analysed using a stochastic modelling technique employing multiple model runs to explore viable alternative scenarios. Input parameters were systematically varied by their standard deviation and models run to determine their influence on the final model. The parameters varied in this study were: the thermal conductivity of the basin sediments, heat production of the basement and granite units, and basal heat flux. The output model provided the standard deviation of the temperature at each point in the model. This modelling has shown that areas of highest predicted temperature are also areas of highest error. It has also found that the percentage error is fairly consistent across the model volume. This is to be expected given that the main sources of uncertainty in the input parameters (basement heat production and basal heat flux) have the same percentage uncertainty. Future studies could refine the uncertainty analysis technique by filtering the stochastic models according to their fit with the temperature data.

Acknowledgements

The authors thank Peter Petkovic and Bridget Ayling for reviewing the document. Figure 6 is published with permission from the Department for Manufacturing, Innovation, Trade, Resources and Energy, South Australia. The authors publish with the permission of the Chief Executive Officer, Geoscience Australia.

References

Archibald, N., Gow, P. and Boschetti, F., 1999. Multiscale edge analysis of potential field data. *Exploration Geophysics,* 30: 38-44.

Bacchin, M., Milligan, P.R., Wynne, P. and Tracey, R., 2008. *Gravity Anomaly Map of the Australian region. Third edition. Scale 1: 15 000 000.* Geoscience Australia, Canberra.

Beardsmore, G.R., 2004. Thermal modelling of the Hot Dry Rock geothermal resource beneath GEL99 in the Cooper Basin, South Australia. *Sydney: 17th Australian Society of Exploration Geophysicists Conference*. Extended Abstracts.

Beardsmore, G.R., and Cull, J.P., 2001. *Crustal heat flow: a guide to measurement and modelling*. Cambridge University Press, 324 pp.

Beardsmore, 2004. The influence of basement on surface heat flow in the Cooper Basin. *Exploration Geophysics*, 30: 223-235.

Birch, F. and Clark, H., 1940. The thermal conductivity of rocks and its dependence upon temperature and composition. *Americal Journal of Science*, 238: 529-58.

Birch, A.F., Roy, R.F. and Decker, E.R., 1968. Heat flow and thermal history in New England and New York, in: Zen, E., White, W.S., Hadley, J.B. and Thompson, J.B. (eds.), *Studies of Appalachian Geology: Northern and Maritime, Interscience*, New York, 437-451.

Boucher, R.K., 1996. Big Lake Suite not Tirrawarra Sandstone in the Moomba Field, Cooper Basin, SA. *South Australia. Department of Mines and Energy Report Book,* 96/31: 1-5.

Bradshaw, M.T., 1993. Australian petroleum systems. *Petroleum Exploration Society of Australia Journal*, 21: 43-53.

Brocher, T.M., 2005. Empirical relations between elastic wavespeeds and density in the Earth's crust. *Bulletin of the Seismological Society of America,* 95(6): 2081-2092.

Callen, R.A., 1995. Tertiary – Callabonna Sub-Basin of the Lake Eyre Basin, in: Gravestock, D.I., Callen, R.A., Alexander, E.M., and Hill, A.J., (eds.). *STRZELECKI map sheet. South Australian Geological Survey. Geological Atlas 1:250 000 Series sheet SH54-2. Explanatory Notes.*

Chapman, D.S. and Furlong, K.P., 1977. Continental heat flow — age relationships. *Eos,* 58. 1240.

Chopra, P. and Holgate, F. L., 2005. A GIS Analysis of Temperature in the Australian Crust. *Proceedings of the World Geothermal Congress 2005,* Antalya, Turkey, 24-29 April 2005.

Clark, W.B., Beg, M.A., and Craig, H., 1969. Excess ^{3}He in the sea: evidence for terrestrial primordial helium. *Earth and Planetary Science Letters,* 6: 213-220.

Clauser, C. (ed.), 2003. *Numerical Simulation of Reactive Flow in Hot Aquifers: SHEMAT and Processing SHEMAT.* Springer-Verlag: Berlin Heidelberg, 332pp.

Cull, J.P. and Denham, D., 1979. Regional variations in Australian heat flow. *Bureau of Mineral Resources, Journal of Australian Geology and Geophysics*, 4: 1-13.

Cull, J.P. and Conley, D., 1983. Geothermal gradients and heat flow in Australian sedimentary basins. *Bureau of Mineral Resources, Journal of Australian Geology and Geophysics*, 8: 329-337.

Deines, P., 2002. The carbon isotope geochemistry of mantle xenoliths. *Earth-Science Reviews,* 58: 247-278.

Direen, N.G., and Crawford, A.J., 2003. The Tasman Line: where is it, what is it, and is it Australia's Rodinian breakup boundary? *Australian Journal of Earth Sciences,* 50: 491-502.

Draper, J.J. (ed), 2002. *Geology of the Cooper and Eromanga Basins, Queensland. Queensland Minerals and Energy Review Series.* Queensland Department of Natural Resources and Mines.

Draper, J.J., Boreham, C.J., Hoffmann, K.L., and McKellar, J.L., 2004. Devonian petroleum systems in Queensland, in Boult, P.J., Johns, D.R., and Lang, S.C. (eds.) *PESA's Eastern Australasian Basins Symposium II.* Adelaide, 19–22 September 2004.

Emerson, D.W., 1990. Notes on Mass Properties of Rocks – Density, Porosity, Permeability. *Exploration Geophysics*, 21: 209-216.

Emsley, J. (1989). *The elements*. Oxford: Clarendon Press.

Evans, P.R., Hoffmann, K.L., Remus, D.A., and Passmore, V.L., 1990. Geology of the Eromanga Sector of the Eromanga-Brisbane Geoscience Transect. *Bureau of Mineral Resources, Australia, Bulletin,* 232: 83–104.

Finlayson, D.M., Leven, J.H. and Etheridge, M.A, 1988. Structural styles and basin evolution in Eromanga region, eastern Australia. *Australian Association of Petroleum Geologists Bulletin,* 72(1): 33-48.

Fraser, A.R., Darby, F., and Vale, K.R., 1977. The reconnaissance gravity survey of Australia; Qualitative analysis. *Bureau of Mineral Resources, Geology and Geophysics Australia, Record,* 1965/251.

Gallagher, K., 1987a, Thermal conductivity of sedimentary and basement rocks from the Eromanga and Cooper Basins, South Australia. *Exploration Geophysics*, 18: 381–392.

Gallagher, K., 1987b, Thermal conductivity and heat flow in the southern Cooper Basin. *Exploration Geophysics*, 18: 62–65.

Gallagher, K., 1988. The subsidence history and thermal state of the Eromanga and Cooper Basins. *PhD thesis, Australian National University*.

Gatehouse, C.G., 1972. Formations of the Gidgealpa Group in the Cooper Basin. *Australian Oil and Gas Reviews*, 18(12): 10-15.

Gatehouse, C.G., 1983a. The geology of the Warburton Basin in South Australia. *South Australian Department of Mines and Energy, Report Book*, 82/81.

Gatehouse, C.G., 1983b. Stratigraphic units in the Warburton Basin in South Australia. G*eological Survey of South Australia. Quarterly Geological Notes*, 86: 5-8.

Gatehouse, C.G. 1986. The geology of the Warburton Basin in South Australia: *Australian Journal of Earth Sciences*, 33(2): 161-180.

Gatehouse, C.G., Fanning C.M. and Flint, R.B., 1995. Geochronology of the Big Lake Suite, Warburton Basin, northeastern South Australia. *Quarterly Geological Notes – Geological Survey of South Australia,* 128: 8-6.

Geological Survey of Queensland, 2004. Sedimentary Basins data package. Available from https://webgis.dme.qld.gov.au/webgis/webqmin

Gerner, E., and Holgate, F., 2010. *OzTemp – Interpreted Temperature at 5 km Depth.* Geoscience Australia, Canberra.

Gibson, H., Stüwe, K., Seikel, R., FitzGerald, D., Calcagno, P., Argast, S., McInerney, P., and Budd, A., 2008. Forward prediction of spatial temperature variation from 3D geology models. *Eastern Australian Basins Symposium III*. Sydney 14-17 September 2008.

Goodwin, J. and van der Wielen, S. (in prep) *A national assessment of radioelement (uranium, thorium, potassium) enrichment using radiometrics, geochemistry, and surface geology. Geoscience Australia Record.* Geoscience Australia: Canberra

Gravestock, D. I., 1995. Simpson Basin. In: J. F. Drexel and W. V. Preiss (Eds). Geology of South Australia, Volume 2, The Phanerozoic. *South Australia Geological Survey Bulletin*, 54: 31-34.

Gravestock, D.I., Callen, R.A., Alexander, E.M. and Hill, A.J., 1995, in: Gravestock, D.I., Callen, R.A., Alexander, E.M. and Hill, A.J., (eds.). *STRZELECKI map sheet. South Australian Geological Survey. Geological Atlas 1:250 000 Series sheet SH54-2. Explanatory Notes.*

Gravestock, D.I. and Gatehouse, C.G., 1995. Eastern Warburton Basin, in: Drexel, J.F., and Preiss, W.V. (eds). Geology of South Australia, Volume 2, The Phanerozoic. *South Australia Geological Survey Bulletin*, 54: 31-34.

Gray, A.R.G., McKillop, M. and McKellar, J.L. 2002 Eromanga Basin Stratigraph, in: Draper, J.J. (ed.), *Geology of the Cooper and Eromanga Basins, Queensland*. Queensland Minerals and Energy Review Series, Queensland Department of Natural Resources and Mines. pp30-56

Gunn, P. J., Milligan, P., Mackey, T., Liu, S., Murray, A., Maidment, D. and Hareen, R., 1997. Geophysical mapping using the national airbourne and gravity datasets: an example focusing on Broken Hill. *AGSO Journal of Australian Geology and Geophysics,* 17(1): 127-136.

Habermehl, M.A., 2001. Hydrogeology and Environmental Geology of the Great Artesian Basin, Australia. Chapter 11, in: Gostin, V.A. (Ed), Gondwana to Greenhouse – Environmental Geoscience. *Geological Society of Australia Inc., Special Publication,* 21: 127-143, 344-346.

Haynes, M., in prep. Geothermal Potential in the Clarence-Moreton Basin, New South Wales: A Case Study in Reducing Uncertainties in Thermal Modelling. *Eastern Australian Basins Symposium, September 2012*.

Herrin, J.M., and Deming, D., 1996. Thermal conductivity of U.S. coals. *Journal of Geophysical Research*, 101: 25,381 – 25,386.

Hoffmann, K.L., 1988. Revision of the limits of the Adavale Basin and Warrabin Trough, southwest Queensland. *Queensland Department of Mines, Record,* 1988/18.

Holgate, F., 2005. Exploration and Evaluation of the Australian Geothermal Resource. *PhD thesis, Australian National University*.

Howard, L.E. and Sass, J.H., 1964. Terrestrial heat flow in Australia. *Journal of Geophysical Research*, 69: 1617-26.

Jessop, 1990. Developments in Solid Earth Geophysics, vol. 17, Thermal Geophysics. Amsterdam: Elsevier.

Kapel, A.J., 1972. The geology of the Patchawarra area, Cooper Basin. *APPEA Journal*, 12(1): 53-57.

Kennedy, B.M. and van Soest, M.C. 2006. A helium isotope perspective on the Dixie Valley, Nevada, hydrothermal system, *Geothermics*, 35: 26-43.

Kennett, B., Salmon, M., Saygin, E. and AusMoho Working Group, 2011. AusMoho: the variation of Moho depth in Australia, *Geophysical Journal International*, 187: 946-958.

Korsch, R.J., Huston, D.L., Henderson, R.A., Blewett, R.S., Withnall, I.W., Fergusson, C.L., Collins, W.J., Saygin, E., Kositcin, N., Meixner, A.J., Chopping, R., Henson, P.A., Champion, D.C., Hutton, L.J., Wormald, R., Holzschuh, J. and Costelloe, R.D., in press. Crustal architecture and geodynamics of North Queensland, Australia: Insights from deep seismic reflection profiling, *Tectonophysics*, Available online 5 March 2012, ISSN 0040-1951, 10.1016/j.tecto.2012.02.022.

de Leeuw, G.A.M., Hilton, D.R., Güleç, N., and Mutlu, H., 2010. Regional and temporal variations in $CO_2/^3He$, $^3He/^4He$ and δ13C along the North Anatolian Fault Zone, Turkey. *Applied Geochemistry,* 25: 524-539.

Li, Y. and Oldenburg, D.W., 1998a. 3-D inversion of gravity data. *Geophysics,* 63: 109-119.

Li, Y. and Oldenburg, D.W., 1998b. Separation of regional and residual magnetic field data. *Geophysics,* 63: 431-439.

Lachenbruch, A.H., 1968. Preliminary geothermal model of the Sierra Nevada. *Journal of Geophysical Research,* 73: 6977-6989.

Lonsdale, G.F., 1965. Southern Queensland constract reconnaissance gravity survey using helicopters. *Bureau of Mineral Resources, Geology and Geophysics Australia, Record*, 65/251.

McKillop, M.D., McKellar, J.L., Draper, J.J., and Hoffman, K.L., 2005. The Adavale Basin: Stratigraphy and depositional environments. In: Munson, T.J. and Ambrose, G.J. (eds), 2007.

Proceedings of the Central Australian Basins Symposium (CABS), Alice Springs, Northern Territory, 16–18 August, 2005. *Northern Territory Geological Survey, Special Publication,* 2: 82-107.

McLaren, S., Sandiford, M., Hand, M., Neumann, N., Wyborn, L. and Bastrakova, I., 2003. The hot southern continent; heat flow and heat production in Australian Proterozoic terranes, in: Hills, R.R. and Mueller, D.R. (Eds) Evolution and dynamics of the Australian Plate. *Geological Society of America Special Paper*, 372: 157-167.

Meixner, A.J., Gerner, E., Weber, R., Brennan, T., Lewis, B., and Gallagher, R., in prep. Geothermal Systems, in: Schofield (ed). *An assessment of the uranium and geothermal prospectivity of the southern Northern Territory. Geoscience Australia Record*. Geoscience Australia: Canberra

Meixner, A.J., Kirkby, A., Champion, D.C., Weber, R., Connolly, D., and Gerner, E., 2011. Geothermal Systems, in: Huston, D. L. and van der Wielan, S. E. (eds). *An assessment of the uranium and geothermal prospectivity of east-central South Australia. Record* 2011/34. Geoscience Australia: Canberra

Meixner, A.J. and Holgate, F., 2009. The Cooper Basin Region 3D Map Version 1: A Search for Hot Buried Granites. *Record* 2009/15. Geoscience Australia: Canberra.

Meixner, A.J. and Lane, R., 2005. 3D Inversion of gravity data and magnetic data for the Tanami Region. *Annual geoscience exploration seminar (AGES), 2005 – Record of abstracts*. *Record, 2005-001*. Northern Territory Geological Survey.

Meixner, A.J., Boucher, R.K., Yeates, A.N., Frears, R.A., Gunn, P.J. and Richardson, L.M., 1999. *Interpretation of geophysical and geological data sets, Cooper Basin region, South Australia. Record, 1999/22.* Australian Geological Survey Organisation: Canberra

Middleton, M.F., 1979. Heat flow in the Moomba, Big Lake and Toolachee gas fields of the Cooper Basin and implications for hydrocarbon maturation. *Bulletin – Australian Society of Exploration Geophysics,* 10(2): 149-155.

Milligan, P.R., Franklin, R., Minty, B.R.S., Richardson, L.M. and Percival, P.J., 2010. Magnetic anomaly map of Australia (fifth edition). *Geoscience Australia*, Canberra.

Minty, B.R.S., Franklin, R., Milligan, P.R., Richardson, L.M., and Wilford, J., 2010. Radiometric Map of Australia (Second Edition), scale 1: 15 00 000. *Geoscience Australia*, Canberra.

Moore P.S., 1986, Jurassic and Triassic stratigraphy and hydrocarbon potential of the Poolowanna Trough (Simpson Desert region) northern South Australia., *Geological Society of Australia. Special Publication*, 12: 39-51

Morgan, P. 1984. The thermal structure and thermal evolution of the continental lithosphere. *Physics and Chemistry of the Earth*, 15: 107–185.

Murray, C.G. 1994. *Basement cores from the Tasman Fold Belt System beneath the Great Artesian Basin in Queensland. Record 99*. Department of Minerals and Energy, Queensland Geological Survey.

Murray, C.G., 1990. Summary of the geological developments along the Eromanga-Brisbane Geoscience Transect. *Bureau of Mineral Resources, Australia, Bulletin,* 232: 11 –20.

NGMA (National Geoscience Mapping Accord), 2001. http://www.pir.sa.gov.au/petroleum/access_to_data/seismic_data/seismic_mapping_products/cooper_basin_mapping_products/ngma_cooper-eromanga_products

Neumann, N., Sandiford, M. and Foden, J., 2000. Regional geochemistry and continental heat flow: implications for the origin of the South Australian Heat Flow Anomaly. *Earth and Planetary Science Letters,* 183: 107-120.

Newell, D.L., Crossey, L.J., Karlstrom, K.E., Fischer, T.P. and Hilton, D.R., 2005. Continental-scale links between the mantle and groundwater systems of the western United States: Evidence from travertine springs and regional He isotope data. *GSA Today*, 15(12): 4-10.

OZTemp, 2010. Data Package. https://www.ga.gov.au/products/servlet/controller?event=GEOCAT_DETAILS&catno=70604

Passmore, V.L. and Sexton, M.J., 1984. The structural development and hydrocarbon potential of Palaeozoic source rocks in the Adavale Basin region. *Australian Petroleum Production and Exploration Association Journal*, 24: 393–411.

Paten, R.J., 1977. The Adavale Basin, Queensland, in: Petroleum in Queensland – a stocktake for the future. *Petroleum Exploration Society of Australia Symposium*. Petroleum Exploration Society of Australia, Queensland Branch: Brisbane.

PIRSA (Department of Primary Industries and Regions of South Australia, now Department for Manufacturing, Innovation, Trade, Resources and Energy (DMITRE)), 2004. Cooper and Eromanga Consolidated Data Package. Data package. http://www.pir.sa.gov.au/petroleum/access_to_data/free_data/cooper__and__eromanga_consolidated_data_package

PIRSA, 2010. Petroleum and Geothermal in South Australia 2010. Data package. http://www.pir.sa.gov.au/geothermal/products__and__data/petroleum__and__geothermal_in_south_australia

Radke, B., 2009. *Hydrocarbon and Geothermal Prospectivity of Sedimentary Basins in Central Australia Warburton, Cooper, Pedirka, Galilee, Simpson and Eromanga Basins. Record 2009/25*. Geoscience Australia: Canberra.

Radke, B.M., Ferguson, J., Cresswell, R.G., Ransley, T.R. and Habermehl, M.A., 2000. *Hydrochemistry and implied hydrodynamics of the Cadna-Owie – Hooray Aquifer, Great Artesian Basin, Australia*. Bureau of Rural Sciences: Canberra.

Rankin, L.R. and Gatehouse, C. G, 1990. *The northern margin of the Warburton Basin. Quarterly Geological Notes 113*. Geological Survey of South Australia.

Raymond, O.L. and Totterdell, J. (custodians), 2012. *Australian Geological Provinces Database*. Geoscience Australia: Canberra.

Rudnick, R.L. and Gao, S., 2003. Composition of the Continental Crust. *Treatise on Geochemistry,* 3: 1-64.

Sass, J.H. and Lachenbruch, A.H., 1979. Thermal regime of the Australian Continental Crust, in: M. W. McElhinny (ed.) *The Earth: its origin, structure and evolution*. Academic Press: London, pp 301-351.

Scheibner, E. and Veevers, J.J., 2000. Chapter 19: Tasman Fold Belt System, in: Veevers, J.J. (ed.), Billion-Year Earth History of Australia and Neighbours in Gondwanaland. *Gemoc Press*, pp 154-234.

Shaw, R., Wellman, P., Gunn, P., Whitaker, A., Tarlowski, C. and Morse, M., 1996. *Users guide to the Australia crustal elements map. Record 1996/30.* Australian Geological Survey Organisation: Canberra.

Somerville, M., Wyborn, D., Chopra, P., Rahman, S., Estrella, D. and van der Meulen, T., 1994. *Hot dry rock feasibility study. Report 94/243*. Energy Research and Development Corporation. 133pp.

Stüwe, K., 2007. Geodynamics of the Lithosphere: an Introduction. 2nd edition. Springer Verlag. 493pp.

Sun, X., 1996. *Sequence stratigraphy, Sedimentology, Biostratigraphy and palaeontology of the eastern Warburton Basin (Palaeozoic), South Australia. PhD Thesis*. National Centre for Petroloeum Geology and Geophysics: University of Adelaide.

Sun, X., 1997. Structural style of the Warburton Basin and control in the Cooper and Eromanga basins, South Australia. *Exploration Geophysics*, 28(3): 333-339.

Sun, X., 1998. Geochemistry and facies analysis of Cambrian volcanics in Warburton Basin and regional correlations, South Australia. Inaugural Sprigg symposium; the Ediacaran revolution; abstracts and programme. Sydney, N.S.W., Australia, *Geological Society of Australia*, 51: 50.

Telford, W.M., Geldart, R.E., and Sheriff, R.E., 1990. *Applied Geophysics. Second Edition.* Cambridge University Press.

Thalhammer, O.A.R., Stevens, B.P.J., Gibson, J.H. and Grum, W., 1998. Tibooburra Granodiorite, western New South Wales: emplacement history and geochemistry. *Australian Journal of Earth Sciences*, 45(5): 775-787.

Weber, R.D., and Kirkby, A.L., 2011. *Thermal Conductivity Dataset.* https://www.ga.gov.au/products/servlet/controller?event=FILE_SELECTION&catno=71576

Wellmann, J.F., Croucher, A. and Regenauer-Lieb, K., 2012. Python scripting libraries for subsurface fluid and heat flow simulations with TOUGH2 and SHEMAT. *Computers and Geosciences,*

Willcox, J.B., Yeates, A.N., Meixner, A.J. and Shaw, R.D., 2003. *Structural evolution and potential petroleum plays in the Darling Basin: Pondie Range Trough - Mount Jack area: based on a seismic sequence analysis. Record 2003/05*. Geoscience Australia: Canberra.

Uysal, T., Gasparon, M., and Bryan, S.E., 2011. QGECE research on delineation of Australian geothermal resources, in: Budd, A. R. (ed), 2011. *Proceedings of the 2011 Australian Geothermal Energy Conference, 16-18 November, Melbourne. Record 2011/43*. Geoscience Australia: Canberra.

Zoth, G. and Hänel, R., 1988. Appendix in: Hänel, R., Rybach, L., Stegena, L. (eds). *Handbook of terrestrial heat flow density determination*, Kluwer Academic Publishers: Dordrecht.